Alma Mater Studiorum – Università di Bologna

Sapienza – Università di Roma

DOTTORATO DI RICERCA IN
BIOINGEGNERIA
Ciclo XXI

Settore/i scientifico disciplinari di afferenza: ING/INF-06

"Studio degli effetti termici indotti da risonanza magnetica su cateteri endocardici: modelli numerici e validazione sperimentale"

"Study of the thermal effects induced by magnetic resonance on endocardial leads: numerical models and experimental validation"

Dottorando: Ing. Eugenio Mattei

Coordinatore Dottorato: Prof. A. Cappello

Supervisore: Prof. S. Salinari

Co-supervisore: Ing. G. Calcagnini

Esame Finale 2009

Summary

Introduction

Background

Magnetic Resonance (MR) imaging (MRI) is a diagnostic technique used to obtain high quality images of the human body. The structure and abundance of water in the different tissues of the human body is the key to clinical MR imaging. The basic concept of MR is the absorption or remission of electromagnetic energy by atomic nuclei in a static magnetic field after excitation by a radiofrequency (RF) pulse [1]. A powerful magnet generates a magnetic field roughly 10,000 times stronger than the natural background magnetism from the earth. Various types of clinical MR systems currently use the superconductive magnet which utilizes 0.5 Tesla to 3.0 Tesla, and even higher fields (≥ 7 T) has been developed for research purposes.

Unlike conventional radiography and computed tomographic imaging, which make use of potentially harmful radiation (X-rays), MR imaging has many advantages, including its non-ionizing nature and the unparallel ability to discriminate different soft tissues without contrast media. MR imaging has now become the image modality of choice for imaging the brain, spine, musculoskeletal system, head and neck, complex paediatric heart malformations and other tissue structures [2]. More recently, MR imaging has been applied successfully to assess myocardial structure, wall motion, perfusion and viability. The number of MR scans performed annually has increased dramatically over the past few years [3-6].

Parallel to the growth and evolution of the MR field, is the burgeoning number of patients benefiting from implantable cardiac systems including PM and implantable cardioverter/defibrillators (ICDs) (Figure1). With new indications for heart failure, innovative device features and expanded medical coverage; this trend is likely to continue its trajectory. The combination of these two growing phenomena results in an estimated 50-75% probability of a patient being indicated for an MR study over the lifetime of their device; it has created an estimated 200,000 implanted patients who were denied the MR scan, and this numbers are likely to increase in the future [7,8].

Given the rapid expansion of technology in the fields of both MR imaging and device arrhythmia management, there is increasing interest in the issue of implantable device safety in the MR environment. In the US, to date no implantable cardiac device has the Food and Drug Agency (FDA) approval for use in the MR environment and “Do not use magnetic resonance imaging on

patients who have an implanted device" appears on product labels [8]. On November 2008, Medtronic (a leading PM manufacturing company) received the European CE Mark for a pacemaker designed for safe use in Magnetic Resonance Imaging (MRI) systems, under very limited conditions. The current state of affairs significantly limits the performance of MR imaging on device patients. With a better understanding of the hazards of performing MR scans on implanted patients as well as the development of MR safe devices, we may soon enter an era where the ability of this imaging modality may be more widely used to assist in the appropriate diagnosis of patients with devices. Not only for heart imaging but mainly for brain, spine, and joints as knees and shoulder [1-7].

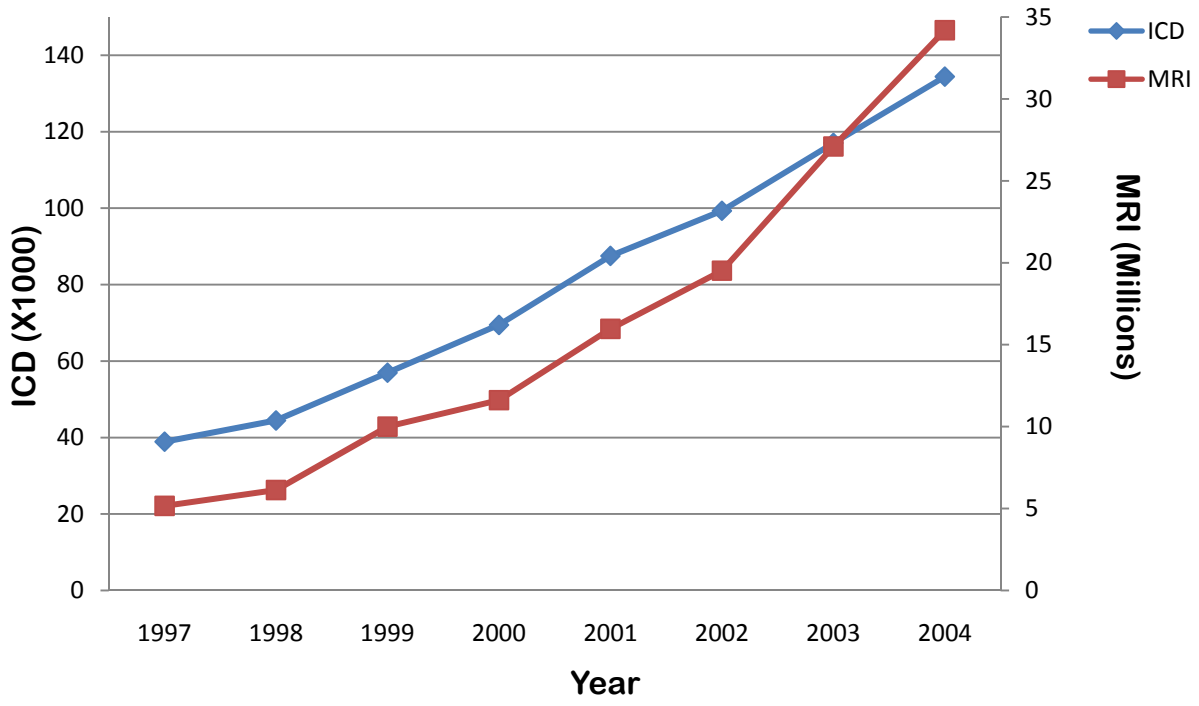

Figure 1: Number of annual MR scans and of newly implanted ICDs in the USA.

A pacemaker is needed when the heart's natural pacemaker (sinus node) is no longer functioning correctly or when the heart rate is too slow. Conditions that affect the normal, steady beat of the human heart are called "arrhythmias". Some arrhythmias are deadly. ICDs may stop potentially life-threatening fast ventricular arrhythmias. ICDs also have pacemaker functions and correct slow arrhythmias. The pacemaker or ICD is implanted just below the surface of the skin below the clavicle. One or two leads attached to the pacemaker are inserted through a vein directly into the right atrium or the right ventricle of the heart. The stimulation of the heart will be either between the pacemaker can and the tip of the pacing lead, or between the lead tip and the lead ring, which is a metallic contact a few centimetre behind the lead tip. Leads with a ring and a tip are called bipolar leads. Unipolar leads have only a tip. The lead tip is

either a screw, which will be screwed into the heart wall (preferred for atrial leads), or a half-sphere placed inside the trabecular structure of the heart [9]. Since the first implantation of a cardiac pacemaker by Ake Senning in 1958, pacemakers have undergone a remarkable development into small and multi-programmable devices [10]. In the beginning, pacemakers could only stimulate the heart with a fix frequency ignoring any signals coming from the heart. This so-called asynchronous mode may still be programmed in current devices. However, with improvements in microelectronics and the better understanding of the electrophysiology of the human heart, pacemakers that could ”listen” to the heart have been developed. Nowadays, commonly used pacemakers measure the electrical potentials in the right atrium and in the right ventricle. This process is referred to as sensing. The pacemaker will only stimulate if no natural stimulation of the heart can be seen. Pacemaker-dependent patients show a low intrinsic rhythm or no intrinsic rhythm at all. The pacemaker will pace continuously. By using piezo crystals to measure motions and by measuring the impedance through the lung to detect the breathing rate, state-of-the-art pacemakers can predict the physical activity very accurately and adapt stimulation properly.

Nowadays, approximately 2 million Europeans have implanted pacemakers, but these patients are prohibited from receiving MRI scans. According to recent estimates, up to 50 % of patients worldwide with implanted cardiac devices are expected to need an MRI scan during the lifetime of their devices. It is thus clear that the possibility to extend MRI investigations also to patients implanted with pacemakers or ICDs, represents an important challenge that could bring great benefits to human health.

Potential effects of MRI on pacemaker systems

With the ability of measuring electrical potentials in the heart, the potential risk of interference with electromagnetic fields also becomes more likely [11-13]. Electromagnetic interference sources, such as theft prevention and security equipment, cellular phones, strong electric motors, high-voltage systems, radio transmitters, may inhibit the pacemaker [14]. In magnetic fields above 0.5mT, the pacemaker switches to an asynchronous mode to prevent any inappropriate sensing. The strong gradients and RF fields of an MRI device show the risk to influence the pacemakers. The fields in an MRI device are considerably stronger than those commonly used in daily life, which may lead to additional adverse effects. However, the ongoing developments in MRI and the increasing number of pacemaker and ICD patients will increase the pressure on radiologist to allow MRI investigations in pacemaker patient under certain circumstances [15–19]. Out of the 13 reported cases of lethality with MRI, eleven were on recipients of implanted devices. In all cases, the MRI investigations were performed without monitoring of the patient. Nevertheless, there exists over a hundred published cases where patients with implanted pacemaker had a MRI examination without any complications. These numbers suggest that MRI is a

potential risk for patients with implanted pacemakers, but MRI may be possible under certain circumstances. It has also been discussed whether imaging of brain and lower extremity may pose potentially less risk than imaging of the thorax.

The electromagnetic field generated by an MRI scanner is made up of three main components:

- the static magnetic field, used to align the magnetic dipoles of the atoms of the biological tissues;
- the radiofrequency (RF) field, that excites the atoms giving them an amount of energy that will be released as soon as the RF signal is turned off;
- the time-varying magnetic static filed, needed to select a particular slice of tissue over the whole body.

Potentially all these three components may interfere with the correct behaviour of a PM (table 1) [11,12, 20–22]. The static magnetic field may cause implant displacement as well as the closure of the reed switch, resulting in asynchronous pacing. The radiofrequency (RF) field may induce electrical currents along the lead which might result in dangerous heating at the lead tip and in an undesirable fast pacing rate and . The time-varying magnetic gradient fields may as well induce heating and currents in the pacemaker system of sufficient magnitude to pace the heart.

Table 1: Potential effects of MRI pacemaker systems

1. Static magnetic field
(a) Reed-switch closure
(b) Pacemaker displacement
(c) Changes in sensed electrograms
2. Radiofrequency field
(a) Heating
(b) Alterations in pacing rate
(c) Pacemaker reprogramming or reset
3. Time-varying magnetic gradient field
(a) Induction voltage
(b) Heating
(c) Reed-switch closure

Today, the materials typically used by pacemaker manufactures (basically titanium and its alloy) have physical properties that make negligible the mechanical effects caused by the static magnetic field.

Several papers in literature [23,24] confirm, indeed, that the torque magnitude over a PM exposed to 1.5T magnetic field (typical value of a clinical MRI scanner) is lower than the gravity force caused by the earth on the pacemaker itself.

More dangerous are the effects on the electrical components of the stimulator: the RF field and the gradient field can mimic the physiological activity of the hearth and thus causing an inappropriate activity of the PM. For this reason, modern devices has a field sensor that, when exposed to fields higher than 05mT, turn the PM into the "magnet mode"; such an operation mode implies that the pace rate becomes fixed to a specific value and does not change according to what is measured from the heart. Experimental studies, however, point out that the switch from the normal to the magnet mode can experience malfunctions when the magnetic field is very high (such as the one of an MRI scanner [23]). As a consequence, unwanted pacing of the myocardium might occur [11,25].

The heating generated at the lead tip owing to the induced currents that flow from the PM lead inside biological tissues is the most significant and potentially dangerous effect of the complex interactions between a PM and a MRI scanner. In particular, since the magnitude of the RF filed is several times higher than the gradient filed, the induced heating is mainly due to the RF field.

MRI induced heating

MRI induced heating is one of the known risks for implanted PM and ICD: the RF field energy generated during MRI procedures may be coupled into conductive leads in two major ways [26]:

1) The conductive lead acts as an antenna capable of receiving and supporting the frequency of the MRI unit's RF field (63.8 MHz for 1.5 Tesla systems or 127.6 MHz for 3.0 Tesla systems). This mechanism can create the resonant waves.

2) The implant acts as an electrical ''short circuit'' to the electrical potentials induced within the body by the MRI RF field.

Each of these effects induces a RF current which flows from the lead into the surrounding tissues. As a consequence of the high electrical resistance of these tissues, resistive heating is then generated at the lead-tissue interface, causing a temperature increase that could be dangerous for the patients.

The scientific and medical literature clearly shows that the MRI-induced heating on metallic leads cannot be immediately neglected: Sommer et al. [27] demonstrated the potential for heating as much as 23.5°C at specific absorption rate (SAR) levels of only 1.3 W/kg in a 0.5 Tesla MRI unit. Achenbach et al. [28] reported pacing lead tip temperature elevation in leads not attached to an implanted pulse generator (IPG) of >63°C during 90 seconds of MRI. Roguin [29] observed in an animal model a lose capture for 12 hours following an MRI, concluding that "… some edema occurred at the tip-lead tissue interface, which subsequently resolved.'' Martin and Coman [30] observed 9.4% of their patients undergo ''significant'' changes to their pacing thresholds after MRI. Konings et al. [31] reported heating around intravascular guide wires by resonating RF waves of 26°C to 74°C after 30 seconds. Bassen et al. [32] measured a

temperature rise of about 0.5°C (local SAR=320 W/kg) for a stent exposed to the RF field of a 1.5 T MRI birdcage coil at 64 MHz; using the same experimental set-up, a temperature increase of 8.6 °C was observed at the bare end of an insulated 24-cm long wire (local SAR=5680 W/kg). Rezai et al. [33] reported deep brain stimulator temperature elevations at the electrode tip of >25°C within 15 minutes of MR imaging. This data is particularly disturbing when one realizes that thermal ablation procedures are typically performed at temperatures of approximately 50–60°C. At the same time, over 300 patients to date have been scanned without any significant clinical difficulty or complication [34]. In a recent study [35], sixteen scans at 3T, with a SAR limited to 2W/kg, were performed with an electrophysiologist present on 14 patients implanted with a variety of devices from various manufacturers: all patients were successfully scanned, with no arrhythmias and no significant change in the programmed parameters, pacing thresholds, sensing, impedance, or battery parameters noted. Only one patient noted chest burning during the scan.

Such widely varying results indicate how the performance of an implanted or interventional device undergoing MRI is a very complex problem. While it is relatively easy to demonstrate a heating or induced voltage problem, it is far more difficult to prove a solution to these problems, due to the complex and unpredictable nature of the MRI interaction. Several factors influence the degree of heating: the whole body specific absorption rate, the patient position in the coil, the type of imaging sequence, the patient characteristics, the duration of imaging procedure, the body structure being imaged, the type and position of transmit coil, the lead design, the lead orientation within the patient, the degree of perfusion near the device, the temperature measurement procedure, the respiratory phase, etc. Many of these parameters are currently either not recognized or inadequately addressed by existing testing methods [26]. The lack of standardization in the measuring methods and the large number of variables which may be involved in the amount of heat generation, as well as the possible occurring of resonance phenomena, make difficult to perform extensive and exhaustive experimental measures. Thus, besides experimental measures, the development of numerical models could represent a very useful approach to investigate the potential effects of MRI on implantable medical devices.

Currently, one of the most challenging problems in medical device simulation is the research and design of active medical implants which do cause heating when exposed to the RF fields of an MRI scanner. Both patients and industry would largely benefit from MRI safe implants. But simulation of a complex implant, embedded in an inhomogeneous body and surrounded by a large electrical resonator, with micrometer resolution is a challenging task. Many different numerical approaches have been developed to solve Maxwell's equations, each having its own advantages and limitations. For example, the Method of Moments (MoM) is fast and accurate for solving metallic structures and electrically large problems, while the Finite Difference Time Domain (FDTD) method is well suited to solving inhomogeneous structures (dielectric and metal), partially due to its straightforward approach. Current trends in GPU (*Graphic Processing Unit*) based hardware acceleration solutions offering up to 100x faster simulation in desktop form-factors, are still mostly restricted to FDTD solvers. For these reasons, the FDTD method is often chosen as the preferred method for many RF simulations of medical applications where transmitters and

patient must be considered. These range from Magnetic Resonance Imaging (MRI) systems to implanted devices with active telemetry like pacemakers. Here FDTD is used to study a number of issues including coil design and field homogeneity, SAR, EMC, worker safety, etc. However, if numerical studies are today widely recognize as an important and useful mean also in critical analysis such as medical safety or electromagnetic compatibility, it is still clear that no numerical model has great sense if not validated through experimental measures.

In this study both experimental measures and numerical analysis were performed. Aim of the study is to systematically investigate the effects of the MRI RF filed on implantable devices and to identify the elements that play a major role in the induced heating. Furthermore, we aimed at developing a realistic numerical model able to simulate the interaction between an RF coil for MRI and biological tissues implanted with a PM, and to predict the induced SAR and temperature increases as a function of the particular path of the PM lead.

Outline

Each chapter is presented as a full paper and the chapters are sorted according to the activity carried out during the three years of the Ph.D. research study.

The first three chapters describe the experimental measures mainly performed during the first year of the research project. In chapter 1 we focused on the definition of an experimental measurement method suitable to be used in a RF environment, to record temperature and SAR in in-vitro experiment at the tip of thin metalllic structures, such as the lead of a PM or an ICD. In particular, the most appropriate positioning of the fluoroptic® temperature probes to measure the maximum lead tip heating was identified, and we also computed the underestimation to the other temperature probe positions in relation to the optimal position.

In chapter 2 a wide database of temperature and SAR experimental measurements is presented. These measures were performed at the Center for Devices and Radiological Health (CDRH) of the Food and Drug Administration (FDA, Washington, USA), inside a 1.5T RF birdcage coil, on wires and PM leads, placed inside phantoms of different shapes. The aim of these measurements was to systematically quantify the contribution of some potential factors involved in the MRI induced heating: the length and the geometric structure of the lead; the implant location within the body and the lead path; the shape of the phantom used to simulate the human trunk and its relative position inside the RF coil. In addition, the data collected will serve as an open-access experimental database for numerical models validation.

Chapter 3 describes another set of experimental measurement; differently from the data presented in chapter 2, we focused our attention on those characterizing real implants in clinical

practice. In this study we investigate the effect of the lead geometry and the lead and pacemaker can placement of an implantable pacemaker on lead heating induced by clinical MRI. We also compared the measures obtained in a laboratory RF coil with the one recorded inside a clinical MRI scanner, using several RF sequences typically adopted during medical procedures.

Chapter 4 and 5 summarize the activity of the second year, which mainly focused on the development of a numerical model of the electromagnetic field generated by an MRI RF coil. In chapter 4 we compared different FDTD models in terms of resulting electromagnetic field distribution and computational effort required. In chapter 5 the current methods for the SAR evaluation inside biological tissues exposed to RF fields are discussed: we showed the effect of thin metallic structures on the local distribution of the electric filed and the associated SAR, to determine to what extent the present standard methods for SAR evaluation are appropriate in the presence of thin metallic structures. Finally, we proposed a refinement of the actual standard to meet the constraint of this particular application.

Chapter 6 and chapter 7 present the integration between the numerical models and the experimental data. A brief description of the FDTD method is given and the experimental and simulated results are compared, in order to validate the numerical model we developed. In particular, the project, the realization and the characterization through RF measurements of a birdcage coil prototype was carried on. Based on data collected from the coil prototype, we developed and validate a realistic numerical model (human visible dataset) able to simulate the interactions between the RF field generated by an MRI birdcage coil and a pacemaker implanted inside the human body, that was the final aim of the study.

References

[1] Pinski SL, Trohman RG: Interference in implanted cardiac devices, Part II. *Pacing Clin Electrophysiol* 2002; **25**: 1496-1509

[2] Niehaus M, Tebbenjohanns J. Electromagnetic interference in patients with implanted pacemakers or cardioverter-defibrillators. *Heart* 2001; **86**: 246-248.

[3] Hundley WG, Morgan TM, Neagle CM, et al. Magnetic resonance imaging determination of cardiac prognosis. *Circulation*. 2002 ;**106**: 2328-2333.

[4] Gerber BL, Garot J, Bluemke DA, Wu KC, Lima JA. Accuracy of contrast-enhanced magnetic resonance imaging in predicting improvement of regional myocardial function in patients after acute myocardial infarction. *Circulation*. 2002;**106**:1083-1089.

[5] Kim RJ, Wu E, Rafael A, et al: The use of contrast-enhanced magnetic resonance imaging to identify reversible myocardial dysfunction. *N Engl J Med*. 2000; **343**:1445-1453.

[6] Klein C, Nekolla SG, Bengel FM, et al: Assessment of myocardial viability with contrastenhanced magnetic resonance imaging: comparison with positron emission tomography. *Circulation* 2002; **105**:162-167.

[7] Kalin R, Stanton MS: Current clinical issues for MRI scanning of pacemaker and defibrillator patients. *Pacing Clin Electrophysiol.* 2005;**28**:326-328.

[8] Kanal E, Borgstede JP, Barkovich AJ et al: American College of Radiology White Paper on MR safety:2004 update and revisions. *AJR.*2004; **182**:1111-1114.

[9] Hayes DL, Lloyd MA, and Friedman PA. Cardiac Pacing and Defibrillation A Clinical Approach. *Futura Publishing Company*, Inc., 2000

[10] Brunckhorst C, Candinas R, and Furman S. Ake senning 1915-2000. *Pacing and Clinical Electrophysiology*, **11**:1710, 2000.

[11] Erlebacher JA, Cahill PT, Pannizzo F, and Knowles RJ. Effect of magnetic resonance imaging on DDD pacemakers. *The American Journal of Cardiology* 1986, **57**:437-440

[12] Hayes DL and Vlictstra RE. Pacemaker malfunction. *American College of Physicians* 1993, **119**:828-835

[13] Lauck G, Smekal VA, Wolke S, Seelos CS, Jung W, Manz M, and Berndt Luderitz. Effects of nuclear magnetic resonance imaging on cardiac pacemaker. *Pacing and Clinical Electrophysiology* 1995, **18**:1549-1555

[14] Irnich W. Interference in pacemaker. *Pacing and Clinical Electrophysiology* 1884, **7**:1021-1048

[15] Sommer TV, Lauck G, Smekal AV, Reike M, Hofer U, Block W, Traber F, Schneider C, Gieseke J, Jung W, and Schild H. MR imaging and cardiac pacemakers: In vitro evaluation and in vivo studies in 51 patients at 0.5 T. *Radiology*, **215**:869{879, 2000.

[16] Alagona P, Toole JC, Maniscalco BS, Glover MU, Abernathy GT, and Prida XE. Nuclear magnetic resonance imaging in a patient with a DDD pacemaker. *Pacing and Clinical Electrophysiology*, **12**:619, 1989. Letter to the Editor.

[17] Inbar S, Larson J, Burt T, Mafee M, and Ezri MD. Case report: Nuclear magnetic resonance imaging in a patient with a pacemaker. *American Journal of the Medical Sciences* March 1993, **305**(3):174-175

[18] Garcia-Bolao I, Albaladejo V, Benito A, Alegria E, and Zubieta JL. Magnetic resonance imaging in a patient with a dual-chamber pacemaker. *Acta Cardiologia* 1998, **19**:33-35

[19] Gimbel JR, Johnson D, Levine PA, and Wilkoff BL. Safe performance of magnetic resonance imaging on five patients with permanent cardiac pacemakers. *Pacing and Clinical Electrophysiology* June 1996, **19**:913-919

[20] Pavlicek W, Geisinger M, Castle L, Borkowski GP, Meaney TF, Bream BL, and Gallagher JH. The effects of nuclear magnetic resonance on patients with cardiac pacemakers. *Radiology* 1983, **147**:149-153

[21] Fetter J, Aram G, Holmes DR, Gray JE, and Hayes DL. The effects of nuclear magnetic resonance imagers on external and implantable puls generators. *Pacing and Clinical Electrophysiology* 1984, **7**:720-727

[22] Shellock FG and Kanal E. SMRI report: Policies, guidelines and recommendations for MR imaging safety and patient management. *Journal of Magnetic Resonance Imaging* 1992, **2**:247-248

[23] Luechinger R, Duru F, Scheidegger MB, et al., Force and torque effects of a 1.5-Tesla MRI scanner on cardiac pacemakers and ICDs. *Pacing Clin Electrophysiol* 2001, **24**:199–205

[24] Shellock FG, Tkach JA, Ruggieri PM, Masaryk TJ, Cardiac pacemakers, ICDs, and loop recorder: evaluation of translational attraction using conventional ("long-bore") and "short-bore" 1.5- and 3.0-Tesla MR systems, *J Cardiovasc Magn Reson*. 2003, **5**:387–397

[25] Hayes D.L., Holmes D.R. Jr., Gray J.E., Effect of 1.5 Tesla nuclear magnetic resonance imaging scanner on implanted permanent pacemakers, *J Am Coll Cardiol* 1987, **10**:782–786

[26] Helfer JL, Gray RW, MacDonald SG, Bibens TW: Can pacemakers, neurostimulators, leads, or guide wires be MRI safe? Technological concerns and possible resolutions. *Minim Invasive Ther Allied Technol* 2006, **15**(2):114-20

[27] Sommer T, Vahlhaus C, Lauck G, von Smekal A, Reinke M, Hofer U, Block W, Traber F, Schneider C, Gieseke J, Jung W, Schild H: MR imaging and cardiac pacemakers: in-vitro evaluation and in-vivo studies in 51 patients at 0.5 T. *Radiology* 2000, **215**(3):869-79

[28] Achenbach S, Moshage W, Diem B, Bieberle T, Schibgilla V, Bachmann K: Effects of magnetic resonance imaging on cardiac pacemakers and electrodes. *Am Heart J* 1997, **134**(3):467-73

[29] Roguin A, Zviman MM, Meininger GR, Rodrigues ER, Dickfeld TM, Bluemke DA, Lardo A, Berger RD, Calkins H, Halperin HR: Modern pacemaker and implantable cardioverter/defibrillator systems can be magnetic resonance imaging safe: in vitro and in vivo assessment of safety and function at 1.5 T. *Circulation* 2004, **110**(5):475-82. 2004 Aug 3

[30] Martin ET, Coman JA, Shellock FG, Pulling CC, Fair R, Jenkins K: Magnetic resonance imaging and cardiac pacemaker safety at 1.5-Tesla. *J Am Col Cardiol* **43**(7):1315-24. 2004 Apr 7

[31] Konings MK, Bartels LW, Smits HF, Bakker CJ: Heating around intravascular guidewires by resonating RF waves. *J Magn Reson Imaging* 2000, **12**(1):79-85

[32] Bassen H, Kainz W, Mendoza G, Kellom T: MRI-induced heating of selected thin wire metallic implants – laboratory and computational studies – findings and new questions raised. *Minim Invasive Ther Allied Technol* 2006, **15**(2):76-84

[33] Rezai AR, Baker KB, Tkach JA, Phillips M, Hrdlicka G, Sharan AD, Nyenhuis J, Ruggieri P, Shellock FG, Henderson J: Is magnetic resonance imaging safe for patients with neurostimulation systems used for deep brain stimulation? *Neurosurgery* 2005, **57**(5):1056-62

[34] Kanal E: White Paper on MRI Safety. In American Society of Neuroradiology Toronto, Canada. May 24, 2005

[35] Gimbel JR: Magnetic resonance imaging of implantable cardiac rhythm devices at 3.0 tesla. *Pacing Clin Electrophysiol*. 2008 Jul; **31**(7):795-801

Chapter 1

Temperature and SAR measurement errors in the evaluation of metallic linear structures heating during MRI using fluoroptic® probes

E Mattei[1], M Triventi1, G Calcagnini[1], F Censi[1], W Kainz[2], H I Bassen[2] and P Bartolini[1]

[1] Department of Technologies and Health, Italian National Institute of Health, Roma, Italy

[2] Center for Devices and Radiological Health, Food and Drug Administration, Rockville, MD, USA

Published on Phys. Med. Biol. **52** (2007) 1633–1646

Abstract

The purpose of thiswork is to evaluate the error associated with temperature and SAR measurements using fluoroptic® temperature probes on pacemaker (PM) leads during magnetic resonance imaging (MRI). We performed temperature measurements on pacemaker leads, excited with a 25, 64, and 128 MHz current. The PM lead tip heating was measured with a fluoroptic® thermometer (Luxtron, Model 3100, USA). Different contact configurations between the pigmented portion of the temperature probe and the PM lead tip were investigated to find the contact position minimizing the temperature and SAR underestimation. A computer model was used to estimate the error made by fluoroptic® probes in temperature and SAR measurement. The transversal contact of the pigmented portion of the temperature probe and the PM lead tip minimizes the underestimation for temperature and SAR. This contact position also has the lowest temperature and SAR error. For other contact positions, the maximum temperature error can be as high as −45%, whereas the maximum SAR error can be as high as −54%. MRI heating evaluations with temperature probes should use a contact positionminimizing the maximum error, need to be accompanied by a thorough uncertainty budget and the temperature and SAR errors should be specified.

1.1 Introduction

Magnetic resonance imaging (MRI) is a widely accepted tool for the diagnosis of a variety of disease states. However, the presence of a metallic implant, such as a cardiac pacemaker, or the use of conductive structures in interventional therapy, such as guide wires or catheters, are currently considered a strong contraindication to MRI [1-4]. Most of the publications dealing with novel MR techniques on patients with implanted linear conductive structures [5-9] point out that the presence of these structures may produce an increase in power deposition around the wire or the catheter. Unfortunately, this increased local absorption rate (SAR) is potentially harmful to the patient due to an excessive temperature increase which can bring living tissues to necrosis. The most direct way to measure SAR deposition along the wire is by using a fluoroptic® temperature probe. In such probes, the temperature sensor is a half-sphere of approximately a 0.3 mm diameter encapsulated inside a cylindrical pigmented jacket and located at the terminal portion of a flexible fibre optic cable. The pigmented jacket (approx. 3 mm length, 0.8 mm diameter) has to prevent ambient light from interfering with the sensor, as well as acting as a reference for the probe positioning.

Because of the well-known limitations of conventional thermometry methods in radiofrequency energy environments [10,11], the use of fluoroptic® thermometry has become the ‘state-of-the-art’ and the industry standard in this field. This method has been used to examine radiofrequency energy-induced heating of tissues, *in vitro* and *in vivo*[11-15].

However, some methodological issues have found limited attention so far. Among them, the underestimation of heating due to the positioning of the temperature probes, as well as the error in temperature and SAR measurement needs to be investigated and standardized. In particular, thin linear structures such as PM leads may generate temperature gradients which cannot be neglected with respect to the physical dimension of the temperature probes. As a consequence, it is not possible to obtain accurate estimation of the maximum temperature and SAR in the lead tip region.

When the investigation involves small objects and rapidly changing (in space and time) temperature gradients, there is the need to define a standardized method for positioning of the temperature probes. This standardized method should minimize the underestimation and the error associated with temperature and SAR measurements. In most of the publications dealing with the heating of conductive structure during MRI, the generated heat is confined in close proximity to the lead tip, but temperature increases appear significantly different, even in the case of apparently similar experimental set-ups [16-20]. The relative positioning of the temperature probe and the lead tip may significantly affect the measurement and can explain, at least partially, the inconsistency of the results.

The aim of this paper is to identify a positioning of fluoroptic® temperature probes next to PM lead tips to measure the maximum lead tip heating. Once this optimal position is found we will assess the temperature and SAR underestimation of the other temperature probe positions in relation to the optimal position. In additions to the underestimation, we estimate the associated error for temperature and SAR measurement for all temperature probe positions using a numerical model of the lead.

1.2 Materials and methods

1.2.1. Experimental model

A PVC phantom (a 28×20×26 cm^3 box) was filled with 2% hydroxy-ethyl-cellulose (HEC), 0.36% sodium chloride and the rest water: a gel saline solution with 0.59 Sm^{-1} conductivity and 79 permittivity at 64 MHz, and 4178.3 J kg^{-1} K^{-1} heat capacity [21]. A 26 × 18 cm^2 grid was submerged in the gel to support the pacemaker and its lead and maintained a consistent separation distance between the implant, phantom gel surface and the temperature probes. The grid was adjusted so that the top of the implant was positioned below the phantom surface.

SAR and temperature were measured on the tip of a 62 cm long monopolar lead (S80TM, *Sorin Biomedica* CRM, Italy). The lead has an inner conductive wire of 0.4 mm radius, 0.5 mm external silicon insulation and a tip area of about 2 mm^2. A radio frequency (RF) signal was injected into the lead tip using a coaxial cable connected to the lead. The outer conductor (signal ground) was connected to a 1 × 20 × 10 mm^3 silver plate located on one side of the PVC box. The current flow through the gel went from the lead tip to the plate (figure 1).

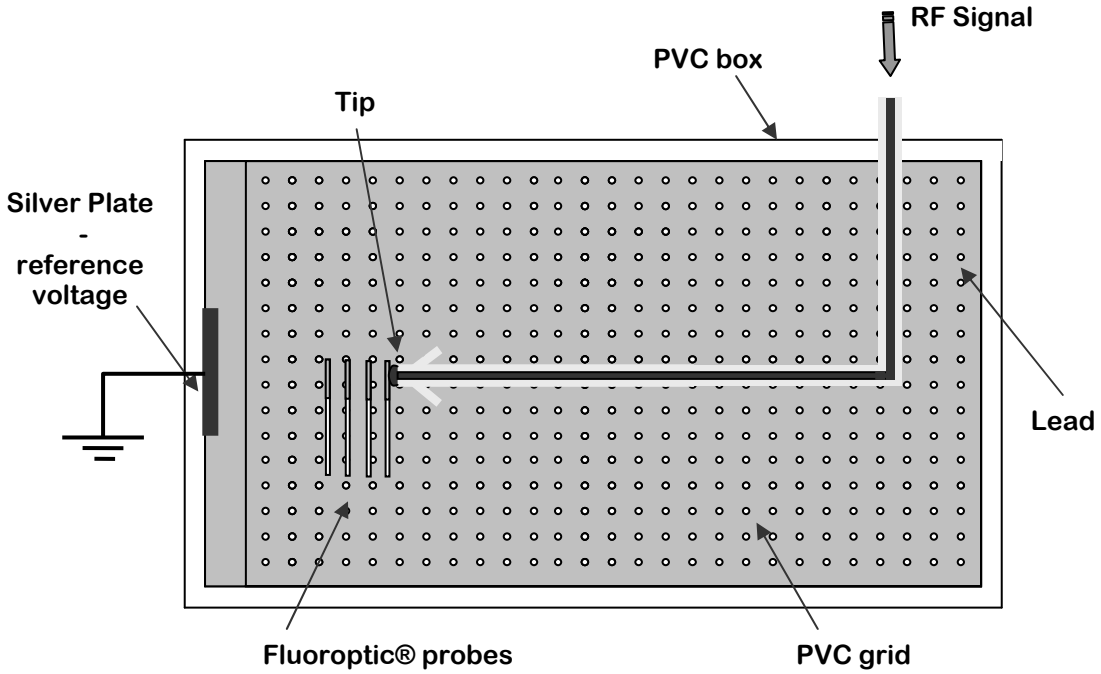

Figure 1. Experimental set-up for SAR and temperature measurements. The position of the fluoroptic® probes for model identification is also illustrated.

The lead was placed in the gel 5 cm below the phantom top surface, simulating an implant in the human body. The distance between the silver plate and the lead tip was 7 cm; the overall submerged lead length was 58 cm. Temperature was measured using a fluoroptic® thermometer (*Luxtron*, Model 3100, USA, *SMM* probes), with a resolution of 0.1 °C, operating at eight samples per second.

Three sinusoidal excitations were studied: 25, 64 and 128 MHz, which approximately correspond to the RF field used in 0.5, 1.5, and 3 T MRI systems. Signals were generated by a RF generator (*Rhode & Schwartz*, SMT 06), and then amplified (*RFPA,* RF 06100-6, France); a power meter (*Rhode & Schwartz* NRT, Z14, range 25–1000 MHz) was connected to the output of the amplifier measuring the average power generated and the reflection coefficient of the load.

The preliminary measurements investigated different contact configurations between the terminal part of the temperature probes and the pacing electrode at the lead tip. The aim was to identify the temperature probe position which results in the maximum heating and to assess the relative underestimations associated with other configurations.

We studied the following possibilities (figure 2):

(a) transversal contact between the side of the temperature probe and the circular surface of the lead tip;

(b) transversal contact between the tip of the temperature probe and the side surface of the electrode;

(c) axial contact between the tip of the temperature probe and the circular surface of the lead tip;

(d) axial contact between the tip of the temperature probe and the side surface of the electrode.

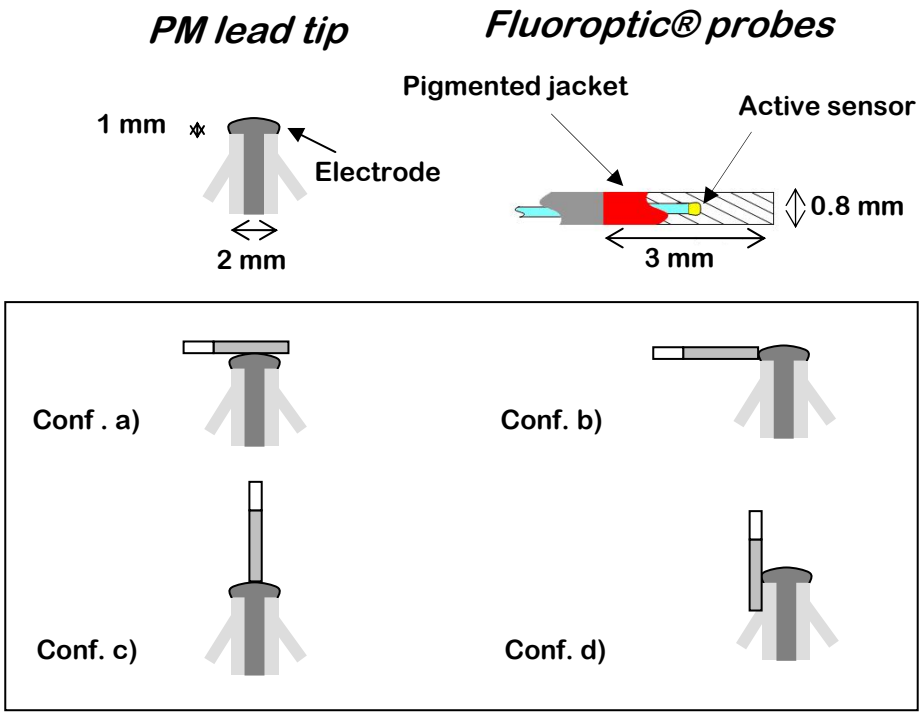

Figure 2. Schematic representation of the sensitive portion of temperature probes and different contact configuration with the tip of a pacemaker lead: transversal contact between the side of the probe and the circular surface of the lead tip (conf. a); transversal contact between the tip of the probe and the side surface of the electrode (conf. b); axial contact between the tip of the probe and the circular surface of the lead tip (conf. c); axial contact between the tip of the probe and the side surface of the electrode (conf. d).

The underestimation was expressed as the difference of the temperature increase measured with the particular temperature probe position with respect to that leading to the maximum temperature increase.

For the same experimental set-up we mapped the temperature in the HEC solution at the gel to electrode interface, at 2 mm, 4 mm and 6 mm from the lead tip (figure 1). Temperature variations were recorded for an interval of 300 s, in which the excitation was active, and in the following 200 s, with no current through the PM lead. These measurements were used to validate the numerical model described in the next section. The best fitting between experimental and modeling data was reached leaving the voltage applied on the lead tip as a free parameter.

1.*2.2. Numerical model*

A numerical model was developed to estimate the maximum temperature increase and the local SAR deposition. We used the models also to assess the measurement error due to temperature probe positioning and physical dimensions. Given the complexity of solutions for the heat-transfer thermal equations [22,23], a finite-element analysis was performed instead of an analytic solution. We developed a three-dimensional model with a commercial software (FEMLAB 3.1, *Comsol Multiphysics*) by which we did coupled analysis that involved simultaneously both thermal and electromagnetic equations.

The native 3D drawing section of the software was used to develop a realistic computer model of the pacemaker lead tip (figure 3). The lead tip is placed inside a saline-filled cylinder of 5 cm radius and 10 cm height).

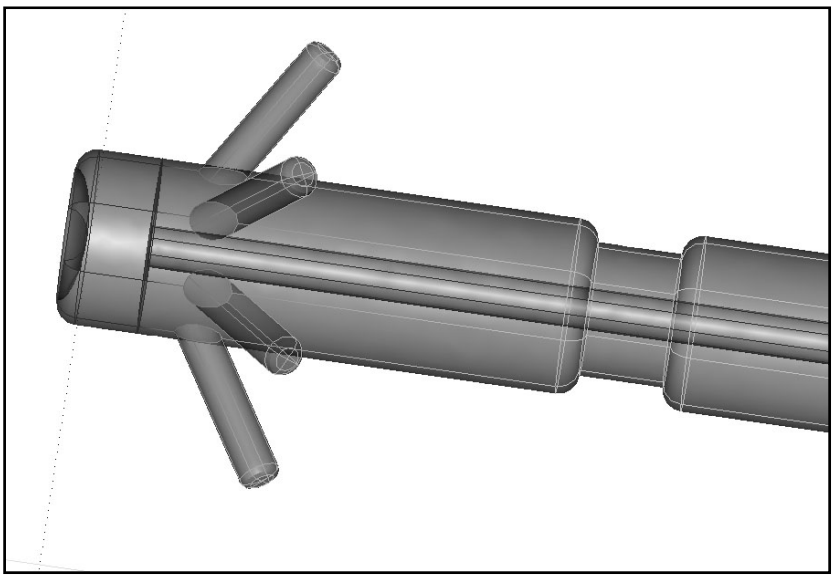

Component	Material	Electrical Conductivity [Sm^{-1}]	Thermal Conductivity [$Wm^{-1}K^{-1}$]
Electrode	Aluminum-Pyrolytie Carbon	3.77×10^{7}	0.1
External Insulation	Silicon	1×10^{-12}	163
Inner Conductor	Aluminum	3.77×10^{7}	160

Figure 3. Pacemaker lead tip: geometry and properties of the materials.

Electromagnetic and thermal properties (specific weight, heat capacity, thermal conductivity and electrical conductivity) of the different elements were chosen to closely approximate those of our experimental system.

The software is furnished with a variable grid (graded-mesh) generator. The mesh used for the finite-elements analysis was finer at the boundaries of the different domains, particularly near the lead tip (minimum cell length: 0.1 mm; element growth rate: 1.35; total number of elements: 156 775), and coarser in the homogeneous areas, to limit the complexity of the model. To evaluate the temperature field around the lead tip, we did an electrostatic analysis, in which the model was excited by a dc voltage between the pigmented portion of the pacemaker electrode and one boundary side of the external domain, which was set at a reference voltage. This excitation simplifies the complexity of the numerical model, inducing a significant increase in spatial resolution.

The electromagnetic equations were coupled with heat-transfer thermal equation through the heat source term Q, according to the relation

$$Q = \frac{1}{2\rho}|E|^2 \sigma \tag{1.1}$$

where E (V m^{-1}) is the electric field in the gel domain, ρ is the density (kg m^{-3}) of the gel and σ the electrical conductivity (S m^{-1}).

The simulation lasted 500 s, with a time step of 10 s and an initial heating phase of 300 s, followed by a 200 s period in which the voltage excitation was turned off. The time required to complete the simulation was about 3 h. We then used the numerical model to evaluate the error associated with temperature measurement using the temperature probes. Since the active temperature sensor is approximately a 0.3 mm diameter half-sphere encapsulated somewhere inside a polymer pigmented jacket which represents the terminal part of the fluoroptic® probe (figure 2), we calculated the average (ΔT_{probe}) and the maximum ($\Delta T_{probe,max}$) temperature increase in the volume covered by this jacket (cylindrical region: radius 0.4 mm, length 3 mm), as well as the maximum temperature increase in the whole domain (ΔT_{max}). The error was quantified as

$$\Delta TLE\%\ (\text{“ \% Local Error”}): \quad \frac{\Delta T_{probe} - \Delta T_{probe,\,\max}}{\Delta T_{probe,\,\max}} \cdot 100 \tag{1.2}$$

$$\Delta TME\%\ (\text{“ \% Maximum Error”}): \quad \frac{\Delta T_{probe} - \Delta T_{\max}}{\Delta T_{\max}} \cdot 100 \tag{1.3}$$

ΔTLE quantifies the error due to the temperature gradient in the area covered by the pigmented portion of the temperature probe, regardless of the actual maximum temperature over the whole domain. ΔTME quantifies the error with respect to the actual maximum temperature increase in the whole domain.

1.2.3. SAR estimation

With the experimental data obtained with the fluoroptic® probes we could estimate the local SAR by calculating the slope (dT/dt) of the initial temperature increase, following the method indicated in the IEEE C95.3-2002 [24]. Such procedure leads to uncertainties of about ±1–2 dB in the local SAR evaluation.

The slope of the interpolating line was estimated by minimizing the R-error over about 40 samples; this estimation was assumed valid when the Pearson coefficient r2 was greater than 0.98.

In the numerical model, the SAR was estimated by calculating the initial dT/dt of the average temperature increase on the volume of the terminal pigmented part of the temperature probe. Over a period of 10 s, with a time step of 0.1 s, SAR was calculated by minimizing the R-error over about 40 samples.

The SAR error was calculated using the same procedure as for the temperature: in the numerical model the SAR was estimated for the maximum local SAR and the mean SAR in the volume covered by the

temperature probes (calculated respectively from the maximum and the mean temperature increase). The percentage measure error associated with different temperature probe positions is expressed as follows:

SLE% (“ % Local Error”): $$\frac{SAR_{probe} - SAR_{probe,\,\max}}{SAR_{probe,\,\max}} \cdot 100 \qquad (1.4)$$

SME% (“ % Maximum Error”): $$\frac{SAR_{probe} - SAR_{\max}}{SAR_{\max}} \cdot 100 \qquad (1.5)$$

where $SAR_{probe,max}$, SAR_{probe}, SAR_{max} are the values of SAR calculated from the maximum temperature increase in the area covered by the temperature probe, from the average temperature rise in the same area, and from the maximum temperature increase in the whole domain, respectively.

1.3 Results

1.3.1. Influence of temperature probe positioning on temperature and SAR underestimation

Figure 4 shows the pacemaker lead tip temperature increases measured with four temperature probes in different positions. The three graphs refer to 25 MHz, 64 MHz and 128 MHz, with an average net power of 0.7 W, 1.36 W and 2.04 W, respectively. These power levels were chosen to obtain heating comparable to those reported in the literature [1,3,6,14]. A detailed investigation of the effect of the frequency on the amount of heating, for a given power, was not attempted since it was not relevant to the aim of this study.

We found that the position of the temperature probe significantly affects the measurement: transversal contact between the side of the temperature probe and the circular surface of the lead tip (figure 2(a)) is the configuration which leads to the highest measured temperature. We define the temperature measured with other positions than that leading to the maximum value as an underestimation (figure 5). The highest temperature underestimation was obtained at 25 MHz and it decreases as the frequency increases, regardless of the temperature probe contact. The configurations ‘tip-to-side’ (figure 2(b)) and ‘tip-to-tip’ (figure 2(c)) resulted in temperature underestimation ranging from 28% to 39%. The underestimation associated with the side-to-side contact was significantly lower (4–7%).

The underestimation associated with the estimation of local SAR at the lead tip showed a similar behaviour: transversal contact between the side of the temperature probe and the circular surface of the lead tip (figure 2(a)) is the configuration measuring the highest SAR (1444 W kg^{-1}). The underestimation associated with other temperature probe configurations is reported in figure 5, lower panel. In the worst case, the SAR underestimation can be up to 75%. The effect of the frequency on SAR underestimation was similar to that observed for the temperature.

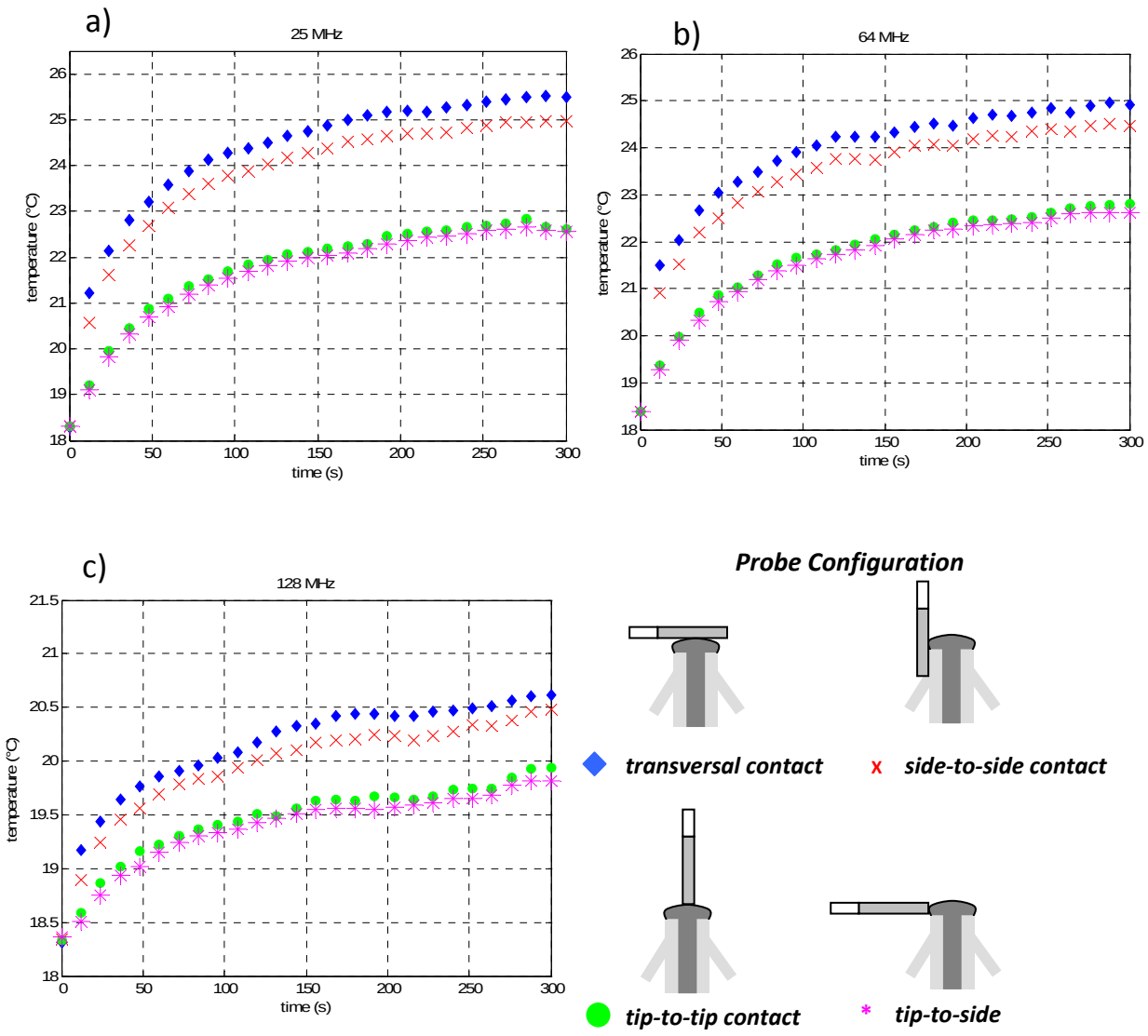

Figure 4. Temperature rise measured by temperature probes in different positions: transversal contact (diamonds); tip-to-side contact (x-marks); tip-to-tip contact (dots); side-to-side contact (stars). Frequency excitation signal: 25 MHz (a), 64 MHz (b), 128 MHz (c).

1.3.2. Validation of the thermal model

For best fitting with experimental measurements at 25, 64 and 128 MHz we applied on the pacemaker lead tip a voltage of 7, 11.5 and 12 V, respectively. Figure 6 shows the numerical and experimental data. The excitation was active for 300 s following by a 200 s cooling phase. We positioned the temperature probes in transversal position with the lead at 2 mm, 4 mm and 6 mm from

the tip (solid lines). The computed temperature distribution was sampled at the same position of the pigmented portions of the temperature probes. For each of these positions we then calculated the average temperature over the volume covered by the pigmented portions of the temperature probes.

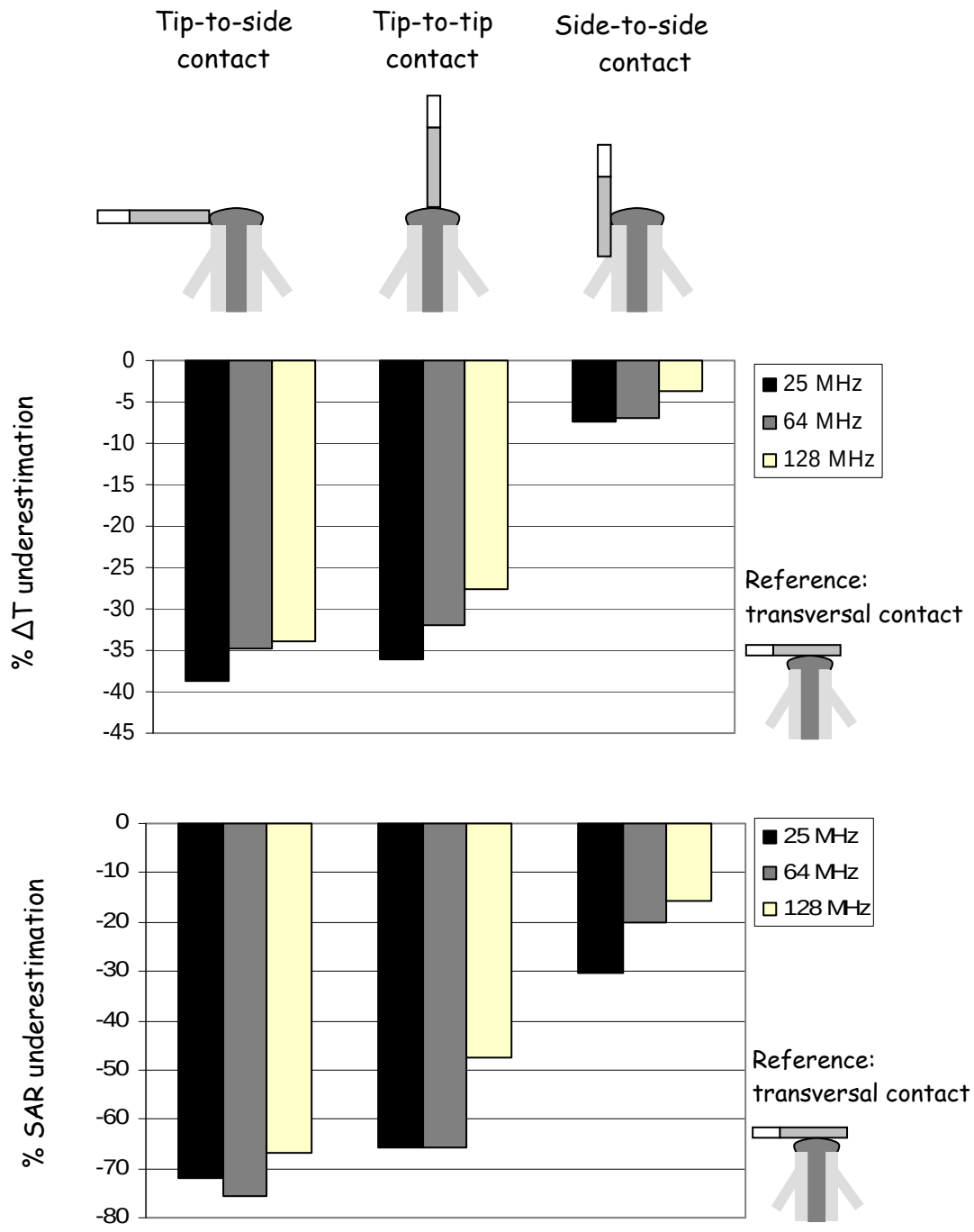

Figure 5. Underestimation: Comparison among measurements made by a temperature probe in transversal contact with the active pacemaker lead (conf. a) and underestimation obtained with other contact configurations (conf. b, c, d): temperature and SAR comparison.

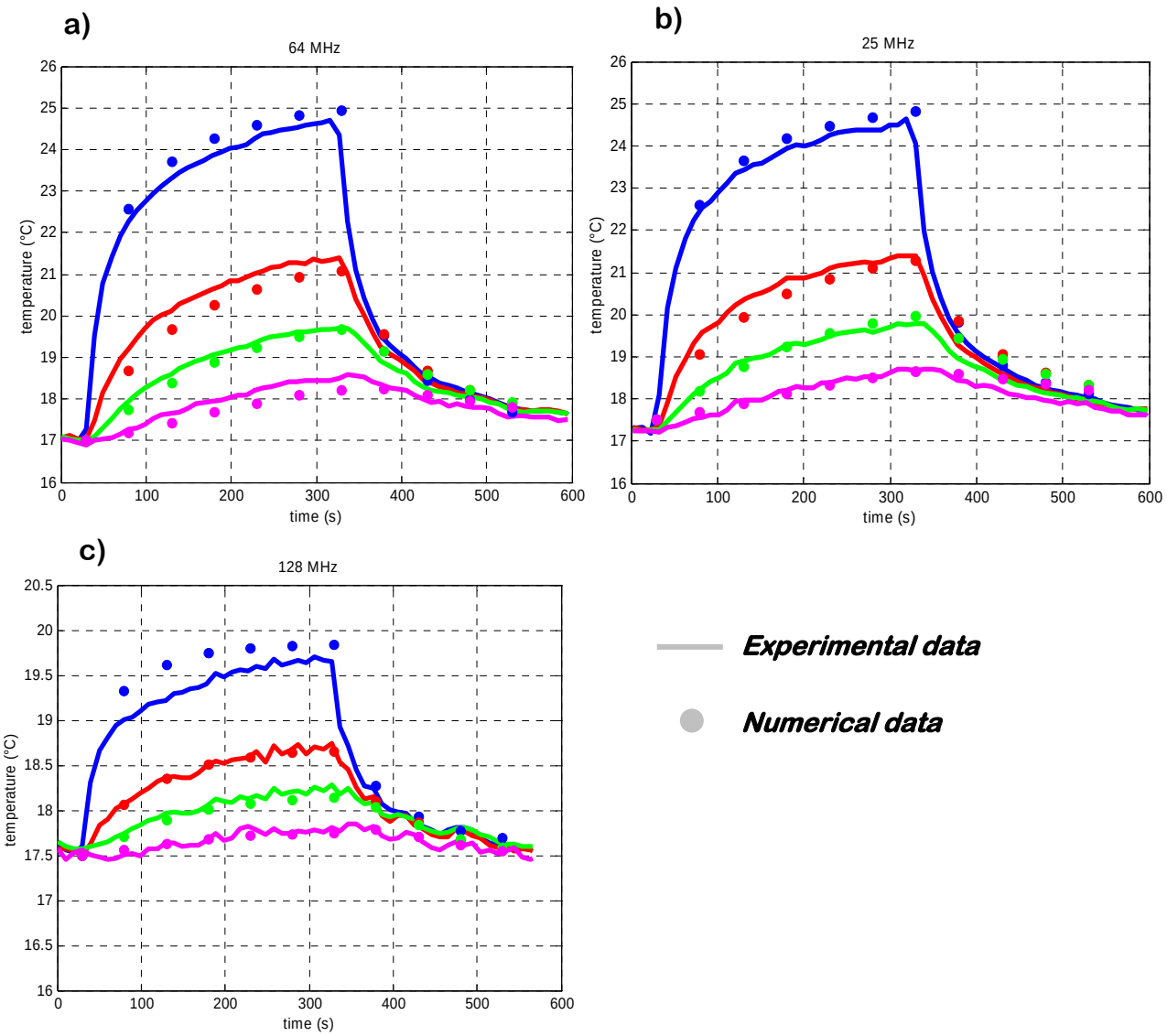

Figure 6. Validation of the model: experimental data (solid lines) were compared with temperature distributions from computer simulations (dots). Excitation signal was set at 25 MHz (a), 64 MHz (b), and 128 MHz (c). For each frequency, heat distribution was characterized by sampling temperature at the lead surface and at 2 mm, 4 mm and 6 mm from the tip. Note that temperature scale of panel c) differs from the others.

The numerical results reproduced the temperature increase measured at 25 and 64 MHz. For each temperature curve, the difference between experimental and numerical results was within the resolution of the fluoroptic® temperature probes (0.1 °C), in both the heating and cooling phase. The numerical model also showed a good agreement with experimental data in terms of spatial distribution of the temperature field: at each distance the difference between experimental and numerical results was comparable for all temperature probes. At 128 MHz the numerical model showed a poorer fitting of the temperature rise, even though at the end of the heating phase the spatial distribution of the temperature was in agreement with the experimental data.

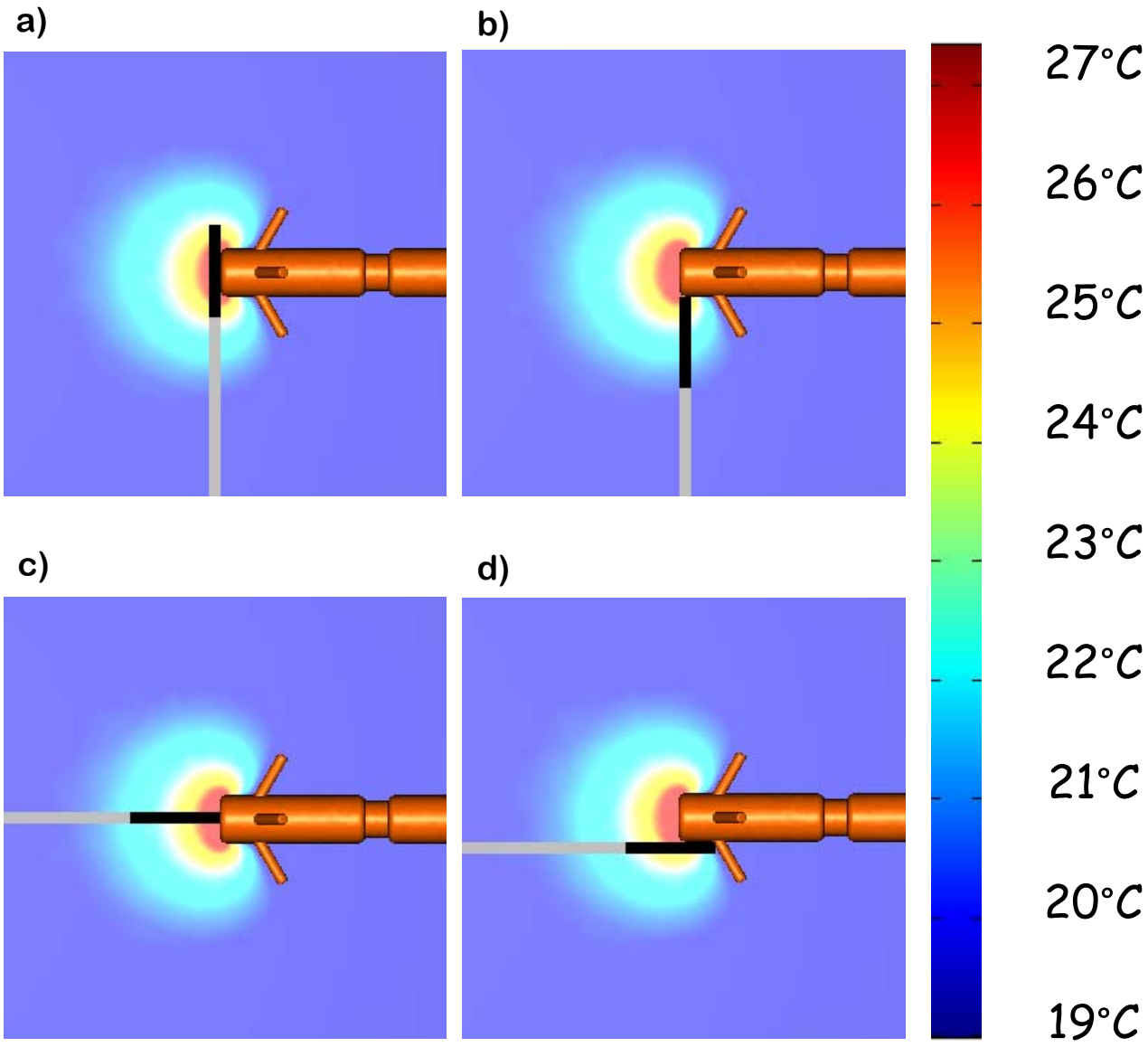

Figure 7. Temperature field resulting from the numerical model. The different contact configurations for the probes are also shown: (a) transversal contact; (b) tip-to-side contact; (c) tip-to-tip contact; (d) side-to-side contact. Temperature gray-map is valid only for the gelled domain, but not for the probes and the lead.

1.3.3. Influence of temperature probe positioning on temperature and SAR error

As illustrated in figure 7, the spatial temperature gradient around the lead tip was very high, which indicates that the physical dimension of the temperature probes may not be neglected. The measurement error was related to the positioning of the terminal portion of the temperature probes in which the active sensor is encapsulated and which covers a volume with large spatial temperature gradients. The values of the local and maximum temperature and SAR errors are reported in figure 8. The transversal contact between the temperature probe and the configuration associated with the lowest maximum errors, both for temperature and SAR measurements.

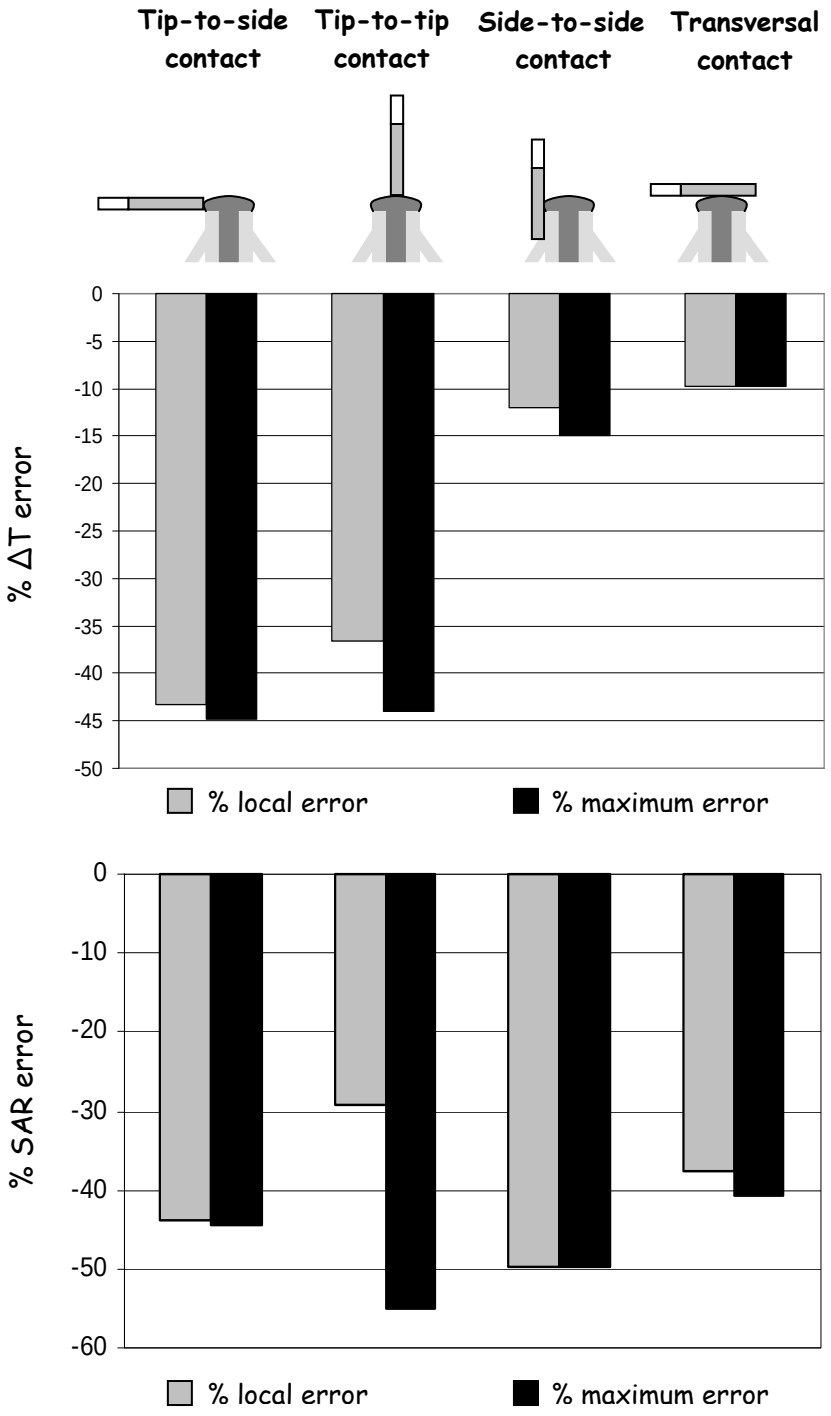

Figure 8. Numerically calculated error associated with temperature increase and SAR measures obtained from fluoroptic® probes. For each contact configuration the error is expressed in terms of local error (referred to the highest temperature in the area covered by the pigmented portion of the probe) and maximum error (referred to the highest temperature in the whole domain).

The maximum error in the measurement of temperature increase (−45%, absolute error: −4 °C) was yielded by the tip-to-side contact, while the positioning resulting in the lowest underestimation (transversal contact) also resulted in the lowest error, i.e., −10% or as absolute error −0.9 °C.

The error associated with SAR measurement was higher than those of temperature (range −30 to 54%); in addition, the positioning of the temperature probes played a minor role for the SAR error. The transversal contact was always the configuration associated with the lowest maximum SAR error (percentage error: −41%, absolute error: −1069 W kg^{-1}).

1.4 Discussion

Using temperature measurements on a physical model of a pacemaker lead we found that the positioning of temperature probes strongly affects temperature and SAR results. Due to the comparable dimension of the temperature probes with the pacing electrode and due to the large spatial temperature gradient around the lead tip, temperature probes tend systematically to underestimate the real value of local temperature and SAR. In particular, using the SMM Luxtron fluoroptic® probes, we found that a transversal contact of the temperature probe with the lead tip always gives the highest temperature and SAR values. Such a result points out that the active sensor is likely to occupy the central region of the pigmented jacket of the temperature probe. Assuming this configuration as reference, the underestimation yielded by other configurations may be as high as 39% for temperature and 75% for SAR.

The experiments allowed us to identify the temperature probe configuration for measuring the highest temperature increase but could not give us the temperature and SAR error. Since the active temperature sensor is placed somewhere inside the terminal pigmented portion of the probe, which covers an area with significant temperature gradients, the measured temperature needs to be averaged over the pigmented jacket. Therefore we developed a numerical model to quantify this error. The model was validated by comparing the numerical results with the experimental measures obtained with fluoroptic® probes in the transversal contact configuration, at 2, 4 and 6 mm from the lead tip. With this configuration we characterized both time and space distribution of the temperature. Due to the physical dimensions of the lead and the spatial resolution, required for consistent temperature estimation, Maxwell's equations were solved under electrostatic approximation. The correspondence between experimental and numerical data was confirmed at 25 and 64 MHz in both the time-transient heating and cooling phases. The spatial distribution of the temperature showed good agreement with the data sampled at various distances from the tip (0, 2, 4, 6 mm). The worst fitting was obtained at 128 MHz, specifically in the dynamical rise of temperature. This suggests that the heat generation at 128 MHz begins to be affected by displacement currents.

Simulated results are consistent with experimental data: the temperature gradient around the lead tip is high enough that the physical dimensions of the temperature probes must not be neglected. As a consequence, the measurement of the temperature increase is always too low. In the best case (transversal contact) the maximum error is about −10%, but can be as high as −45% in the worst case (tip-to-side contact).

The error associated with the measurement of local SAR is higher than the temperature error. SAR is calculated as the slope of the initial linear temperature increase and is therefore affected by the spatial distribution of the temperature in the first instants of the heat generation process. Thus, the effect of the dimensions of the physical probe is higher than at steady state. After about 300 s the temperature distribution became more homogenous, consequently reducing the error. In agreement with experimental data, the SAR error is also less sensitive to probe positioning than temperature measures. The maximum error for SAR is about −40% for the transversal contact position but can go up to −54% for the tip-to-tip contact. Also, the temperature probe position leading to the lowest underestimation has the lowest error for temperature and SAR measurements as well.

The physical model adopted in this work reproduced the lead tip heating but not the current-induction of an MRI system. Future analysis could be extended to pacemaker lead tip temperature measurements with temperature probes during real MRI systems. Furthermore, thermal events at the tip of a pacemaker lead are the same for all linear conductive structures with comparable dimensions; this fact suggests the possibility of extending the results of this work to other medical devices commonly used under MRI guidance, such as guide wires and catheters in interventional therapy.

In addition, our data show a frequency dependence of the underestimation in temperature and SAR measurements. The aim and the design of our study do not allow an explanation of this phenomenon. Such an explanation would require a deeper and dedicated analysis, which was beyond this study.

The investigation of the temperature and SAR errors yielded by other fluoroptic® probe types, such as surface and remote style probes, was beyond the aim of this paper. The SMM probes were chosen because they can guarantee a reliable contact even with very thin wires. In addition, since heating is generated at the interface between metallic structure and gel, surface contact probes would not be located in the actual hot spot area.

1.5 Conclusions

The results showed the sensitivity of these measurements on temperature probe contact positioning. The transversal contact of the pigmented portion of the temperature probe and the lead tip minimized the underestimation for temperature and SAR and therefore gave always the highest values for this type of pacemaker lead. Other contact configurations may cause a temperature underestimation of up to 39% and a SAR underestimation of up to 75%. For all contact configurations the transversal contact showed the lowest maximum temperature error (−10%) and the lowest maximum SAR error (−40%). The maximum temperature error can be as high as −45% for the tip-to-side configuration whereas the maximum SAR error is highest for the tip-to-tip configuration (−54%). For all MRI heating evaluations with temperature probes, a contact position leading to the lowest maximum error should be used and the error should be specified. Scientific sound MRI heating evaluations need to be accompanied by a thorough uncertainty

budget. Therefore, other uncertainty factors should also be evaluated when specifying temperature and SAR values on implants based on measurements with fluoroptic ® temperature probes.

Disclaimer

The opinions and conclusions stated in this paper are those of the authors and do not represent the official position of the Department of Health and Human Services. The mention of commercial products, their sources, or their use in connection with material reported herein is not to be construed as either an actual or implied endorsement of such products by the Department of Health and Human Services.

Acknowledgments

Authorswish to thank Sorin Biomedica Cardio (eng. G. Gaggini) for providing the pacemakers and their leads; Monica Brocco for the linguist revision of the paper.

References

[1] Niehaus M and Tebbenjohanns J 2001 Electromagnetic interference in patients with implanted pacemakers or cardioverter-defibrillators *Heart* **86** 246–8

[2] Pinski S L and Trohman R G 2002 Interference in implanted cardiac devices: part II. *Pacing Clin. Electrophysiol.* **25** 1496–509

[3] Kanal E *et al* 2002 American College of Radiology white paper on MR-safety *Am. J. Roentgenol.* **178** 1335–47

[4] Shellock F G and Crues JVIII 2002 MR-safety and the American College of Radiology white paper *Am. J. Roentgenol.* **178** 1349–52

[5] Dumoulin C L, Souza S P and Darrow R D 1993 Real-time position monitoring of invasive devices using magnetic resonance *Magn. Reson. Med.* **29** 411–5

[6] Leung D A, Debatin J F, Wildermuth S, McKinnon G C, Holtz D, Dumoulin C L, Darrow R D, von Hofmann E and Schulthess G K 1995 Intravascular MR tracking catheter: preliminary experimental evaluation *Am. J. Roentgenol.* **164** 1265–70

[7] Glowinsky A, Adam G, Brucker A, Neuerburg van J, Vaals J J and G¨unther R W 1997 Catheter visualization using locally induced, actively controlled field inhomogeneities *Magn. Reson. Med.* **38** 253–8

[8] Atalar E, Kraitchman D L, Carkhuff B, Lesho J, Ocali O, Solaiyappan M, Guttman M A and Charles H K Jr 1998 Catheter-tracking FOV MR fluoroscopy *Magn. Reson. Med.* **40** 865–72

[9] Baker K B, Tkach J A, Nyenhuis J A, Phillips M, Shellock F G, Gonzalez-Martinez J and Rezai A R 2004 Evaluation of specific absorption rate as a dosimeter of MRI-related implant heating *J. Magn. Reson. Imaging* **20** 315–20

[10] Wickersheim K A and Sun M H 1987 Fluoroptic ® thermometry *Med. Electron. (February)* 84–91

[11] Shellock F G 1992 Thermal responses in human subjects exposed to magnetic resonance imaging *New York Acad. Sci.* **649** 260–72

[12] Blouin L T, Marcus F I and Lampe L 1991 Assessment of effects of a radiofrequency field and thermistor location in an electrode catheter on the accuracy of temperature measurement *Pacing Clin. Electrophysiol.* **14** 807–13

[13] Shellock F G, Schaefer D J and Kanal E 1994 Physiologic responses to an MR imaging performed at a specific absorption rate of 6.0 W/kg1 *Radiology* **192** 865–8

[14] Dinerman J L, Berger R D and Calkins H 1996 Temperature monitoring during radiofrequency ablation *J. Cardiovasc. Electrophysiol.* **7** 163–73

[15] Shellock F G and Shields C L Jr 2000 Radiofrequency energy-induced heating of bovine articular cartilage using a bipolar radiofrequency electrode *Am. J. Sports Med.* **28** 720–4

[16] Achenbach S, Moshage W, Diem B, Bieberle T, Schibgilla V and Bachmann K 1997 Effects of magnetic resonance imaging on cardiac pacemakers and electrodes *Am. Heart J.* **134** 467–73

[17] Sommer T *et al* 2000 MR imaging and cardiac pacemakers: in-vitro evaluation and in-vivo studies in 51 patients at 0.5 T *Radiology* **215** 869–79

[18] Nitz W R, Oppelt A, Renz W, Manke C, Lenhart M and Link J 2001 On the heating of linear conductive structure as guide wires and catheters in interventional MRI *J. Magn. Reson. Imaging* **13** 105–14

[19] Ruggera P S, Witters D M, von Maltzahn G and Bassen H I 2003 *In vitro* assessment of tissue heating near metallic medical implants by exposure to pulsed radio frequency diathermy *Phys. Med. Biol.* **48** 2919–28

[20] RoguinA, ZvimanMM, MeiningerGR, Rodrigues E R, Dickfeld TM, BluemkeDA, Lardo A, Berger RD, CalkinsH and Halperin H R 2004 Modern pacemaker and implantable cardioverter/defibrillator systems can be magnetic resonance imaging safe. In vitro and in vivo assessment of safety and function at 1.5 T *Circulation* **110** 475–82

[21] American Society for Testing and Materials (ASTM) 2004 Standard test method for measurement of radio frequency induced heating near passive implants during magnetic resonance imaging *ASTM Designation*: F2182-02a

[22] Chang I 2003 Finite element analysis of hepatic radiofrequency ablation probes using temperature-dependent electrical conductivity *Biomed. Eng. Online* **2** 12

[23] Solazzo S A, Liu Z, Lobo SM, Ahmed M, Hines-Peralta A U, Lenkinski R E and Goldberg S N 2005 Radiofrequency ablation: importance of background tissue electrical conductivity—an agar phantom and computer modeling study *Radiology* **236** 495–502

[24] IEEE 2002 Recommended practice for measurements and computations with respect to human exposure to radiofrequency electromagnetic fields, 100 kHz to 300 GHz *IEEE Standard* C95.3-2002 (Institute of Electrical and Electronics Engineers)

Chapter 2

Complexity of MRI induced heating on metallic leads: experimental measurements of 374 configurations

E Mattei[1], M Triventi1, G Calcagnini[1], F Censi[1], W Kainz[2], G.Mandoza[2], H I Bassen[2] and P Bartolini[1]

[1] Department of Technologies and Health, Italian National Institute of Health, Roma, Italy

[2] Center for Devices and Radiological Health, Food and Drug Administration, Rockville, MD, USA

Published on BioMedical Engineering OnLine 2008, 7:11

Abstract

MRI induced heating on PM leads is a very complex issue. The widely varying results described in literature suggest that there are many factors that influence the degree of heating and that not always are adequately addressed by existing testing methods. We present a wide database of experimental measurements of the heating of metallic wires and PM leads in a 1.5 T RF coil. The aim of these measurements is to systematically quantify the contribution of some potential factors involved in the MRI induced heating: the length and the geometric structure of the lead; the implant location within the body and the lead path; the shape of the phantom used to simulate the human trunk and its relative position inside the RF coil. We found that the several factors are the primary influence on heating at the tip. Closer locations of the leads to the edge of the phantom and to the edge of the coil produce maximum heating. The lead length is the other crucial factor, whereas the implant area does not seem to have a major role in the induced temperature increase. Also the lead structure and the geometry of the phantom revealed to be elements that can significantly modify the amount of heating. Our findings highlight the factors that have significant effects on MRI induced heating of implanted wires and leads. These factors must be taken into account by those who plan to study or model MRI heating of implants. Also our data should help those who wish to develop guidelines for defining safe medical implants for MRI patients. In addition, our database of the entire set of measurements can help those who wish to validate their numerical models of implants that may be exposed to MRI systems.

2.1 Introduction

Magnetic resonance imaging (MRI) has become the imaging procedure of choice for extensive clinical evaluation and diagnosis. Unlike conventional radiography and computed tomographic imaging, which make use of potentially harmful radiation (X-rays), MRI has many advantages, including its no ionizing nature and the unparallel ability to discriminate different soft tissues without contrast media. However, the substantial benefits of MRI are often denied to patients known to have implanted medical devices such as pacemakers (PM) and implantable cardioverter devices (ICD). The outstanding increases in both MRI usage and cardiac device-based therapy have resulted in an estimated 50–75% probability of a patient being indicated for an MRI over the lifetime of their device [1,2]. MRI induced heating is one of the known risks for implanted PM and ICD: the RF field energy generated during MRI procedures may be coupled into conductive leads in two major ways [3]:

1) The conductive lead acts as an antenna capable of receiving and supporting the frequency of the MRI unit's RF field (63.8 MHz for 1.5 Tesla systems or 127.6 MHz for 3.0 Tesla systems). This mechanism can create the resonant waves.

2) The implant acts as an electrical "short circuit" to the electrical potentials induced within the body by the MRI RF field.

Each of these effects induces a RF current which flows from the lead into the surrounding tissues. As a consequence of the high electrical resistance of these tissues, resistive heating is then generated at the lead-tissue interface, causing a temperature increase that could be dangerous for the patients. The scientific and medical literature clearly shows that the MRI-induced heating on metallic leads cannot be immediately neglected:

Sommer et al. [4] demonstrated the potential for heating as much as 23.5°C at specific absorption rate (SAR) levels of only 1.3 W/kg in a 0.5 Tesla MRI unit. Achenbach et al. [5] reported pacing lead tip temperature elevation in leads not attached to an implanted pulse generator (IPG) of >63°C during 90 seconds of MRI. Roguin [6] observed in an animal model a lose capture for 12 hours following an MRI, concluding that "... some edema occurred at the tip-lead tissue interface, which subsequently resolved." Martin and Coman [7] observed 9.4% of their patients undergo "significant" changes to their pacing thresholds after MRI. Konings et al. [8] reported heating around intravascular guide wires by resonating RF waves of 26°C to 74°C after 30 seconds. Bassen et al. [9] measured a temperature rise of about 0.5°C (local SAR = 320 W/kg) for a stent exposed to the RF field of a 1.5 T MRI birdcage coil at 64 MHz; using the same experimental set-up, a temperature increase of 8.6°C was observed at the bare end of an insulated 24-cm long wire (local SAR = 5680 W/kg). Rezai et al. [10] reported deep brain stimulator temperature elevations at the electrode tip of >25°C within 15 minutes of MR imaging. This data is particularly disturbing when one realizes that thermal ablation procedures are typically performed at temperatures of approximately 50–60°C. At the same time, over 300 patients to date have been scanned without any significant clinical difficulty or complication [11].

Such widely varying results indicate how the performance of an implanted or interventional device undergoing MRI is a very complex problem. While it is relatively easy to demonstrate a heating or induced voltage problem, it is far more difficult to prove a solution to these problems, due to the complex and unpredictable nature of the MRI interaction. Several factors influence the degree of heating: the whole body specific absorption rate, the patient position in the coil, the type of imaging sequence, the patient characteristics, the duration of imaging procedure, the body structure being imaged, the type and position of transmit coil, the lead design, the lead orientation within the patient, the degree of perfusion near the device, the temperature measurement procedure, the respiratory phase, etc. Many of these parameters are currently either not recognized or inadequately addressed by existing testing methods [3]. In a previous study we investigated the variability in temperature and SAR measurements using fluoroptic® temperature probes on the tip of a PM lead [17].

In this paper we present a wide database of experimental measurements of the heating of metallic wires and PM leads in a 1.5 T RF coil. The aim of these measurements is to systematically quantify the contribution of some potential factors involved in the MRI induced heating: the length and the geometric structure of the lead; the implant location within the body and the lead path; the shape of the phantom used to simulate the human trunk and its relative position inside the RF coil. In addition, the data collected will serve as an open-access experimental database for numerical models validation.

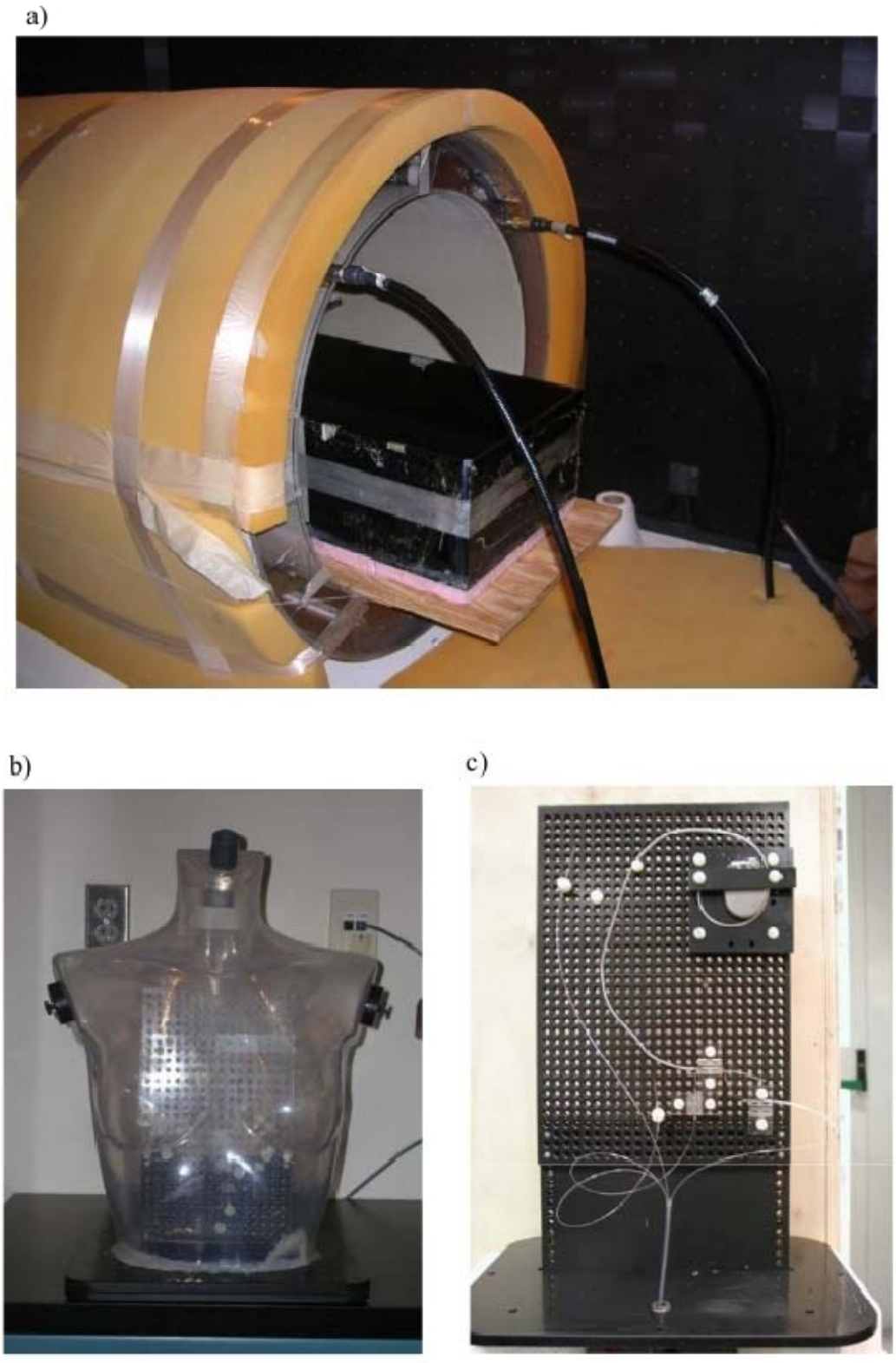

Figure 1. RF coil and phantoms. a) MRI birdcage coil with rectangular box phantom inside coil; b) PVC grid placed inside the phantom to support the pacemaker implant and the fluoroptic® temperature probes; c) Human-shaped phantom filled with HEC gel.

2.2 Materials and methods

2.2.1 Exposure System

We performed temperature measurements at the Center for Device and Radiological Health (CDRH), Food and Drug Administration (FDA) in Rockville, MD, USA. We used a full-size RF coil (length 113 cm, inner diameter 62 cm) with 16 legs forming the classic Birdcage configuration (Figure 1a).

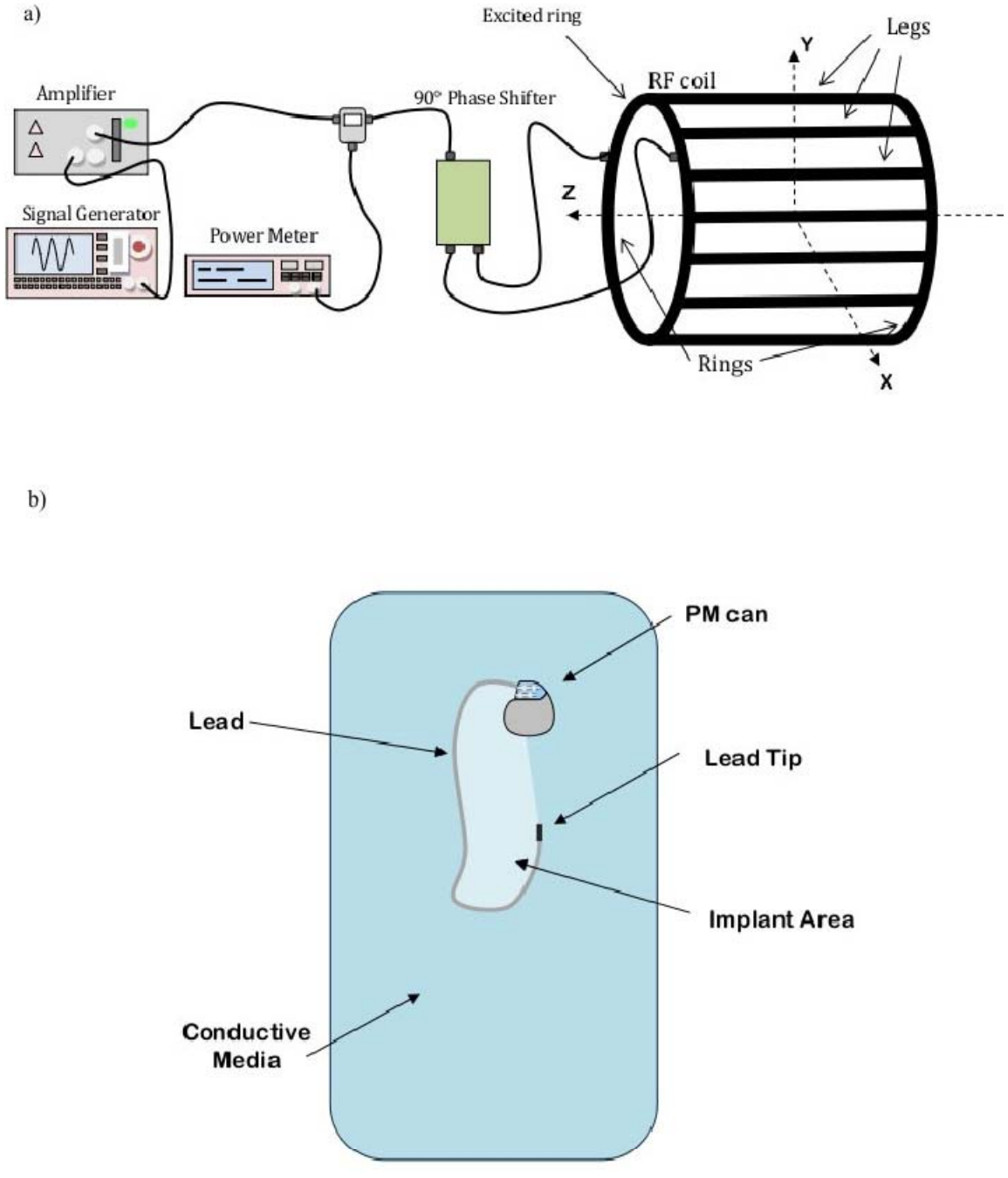

Figure 2. Experimental set-up and terminology. a) Experimental set-up and MRI coil configuration terminology; b) Sketch and terminology for a PM implants.

Tuning capacitors are placed on each of the legs, resulting in a low-pass structure. This system is the same as those used in 1.5 T clinical systems. The coil was fed by a quadrature power divider so to produce a circularly polarized B1 fields. The birdcage coil was housed in an anechoic chamber and the exposure was realized by a RF amplifier that delivers over 130 Watts at 64 MHz.
A schematic representation of the experimental set-up used is shown in Figure 2a.

2.2.2. Phantoms

We used two geometries as human trunk simulator: a rectangular plastic box (Figure 1b) and a PVC human-shaped phantom (Figure 1c). Both phantoms were filled with a saline gel composed of Hydroethylcellulose gelling agent (HEC) and NaCl to meet the general requirements of the ASTM F2182-02a standard for testing of MRI heating of implants [12].
The mixture we used produced conductivity at 64 MHz of about 0.7 Sm-1, corresponding to a salinity of about 0.4% by weight, and permittivity of 79. The amount chosen for the HEC (2% by weight) allowed implants to be placed in the gel, moved and replaced, but, at the same time, provided a barrier to rapid thermal convection. Any art voids that are created by movements of implants filled in less than 20 minutes.
The rectangular box phantom (35 × 61 × 19 cm deep) was filled to a depth of 11.5 cm with the gel. The dimensions conformed to the ASTM 2182 standard [12], except for the width of our box. This was narrower than the ASTM specifications to allow the phantom to fit in the RF coil (62 cm inner diameter).
The total amount of gel was 24.6 l, corresponding to a weight of 24.7 kg. The box was surrounded with 2.6 cm of rigid foam for thermal insulation and it was placed on a wood board about 10 cm far from the bottom of the RF coil (Figure 1a). This foam allowed us to perform calorimetry studies to determinate the whole body SAR induced in the phantom. A 26 × 18 cm grid was submerged in the gel to support the implants and maintained a consistent separation distance between the metallic structures, the phantom gel surface and the temperature probes. The grid was adjusted so that the top of the implant was positioned 2 cm below the phantom surface, which resulted in a final position of the grid about 10 cm down the centre of the coil, along the vertical transversal axis (y axis – Figure 2a).
The human-shaped trunk simulator was designed and built at the Dept. of Technology and Health of the National Institute of Health in Rome. The simulator consists of a torso-shaped transparent PVC phantom of the size of a 45 kg female and of an internal volume of 25 liter. The pacemaker and its leads were fixed on a PVC grid placed inside the phantom (Figure 1b).
Both the rectangular box and the human-shaped phantom were placed in various positions inside the RF coil: in this way, we could compare the heating induced on the same implant configurations, but with the phantom differently positioned respect to the coil. The MRI coil configuration and axes are shown in Figure 2a. The terminology for implants is illustrated in Figure 2b.

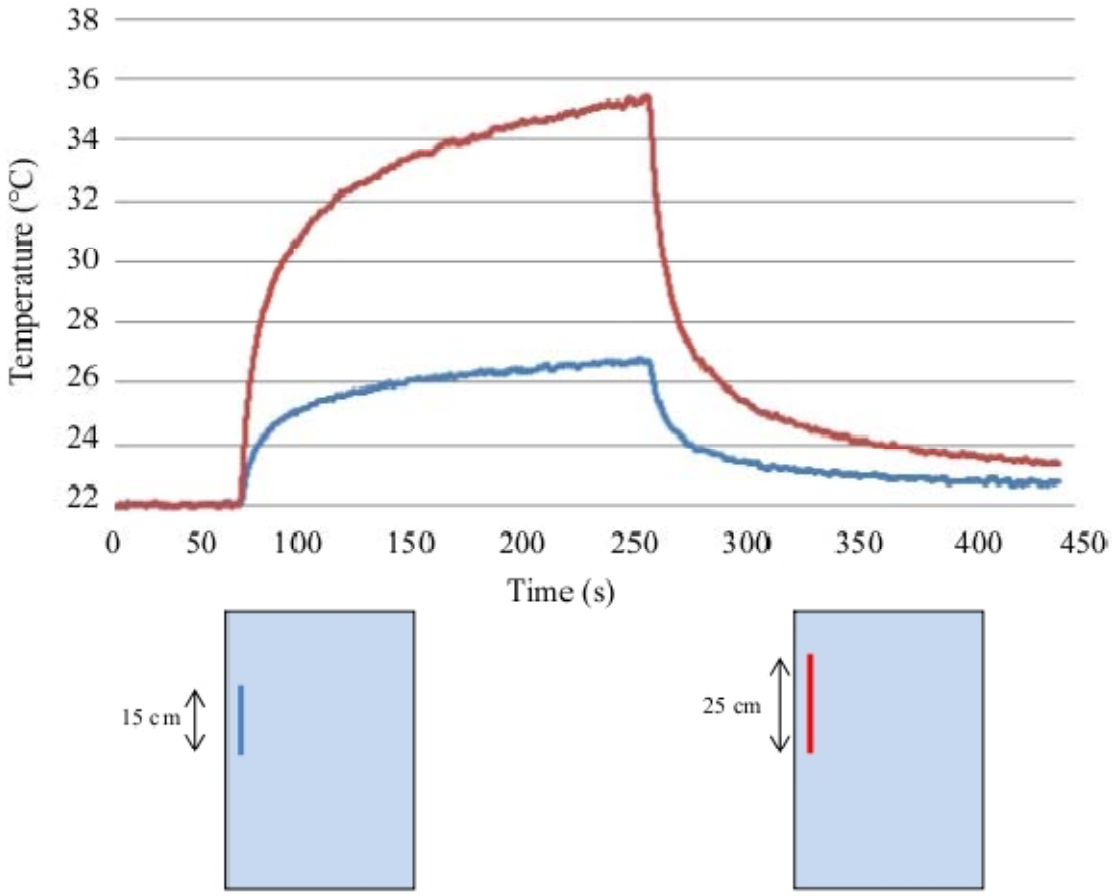

Figure 3. Temperature increase at the lead tip. Example of temperature increase versus time curves measured with fluoroptic® probes at the tip of the implant, during the experiments inside the RF coil. The two lines refers to the configurations reported below.

2.2.3. Implants

The measurements we performed aimed at the identification of the major contributes involved in the heat generation: (1) the position of the implant inside the phantom, (2) the length of the wire and, the thickness of the insulation sheath, (3) the wire geometries (shape) and (4) its position of the implant including its lead with respect to the RF coil. In the following pages, we use the term "configuration" (config.) to refer to a single experimental setup; for each configuration we measured the temperature increase and we estimated the local SAR. The proposed configurations were properly modified from one another in order to investigate the specific contributes to the heating of the four factors previously mentioned. Inside the rectangular box phantom we first simulated the implant with conductive wires (radius 0.5 mm) of various shapes and length; we tested both bare and insulated wires (insulation thickness 0.5 mm and 1 mm). For the insulated wires, the exposed tip length was 1 mm at only one end of the implant. then we replaced the metallic wires with a dual chamber PM (Elect D, *Sorin Biomedica* CRM, Italy) with its 62 cm-long leads. We tested both unipolar and bipolar leads (mod. S80T and S80TB, *Sorin Biomedica* CRM, Italy), either attached or not to the PM can (metallic case).

In a real PM implant, since the length of the lead may not fit the patient's anatomy and size, the excess length may be wrapped near or around the PM can. As a consequence, the length of the lead and the area covered by the implant can significantly vary from patient to patient, thus creating many configurations of implants. In addition, some papers on MRI safety state that a higher heating is induced at the tips of implants which cover a large area [4,10]. From this point, we dedicated a group of measurements to investigate the effect of the implant area, which is the area delimited by the lead, the PM can and the line connecting the lead tip to the PM center of mass (Figure 3b). In the experiments with metallic wires, we compare the temperature increase for wires of different length but with the same geometry (i.e. same shape) (24 config.) When using a real PM with its lead, we tested several configurations without changing the position of the PM can, whereas the total area of the implant was varied by wrapping the exceeding lead near the PM body or by changing the lead geometry (75 config.). Also the presence of the PM can respect to the unattached lead was investigated (18 config.).

Frequency resonance phenomena in various kinds of linear metallic leads and wires undergoing MRI procedures (e.g. catheters used in interventional radiology) have been hypothesized by several groups [13-15]. Resonance is said to occur when the lead is an integral fraction of a half wavelength [15]. The wavelength of 64 MHz is 4.68 m in air but is almost 12 times smaller in saline (due to the dielectric constant and conductibility of saline). Yeung et al [15] illustrates that a 25 cm wire length is close to the resonant length for 64 MHz. We investigated the contribution of resonance to the heating of the lead length by measuring the temperature rise at the tip of three straight wires of different lengths: 15 cm, 25 cm 40 cm (15 config.)

The implants used in our measurements were placed inside a material with an electrical conductivity greater than zero; thus, the presence of an insulation sheath and its thickness may affect the amount of heating induced at the implant tip by concentrating the "exiting" current from the wire in the saline. We tested both bare wires and wires insulated with thermoplastic sheaths of two thicknesses (0.5 mm and 1 mm) (12 conf).

In clinical practice, the PM chassis may be typically located in the left or right pectoral region of the patient, with a lead path that significantly changes in the two cases. Our interest was to understand if one implant location may be considered safer than the other, concerning the heating induced by the MRI exposure. To this aim, we shaped the metallic wires in order to simulate the two typical implants paths for a PM lead, corresponding to a left and right pectoral implant position. We compared the temperature increase in the two cases (70 config.). Left and right pectoral implants were also studied when using a real PM with its lead (32 conf). In addition, we reproduced several implant configurations, both with metallic wires and real PM leads, which do not correspond to a physiological implant condition, but which could give interesting result in order to understand how the geometry of the implant may affect the amount of the induced heating (114 config.).

With regard to heating of pacemaker leads it has been discussed whether imaging of brain and abdomen may pose potentially less risk than imaging of the thorax [16]. We tried to study this issue performing a

separate group of measures where we moved our phantoms along the main axis of the RF birdcage coil, so to simulate MRI scanning of different organs (48 config.).

For most of the implant structures tested, we compared the temperature increases resulting for the same configurations but placed in different regions of the phantom. We studied this for metallic wires and with actual PM leads. In most of the previous studies published on MRI safety and compatibility with metallic implants, temperature measurements are performed inside human trunk simulators of quite simple geometry (box phantoms, rectangular phantoms with rectangular head). In order to evaluate whether the phantom's shape and geometry is a factor that could affect the amount of heating induced by MRI procedures, we placed a PM lead with its can on the left and right sides of a human-shaped phantom, so to reproduce actual left and right pectoral implants: in this study we used bipolar leads, and the lead paths were chosen to mimic a physiological implant condition (atrial and ventricular stimulation). The importance of the geometry of the phantom was studied by comparing the temperature increases resulting from the same configurations tested first inside the rectangular phantom, then in the human shaped phantom (38 conf). The two phantoms had comparable total volume and were exposed to the same whole body SAR.

In all our experiments we measured the temperature increase and SAR at the tip of a "standard wire" (18-cm long, diameter 1 mm, insulated by thermoplastic tubing with a wall thickness of 0.5 mm)., this wire was always placed in the same location and position inside the phantoms: in this way we had a parameter to evaluate the reproducibility of our measurements. We also used the same wire to create a map of the temperature increase and SAR deposition inside the rectangular phantom, by positioning it in the four corners of the simulator (8 config.). We placed the wires 2 cm far from the edges of the box, orientated both along the Z and Y axis of the coil (a picture of the wire position can be found in the Additional file 1).

2.2.4. Instrumentation

Temperature measurements were performed using a fluoroptic ® thermometer (*Luxtron* model 3100) with four separate model SMM probes. These plastic fiber probes (1 mm diameter) minimize perturbations of RF fields. The Luxtron system was operated at 8 samples per second, with resolution of 0.1°C. The background noise was in the range of Luxtron resolution. The terminal portion of the temperature probes were placed in transversal contact (i.e. the probe is perpendicular to the body of the lead wire axis) with the lead tip: this contact configuration was demonstrated to minimize the measurements error associated to the physical dimensions of the probes. Temperature was also sampled on the PM can and, when using a bipolar lead, on the ring.

Data acquisition was performed using the analog output of the Luxtron thermometer, an A/D converter and a 16-bit acquisition card (National Instrument, DAQCard-AI-16XE-50), installed on a standard notebook computer (Acer 1670, Windows XP OS) In previous studies [9,17] the positions and mounting of the temperature probes yielding the minimum error for temperature and SAR measurements were

investigated. The best positioning is obtained when the Luxtron probe (actually the center of the pigmented part) in direct contact with the lead tip or the ring electrode. In this configuration the Luxtron probe and the lead tip or ring electrode are perpendicular to each other. Care was taken to ensure contact of the sensitive region of the Luxtron probe (center of the pigmented end of the Luxtron probe) and the lead tip or ring electrode. In such conditions the underestimations associated to SAR and temperature measurements are lower than 20%, and 7%, respectively.

2.2.5. Exposure protocols

Each configuration tested inside the RF coil was characterized by a temperature versus time behavior made up of three phases: an initial base signal with no excitation in the coil was acquired for a period of 60 s, followed by a 200 s of exposure and a 200 s cooling phase. As a preliminary study, we performed calorimetry with the rectangular box phantom filled with saline (without gelling agent) to measure the whole body average SAR delivered to the phantom. This allowed us to determine the total power absorbed by the phantom (whole body SAR) [9]. The power supplied to the coil was about 55 W, producing inside the phantom a whole body average SAR of about 1 W/kg. Determining the whole-body SAR would allow us to extrapolate the data we collected in our lab on the heating of PM leads to values that could be expected to occur in a phantom placed in a clinical MRI system. For each temperature increase acquired, we also calculated the local SAR following the method described in IEEE C95.3- 2002 [18]. This method leads to uncertainties of about ± 1–2 dB in the local SAR evaluation. Local SAR at the lead tip was calculated according to the definition of SAR by multiplying the initial slope of the temperature rise (dT/ dt) with the specific heat capacity of the gel [9,19]. We used a slope-determining algorithm to properly select the linear portion of the initial temperature rise. The starting point was defined as the first sharp temperature increase from baseline; the initial linear slope was estimated on the number of samples which maximized the Pearson coefficient (R-squared) of the regression (range 25–50 samples).

2.3 Results

We produced a database of 374 experimental measurement results from our investigation of several parameters affecting MR-induced heating. Results are grouped as a function of the parameter investigated (e.g., position of the implant inside the phantom, area covered by the implant, etc). A total of 58 configurations of implants are reported in this paper. The whole set of measurement data as well as the raw temperature data are provided as Excel sheets in the Additional file 1 (temperature measurements on metallic wires) and Additional file 2 (temperature measurements on PM leads). Significant temperature increases (relative to patient safety) were observed only at the lead tip, while no significant heating occurred either at the PM can or at the ring of bipolar leads. Therefore we report only the temperature

increase at the lead tip. This increase is the absolute difference between temperature immediately before RF exposure and at the end of 200 seconds of exposure. An example of the temperature rise is shown in Figure 3.

2.3.1. Position of the implant inside the phantom

We studied an insulated, straight wire that was 25-cm long and parallel with axis of coil (radius 0.5 mm, insulation thickness 0.5 mm, exposed bare tip length = 1 mm). This wire was placed in the middle of the rectangular box phantom. It produced no significant heating at its tip, whereas the temperature increase measured on the same wire placed close to the edge of the torso simulator was as high as 13°C (Figure 4A).

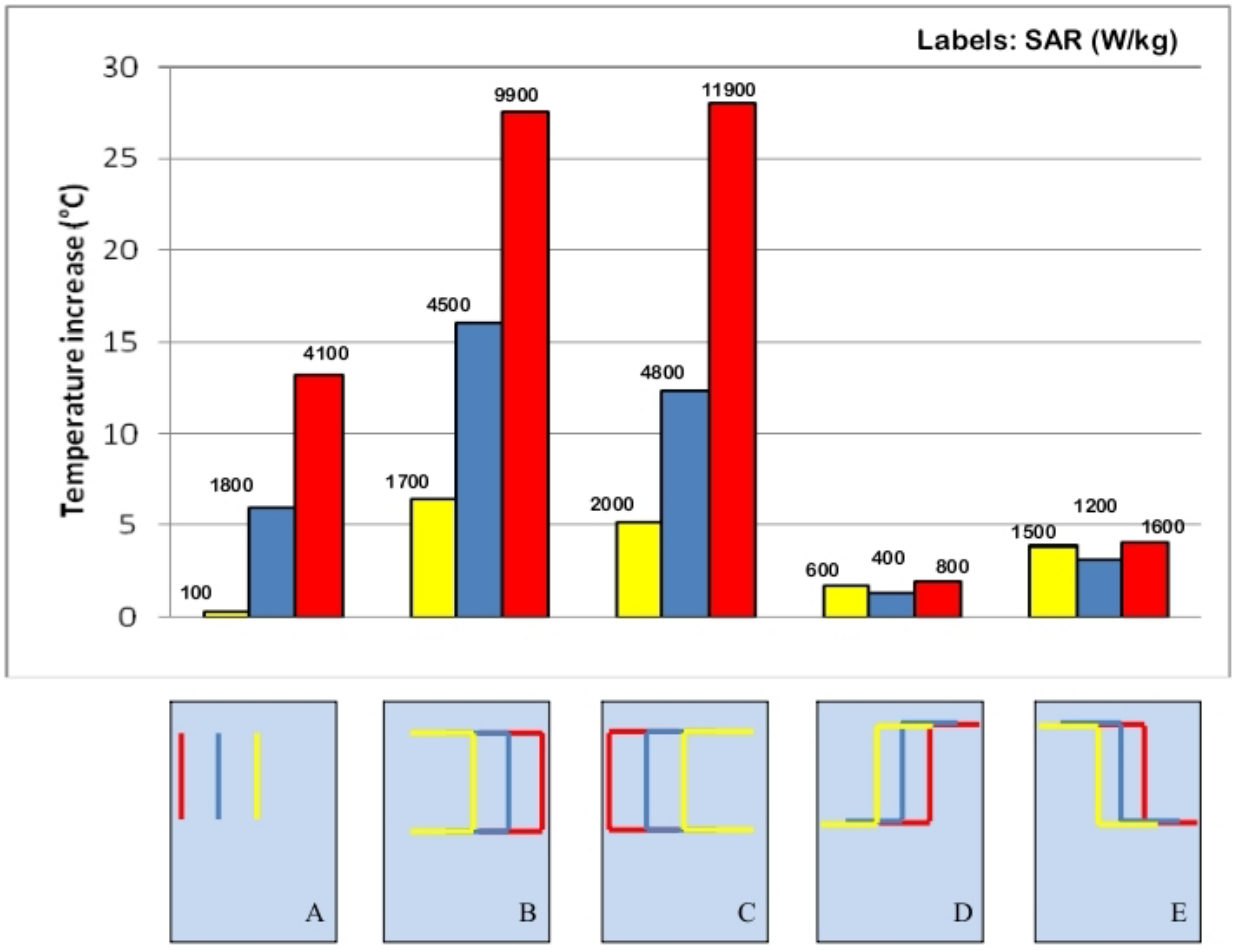

Figure 4. Position of the implant inside the phantom. Temperature increases and SAR measured at the tip of metallic wires placed in different positions inside the phantom. The uncertainty in the reported SAR value is ± 2 dB. Each group of bars refers to the implant configuration reported below.

The effect of the distance from the edge of the phantom is even more marked for longer wires with a complex path. When shaped to simulate a left implant position, with the main straight segment near one

side of the phantom, the induced heating saturated the dynamic range of our of the A/D converter (temperature increase > 30°C). If moved to the central region of the torso simulator, the temperate increase was less than 8°C (Figure 4B–C). The same behavior was as well observed for metallic wire of different shape (Figure 4D–E) and for PM implants, regardless the particular path designed by the lead.
The local SAR values are consistent with the temperature increases: the highest power deposition is always reached in close proximity of the phantom edges.

2.3.2. Length of straight wire implants

Inside the rectangular trunk simulator, we measured the temperature increases at the tip of three straight metallic wires of different length (15 cm 25 cm and 40 cm). Different locations were tested (Figure 5 A–B–C). All the three wires had 0.5 mm-thick thermoplastic insulation, except for the tip (bare for 1 mm). The highest temperature increase (13.5°C) was obtained for the 25-cm long wire (Figure 5 A–B–C). The induced heating was much less for the other two implants (4.3°C and 0.8°C for the 15 cm long and 40 cm-long wire, respectively).
The SAR value are substantially consistent with the temperature increases; the highest SAR was reached at the tip of the 25 cm long wire, when placed close to the border of the rectangular phantom Figure 5C). The 15 cm and 40 cm wires, located in the same position, gave a significant lower SAR.
When the temperature increase are very small (<1°C), the SAR calculation with the method described in the previous section cannot be so accurate and leads to values not so significant.

2.3.3. Area enclosed by the implant

We observed that a leads that formed a square shape and therefore had a large "loop area" (Figure 5D) did not always imply a higher heating. The same lead shape for a smaller implant area obtained by shaping a 25-cm long wire may produce a higher temperature increase than a 50-cm long wire with similar shaping, if placed more peripherally inside the phantom (see the Additional file 1 for details). Only when the main straight segments of the wires are located at the same distance from the phantom edges, the implant that covers a larger area produces a higher temperature increase at its tip (Figure 5D–E). In the same way, a no-loop PM implant (i.e. an implant with the lead that is not wrapped around the PM can) covered an area almost double than the one of a one-loop configuration (the lead makes one loop around the PM can): the former caused a temperature increase significantly higher (> 15°C) than the latter when both of the PM leads are placed near the border of the rectangular box simulator (Figure 6D). After moving both implants in the central region of the phantom, the major heating was obtained for the one-loop configuration (4°C versus 1°C of the no-loop implant; Figure 6C). Such results show that more than the area, the actual contribute to the heating is the length of the segments of the implant places next to the edge of the phantom. A similar behavior was as well observed by comparing the SAR values: the highest deposited power is reached at the tip of those implants that have long straight segment close to the borders of the phantom.

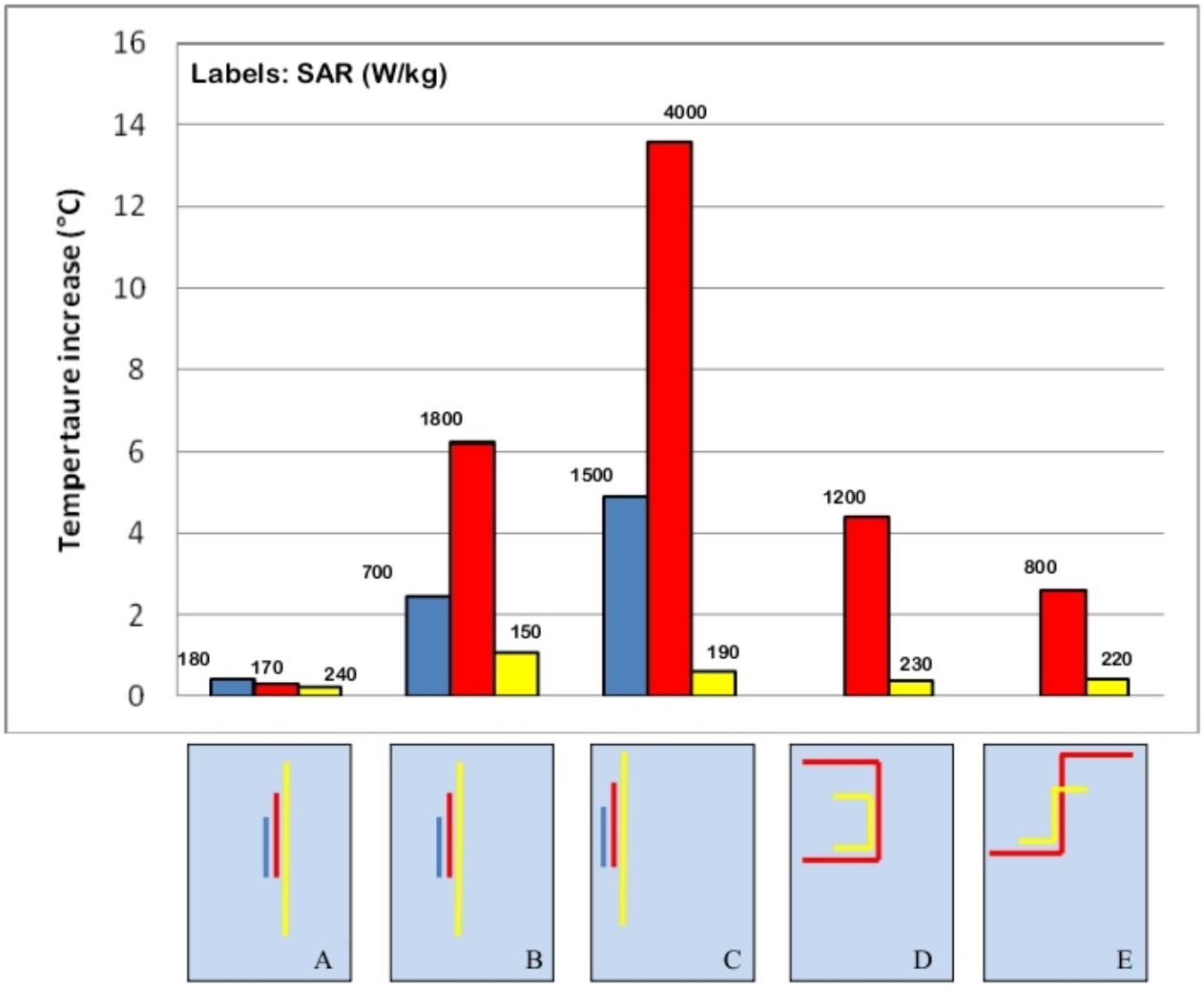

Figure 5. Length of wire implants. Temperature increases and SAR measured at the tip of metallic wires of different lengths (15 cm, 25 cm and 40 cm – A, B, C; 25 cm and 50 cm – D, E). The uncertainty in the reported SAR value is ± 2 dB. Each group of bars refers to the implant configuration reported below.

2.3.4. Geometry and structure of the lead

Experimental measurements of metallic wires in phantoms showed significant differences between left and right pectoral implants. In particular, with the exposed tip in the left region of the rectangular phantom (in the physiological position of the heart ventricles), the right-implant wire, that is the wire shaped to simulate the lead path from the right pectoral region to the heart ventricle, produced a temperature increase of 2.6°C whereas for the left-implant wire (shaped to reproduce the lead path from the left pectoral region to the heart ventricle) we measured a temperature increase barely higher than 1°C (Figure 6A). An opposite configuration, with the tip of the two wires in the right region of the box simulator, produced opposite results: the highest heating was obtained for the left-implant wire (temperature increase of 3°C), whereas the temperature at the right-implant wire rose of less than 1°C (Figure 6B).

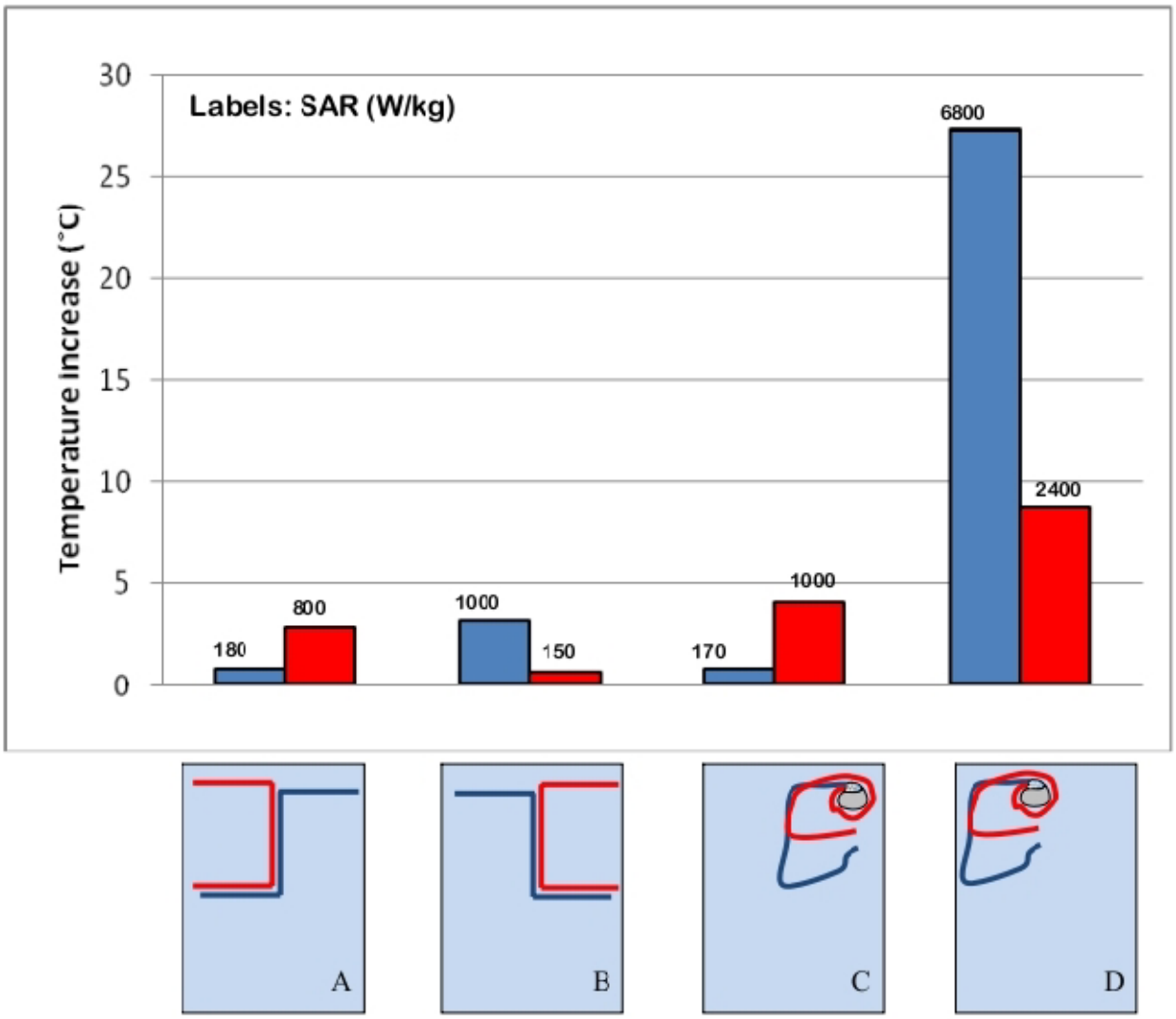

Figure 6. Shaped and area enclosed by the implant. Comparison between the temperature increases and SAR measured at the tip of metallic wires of different shape (A, B); comparison between the temperature increases and SAR for PM implants of different area, in different regions of the phantom. The uncertainty in the reported SAR value is ± 2 dB. Each group of bars refers to the implant configuration reported below.

Inside the human-shaped phantom we reproduced left and right pectoral implants of the pacemaker can, with the lead paths chosen to most closely approximate a physiological configuration for a dual chamber PM, simulating implantation in both atrium and ventricle. In agreement with the measurements on the rectangular box phantom, we found that right-pectoral implants produced a higher heating that left-pectoral implants, in most of the configurations we studied. We also investigated if the different structures of unipolar and bipolar PM leads may affect the amount of heating caused by MRI exposure.

We compared temperature increases with the each of two leads attached separately to the same PM can. The leads were located in various regions inside the rectangular phantom, in order to see if this would produce different degrees of heating at their tips.

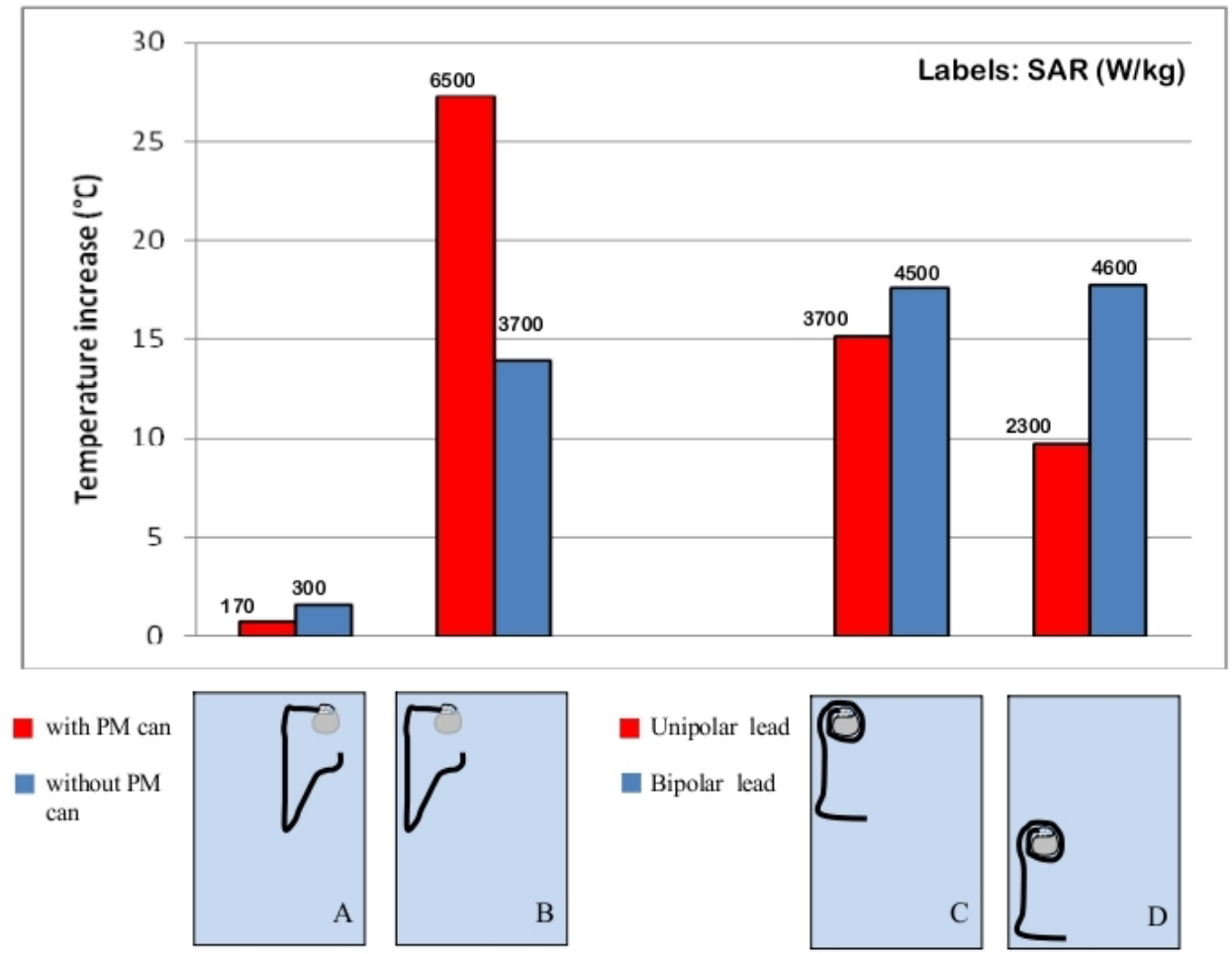

Figure 7. Implant and lead structure. Effect of the presence of the PM can on the temperature increase and SAR at the lead tip (A, B); different amounts of heating and SAR observed for unipolar and bipolar PM leads (C, D). The uncertainty in the reported SAR value is ± 2 dB. Each group of bars refers to the implant configuration reported below.

We found that for locations in the phantom where low temperature increases occurred, the behavior of the two types of leads is quite similar, whereas for locations in the phantom where heating was higher, the temperature increase for bipolar leads was significantly greater than for unipolar leads. A maximum difference of 8.1°C was observed, for one-loop PM configurations and with the leads placed close the edges of the phantom (Figure 7C–D).

In addition, we performed a group of measurements in order to evaluate how the presence of the PM can modifies the temperature increase at the lead tip. By comparing the results on PM leads that were either attached or unattached to a PM case, we observed a significant difference in the two situations. The presence of the PM can may either lead to an increase or decrease in the induced heating, depending on its position inside the phantom (Figure 7A–B). The same differences we found in the temperature increases, for the implant geometries and structures tested were as well found for the computed SAR values.

2.3.5. Position of the phantom and the implant with respect to the RF coil

Several implant configurations were tested with the phantom placed at first in the center of the coil and then moved along the main coil axis towards the RF excited (driven) ring (Figure 1a) or the non-excited ring end. We found that the amount of heating strongly depends on the phantom position, regardless the phantom shape (either rectangular or human-shaped): the highest temperature increase was measured when the implant was located inside the central field area of the RF coil (± 13 cm far from the center along X, Y and Z axes – isocenter): since both metallic wires and PM leads were generally placed in the upper middle half region of the phantoms, closer to excited ring, the maximum heating was obtained when moving the phantom towards the non excited ring. As the implant was shifted out from the central field region of the coil, the temperature increase was less than it when the implant was placed in the isocenter. At a distance of about 30 cm from the isocenter, we observed a 10–30% temperature rise decrease, with respect to the one measured inside the central field area, depending on the particular implant configuration.

We previously observed that an implant located next to any of the edges of the phantom produces the highest temperature increase. Our interest was also to understand if the contribution to the heating was due to the fact that the implant was positioned near the edges of the phantom or near the leg of the RF coil. To this aim, we compared temperature measurements performed on implants located in the same position respect to the coil, but in different areas of the phantom (i.e. the phantom was moved but the implant was in a fixed location in the coil). A marked decrease in the heating was always observed when implants were moved from the edges to the center of the phantom, even without changing their positions respect to the RF coil.

In addition, the presence of the tuning capacitors in the low-pass birdcage coil may cause a local increase in the E field. However, this high field regions are rather small, and may additionally contribute to the lead heating only when both the phantom and the implant are positioned very close to the inner side of the coil.

Also with regard to the SAR, the position of the phantom inside the RF coil showed to be an important factor. For a typical PM implant configuration (no-loop, left implant), the deposited power goes from 2217.5 W/kg with the phantom moved towards the excited ring, to 4432.9 W/kg with the phantom moved towards the non excited ring (see Additional file 2 for further details).

2.3.6. Geometry of the phantom

We measured induced heating for the same wire and lead configurations when implanted in the rectangular box and in the human-shaped phantom. Even though great care was taken in order to maintain the same distance between the implants and the borders of the phantom, we observed that, for almost all the implants we tested, the temperature increase measured inside the human-shaped phantom was about 6°C lower than in the rectangular trunk simulator (Figure 8). The lower temperature increases measured

inside the human shaped phantom go with lower SAR value, compared to same configurations reproduced inside the rectangular phantom.

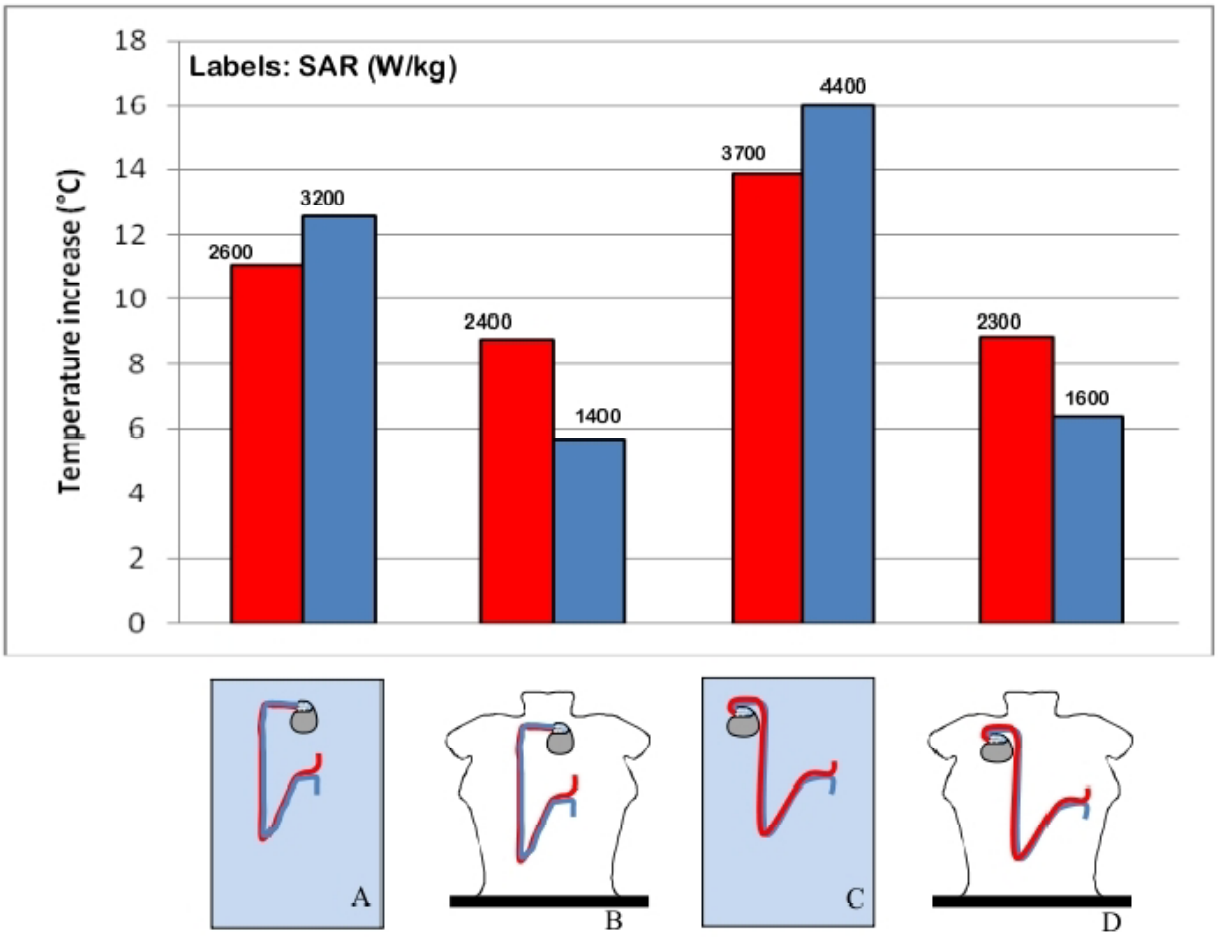

Figure 8. Geometry of the phantom. Effect of the phantom geometry on the induced heating and SAR for the same implant configuration reproduced inside the rectangular box phantom (A, C) and the human shaped phantom (B, D). The uncertainty in the reported SAR value is ± 2 dB. Each group of bars refers to the implant configuration reported below.

2.3.7. Thickness of the insulation sheath

We compared the temperature increases for three straight wires of the same length (15 cm) with no insulation (bare wire), 0.5 mm thick insulation (single-sheath) and 1 mm thick insulation (double-sheath wire) thermoplastic sheaths. Different locations inside the rectangular phantom were tested (close to the edge, halfway between the edge and the center and in the center – Figure 9); the phantom was kept in the central field region of the coil, at the same distance from the coil legs and rings. We found that the bare and the single-sheath wire produced almost the same temperature increase, even if the bare wire reaches the steady state more slowly than the insulated wire. The heating at the tip of the double-sheath wire was instead significantly lower: a temperature increase of 2.2°C was measured, compared to 5.2°C of the bare and single-sheath wires.

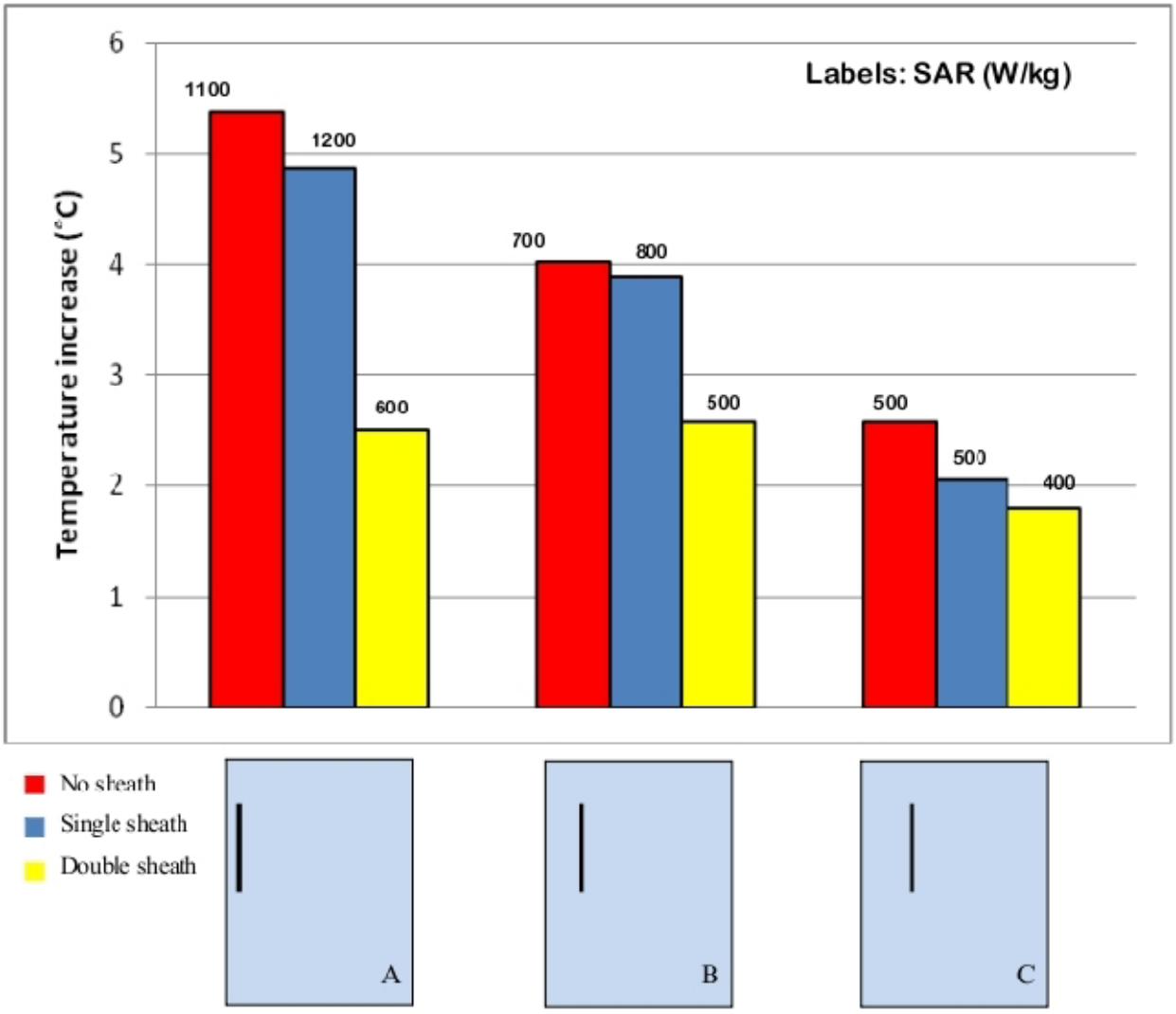

Figure 9. Thickness of the insulation sheath. Influence of the presence and thickness of the insulation sheath on the amount of the induced heating and SAR at the tip of a 15 cm long straight wire. The uncertainty in the reported SAR value is ± 2 dB. Each group of bars refers to the implant configuration reported below.

We also used a 25 cm-long bare wire to reproduce more realistic paths for a PM lead: several positions and geometries were tested and no significant heating was observed at the lead tip, even when the same configuration for an insulated wire (0.5 mm insulation thickness) had produced temperature increases greater than 10°C. The different dynamic in temperature rise leads to a SAR value that is higher for the insulated wire than for the bare one, even if the temperature increase is higher for the latter than the former.

2.4 Discussion

Previous studies investigating MRI induced PM lead heating reported a large variability in the induced temperature increases versus the location of the lead in phantom and the location of the phantom within the coil. We performed extensive measurements inside a RF birdcage coil on metallic wires and PM leads, in order to identify the major contributors to heating, which may explain such variability in results. We collected a wide archive of experimental data consisting of 374 configurations, which reveal how complex the problem is and how many factors have to be taken into account in order to understand and model the heating-induction phenomenon. These factors include the position of the implant inside the phantom, the structure and the geometry of the lead, the thickness of the external insulation on the lead the presence of the PM can, the shape and size of the phantom, and the position of the phantom inside the RF coil.

Our data show clearly that the several factors are the primary influence on heating at the tip. Closer locations of the leads to the edge of the phantom and to the edge of the coil produce maximum heating. This is due to the electric field that is highest at the edges (radial and at the ends) of the phantom nearest the inner wall of the RF coil; in addition, the low-pass structure of the coil may additionally contribute to the heating if the implant is close to the tuning capacitors placed along the legs. The other factor is the length of the lead. Others have stated that the magnetic field is believed to be a primary contributor to heating of the lead. Several papers in the literature [4,10] chose a configuration of the pacemaker lead in the coronal plane to achieve a maximal magnetic induction area (larger loop producing larger area (area as shown in Figure 2b). This was done by others to maximize the heating at the lead tip.

We found that the temperature increase is not always proportional to this area. Similar areas might give different temperature increases; in some cases we even observed a higher temperature increase on the tip of the implant with the smaller area, but with the lead located closer to the phantom's edges. We demonstrated that rather than the area, the length of the straight segments of the lead and their position inside the phantom and the coil determines the amount of heating.

The comparison between left and right implant configurations, both with metallic wires and PM leads, confirms that the area covered by the implant is not a crucial element in MRI induced heating. Right implants covered an area significantly smaller than the left counterparts and the temperature increases are higher for the former than the latter ones.

The influence of the insulation sheath on the MRI induced heating is still a widely discussed issue. The thickness of the silicone or polyurethane sheath of a PM lead (less than a millimeter) is very small compared to the wavelength (5 m) of the RF field used inside a MRI system. This would let us suppose that the presence of the insulation is not an important aspect to be considered in modeling the RF currents induced in the lead [20]. Actually, our experimental measurements prove that the amount of heating depends greatly on whether the metallic wire is provided with insulation or not. In addition, the thickness of the insulation seems to play an important role. For a bare wire that was shaped to reproduce the typical

path of a PM lead, the RF induced temperature increase was much lower than for the same configuration with an insulated wire of the same shape.

However, when comparing temperature increases on short straight wires (15 cm long) exposed under identical conditions, the higher heating is observed for the bare wire, compared to insulated wire of the same length and shape. For the bare, short wire the temperature reached after long exposures (steady state) is high, but the initial rate of rise (SAR at the wire tip) is lower. Furthermore, for short straight wires, the heating seems to decrease as the thickness of the insulation sheath increases.

The contribution of the lead structure (unipolar or bipolar) to the heating is strongly affected by the positioning of the lead itself inside the phantom: bipolar leads showed higher temperature increases than unipolar when placed close to the edge of the phantom; when placed in the central regions, heating was slightly higher for unipolar. Since this comparison was based on a limited number of positions and lead paths, no generalization or interpretation of these results can be attempted.

Clinical MRI birdcage coils are designed to have a homogenous RF magnetic field over the entire body of a patient. We did studies to mimic MRI imaging of a part of the body different from the thorax, such as the head or the abdomen, for a pacemaker patient. The phantom was shifted along the main (Z) axis of the RF coil. For these conditions, the highest heating is obtained with an implant that crosses the isocenter of the coil. As the distance of the center of the implant from the isocenter increases, the heating gets lower. Particularly, a marked decrease in temperature occurs when part of the implant is shifted along the Z axis of the coil out from the ring of the RF coil.

Temperature and SAR measurements we performed showed also the importance of the morphology of the phantom: the heating induced in the same implant configurations when placed in the rectangular phantom was higher than in the human-shaped phantom. The irregular surface of the human-shaped phantom implies a distance of the implant from the edges that varies point to point. This may partially explain such differences. Furthermore, the currents that are induced in the rectangular phantom, follow straight regular paths that provide a better coupling with straight metallic wires or leads. Our findings highlight the factors that have significant effects on RF-induced heating of implanted wires and leads. These factors must be taken into account by those who plan to study, model MRI heating of implants. Also our data should help those who wish to develop guidelines for defining safe medical implants for MRI patients. In addition, our database of the entire set of measurements can help those who wish to validate their numerical models of implants that may be exposed to MRI systems.

2.5 Conclusions

Our study demonstrates how complex the MRI-induced heating phenomenon of pacemaker leads is and how many aspects are involved in this process. Experimental measurements inside a RF birdcage coil at 64 MHz revealed two major factors affecting the amount of lead tip heating: the length of the straight

segments of the lead and their position inside the phantom. In particular, in order to have the worst case condition (i.e. maximize the induced heating and local SAR at the tip) inside a simulated torso, the following are necessary. The lead has to be placed parallel and next to the lateral edges of the phantom (parallel to the long axis of the phantom). The phantom has to be placed close to the inner wall of the RF coil, The length of the lead has to be close to the theoretical resonance length, at the frequency of the applied RF field (i.e. a half wavelength in the dielectric tissue medium). In addition the path of the lead has to be chosen as to obtain the best coupling with the E field distribution inside the phantom. With regards to the field generated by a birdcage RF coil typically used in most MRI scanners, the lead path which goes from the right pectoral region to the heart ventricle is the one that produces the best coupling with the E field. Other aspects play also an important role in MRI induced heating: the structure of the lead, the presence of the PM can, the geometry (shape) of the phantom and its position inside the coil. All these elements make it very time-consuming and expensive to perform extensive and exhaustive experimental measurements, as well as to develop accurate numerical models. Thus, while our presented data cannot be exhaustive, to our knowledge, they represent the largest database of MRI induced heating on thin metallic implants and pacemaker leads. The data are also intended to be used to validate numerical models.

Disclaimer

The mention of commercial products, their sources, or their use in connection with material reported herein is not to be construed as either an actual or implied endorsement of such products by the U.S. Food and Drug Administration. The opinions expressed by of the author are not those of the US Food and Drug administration.

Competing interests

The author(s) declare that they have no competing interests.

Authors' contributions

EM carried out the experimental measures and drafted the manuscript. MT realized the human shaped-phantom and participated in the acquisition of the experimental data. GC has made substantial contributions to conception and interpretation of data. FC participated in the design of the experimental set-up, interpretation of data and revised the manuscript. WK participated in the design and realization of the exposure system and discussed the methodological issues related. GM helped in the preparation of the gel and in setting up and calibrating the temperature acquisition system. HB revised the final manuscript and gave the final approval for publication. PB gave the final approval for publication.

Additional file 1

Temperature and SAR measures on metallic wires. The Excel file (2007 version) contains the temperature raw data collected during the RF exposure of metallic wires. For each configuration, which corresponds to a single column of the file, a schematic representation of the experimental setup is reported. For each configuration, we also calculated the difference between the baseline and the highest temperature reached during the RF exposure (dT – °C), as well as the SAR (W/kg), from the slope of the initial temperature increase (see Methods section for details). The file is divided into 5 sheets, which refers to different shapes of the metallic wire: - straight wires; - left imp. wires (insulated wires shape to simulated the PM lead path from the left pectoral region to the heart ventricle); - right imp. wires (insulated wires shape to simulated the PM lead path from the right pectoral region to the heart ventricle); - bare wires; - left and right imp. wires (left imp. wires and right imp. wires simultaneously exposed to the RF signal). The first column of each sheet contains the time reference for the temperature values.

Click here for file [http://www.biomedcentral.com/content/supplementary/1475- 925X-7-11-S1.zip]

Additional file 2

Temperature and SAR measures on PM leads. The Excel file (2007 version) contains the temperature raw data collected during the RF exposure of PM leads. For each configuration, which corresponds to a single column of the file, a schematic representation of the experimental set-up is reported. For each configuration, we also calculated the difference between the baseline and the highest temperature reached during the RF exposure (dT - °C), as well as the SAR (W/kg), from the slope of the initial temperature increase (see Methods section for details). The file is divided into 5 sheets, which refers to different locations or structures of the lead: - left imp.-0,1,2 loops (PM can positioned in the upper left region of the phantom, with the lead that makes 0, 1 or 2 loops around it); - right imp.-0,1,2 loops (PM can positioned in the upper right region of the phantom, with the lead that makes 0, 1 or 2 loops around it); - Bipolar leads; - rect. VS human-shaped phantom (comparison between same configuration in the rectangular and in the human-shaped phantom). The first column of each sheet contains the time reference for the temperature values.

Click here for file [http://www.biomedcentral.com/content/supplementary/1475- 925X-7-11-S2.zip]

References

[1] Kalin R, Stanton MS: Current clinical issues for MRI scanning of pacemaker and defibrillator patients. *Pacing Clin Electrophysiol* 2005, **28**(4):326-8

[2] Nair P, Roguin A: Magnetic Resonance Imaging in patients with ICDs and Pacemakers. *Indian Pacing Electrophysiol J* **5**(3):197-209. 2005 Jul 1

[3] Helfer JL, Gray RW, MacDonald SG, Bibens TW: Can pacemakers, neurostimulators, leads, or guide wires be MRI safe? Technological concerns and possible resolutions. *Minim Invasive Ther Allied Technol* 2006, **15**(2):114-20

[4] Sommer T, Vahlhaus C, Lauck G, von Smekal A, Reinke M, Hofer U, Block W, Traber F, Schneider C, Gieseke J, Jung W, Schild H: MR imaging and cardiac pacemakers: in-vitro evaluation and in-vivo studies in 51 patients at 0.5 T. *Radiology* 2000, **215**(3):869-79

[5] Achenbach S, Moshage W, Diem B, Bieberle T, Schibgilla V, Bachmann K: Effects of magnetic resonance imaging on cardiac pacemakers and electrodes. *Am Heart J* 1997, **134**(3):467-73

[6] Roguin A, Zviman MM, Meininger GR, Rodrigues ER, Dickfeld TM, Bluemke DA, Lardo A, Berger RD, Calkins H, Halperin HR: Modern pacemaker and implantable cardioverter/defibrillator systems can be magnetic resonance imaging safe: in vitro and in vivo assessment of safety and function at 1.5 T. *Circulation* 2004, **110**(5):475-82. 2004 Aug 3

[7] Martin ET, Coman JA, Shellock FG, Pulling CC, Fair R, Jenkins K: Magnetic resonance imaging and cardiac pacemaker safety at 1.5-Tesla. *J Am Col Cardiol* **43**(7):1315-24. 2004 Apr 7

[8] Konings MK, Bartels LW, Smits HF, Bakker CJ: Heating around intravascular guidewires by resonating RF waves. *J Magn Reson Imaging* 2000, **12**(1):79-85

[9] Bassen H, Kainz W, Mendoza G, Kellom T: MRI-induced heating of selected thin wire metallic implants – laboratory and computational studies – findings and new questions raised. *Minim Invasive Ther Allied Technol* 2006, **15**(2):76-84

[10] Rezai AR, Baker KB, Tkach JA, Phillips M, Hrdlicka G, Sharan AD, Nyenhuis J, Ruggieri P, Shellock FG, Henderson J: Is magnetic resonance imaging safe for patients with neurostimulation systems used for deep brain stimulation? *Neurosurgery* 2005, **57**(5):1056-62

[11] Kanal E: White Paper on MRI Safety. In American Society of Neuroradiology Toronto, Canada. May 24, 2005

[12] ASTM F2182-02a: "Standard Test Method for Measurement of Radio Frequency Induced Heating Near Passive Implants During Magnetic Resonance Imaging". In ASTM International 100 Barr Harbor Drive, PO Box C700, West Conshohocken, PA, 19428-2959 USA

[13] Duru F, Luechinger R, Scheidegger MB, Luscher TF, Boesiger P, Candinas R: Pacing in magnetic resonance imaging environment: clinical and technical considerations on compatibility. *Eur Heart J* 2001, **22**(2):113-24

[14] Nitz WR, Oppelt A, Renz W, Manke C, Lenhart M, Link J: On the Heating of linear conductive structure as Guide Wires and Catheters in Interbentional MRI. *Journal of Magnetic Resonance Imaging* 2001, **13**:105-114

[15] Yeung CJ, Susil RC, Atalar E: RF heating due to conductive wires during MRI depends on the phase distribution of the transmit field. *Magn Reson Med* 2002, **48**(6):1096-8

[16] Luechinger R, Duru F, Zeijlemaker VA, Scheidegger MB, Boesiger P, Candinas R: Pacemaker reed switch behavior in 0.5, 1.5, and 3.0 Tesla magnetic resonance imaging units: are reed switches always closed in strong magnetic fields? *Pacing Clin Electrophysiol* 2002, **25**:1419-1423

[17] Mattei E, Triventi M, Calcagnini G, Censi F, Kainz W, Bassen HI, Bartolini P: Temperature and SAR measurement errors in the evaluation of metallic linear structures heating during MRI using fluoroptic probes. *Phys Med Biol* **52**(6):1633-46. 2007 Mar 21

[18] C95.3-2003: Recommended Practice for Measurements and Computations with Respect to Human Exposure to RadioFrequency Electromagnetic Fields, 100 kHz to 300 GHz. *Institute of Electrical and Electronics Engineers* (EEEI)

[19] Ruggera PS, Witters DM, von Maltzahn G, and Bassen HI: In vitro assessment of tissue heating near metallic medical implants by exposure to pulsed radio frequency diathermy. *Phys Med Biol* 2003, **48**:2919-28

[20] Stuchly MA: Numerical Evaluation of Radio Frequency Power Deposition in Human Models during MRI. *Proceedings of the 28th IEEE EMBS Annual International Conference*, New York City, USA . Aug 30–Sept 3, 2006

Chapter 3

In vitro investigation of pacemaker lead heating induced by magnetic resonance imaging: role of implant geometry

G Calcagnini[1], M Triventi1, F Censi[1], E Mattei[1], P Bartolini[1], W Kainz[2] and H I Bassen[2]

[1] Department of Technologies and Health, Italian National Institute of Health, Roma, Italy

[2] Center for Devices and Radiological Health, Food and Drug Administration, Rockville, MD, USA

Published on Journal Of Magnetic Resonance Imaging 28:879–886 (2008)

Abstract

Purpose*: To evaluate the effect of the geometry of implantable pacemakers (PMs) on lead heating induced by magnetic resonance imaging (MRI).*

Materials and Methods*: In vitro experiments were conducted with two different setups, using fluoroptic probes to measure the temperature increase. The first experiment consisted of a rectangular box filled with a gelled saline and a pacemaker with its leads. This box was exposed in an MRI birdcage coil to a sinusoidal 64-MHz field with a calibrated whole-body specific absorption rate (WB-SAR) of 1 W/kg. The highest SAR and temperature increase (3000 W/kg, 12°C) occurred for the implant configuration having the largest area. The second experimental setup consisted of a human-shaped torso filled with gelled saline. In this setup the PM and its lead were exposed to a real MRI scanner, using clinical sequences with WB-SAR up to 2 W/kg.*

Results*: We found that higher heating occurs for configurations with longer exposed lead lengths and that right chest PMs showed the highest temperature and local SAR (11.9°C, 2345 W/kg), whereas the left chest PMs were less heated (6.3°C, 1362 W/kg). Implant geometry, exposed lead length, and lead area must be considered in the wide variation of temperature increases induced by MRI.*

Conclusions*: The amount of MRI-induced lead tip heating depends strongly on implant geometry, particularly the lead area, exposed lead length, and position of the implant in the phantom. Critical lead tip heating was found for the longer leads. Therefore, to minimize MRI-induced lead tip heating, the PM lead should be as short as possible.*

Key Words*:* pacemaker; lead heating; fluoroptic measurements; implant geometry; radiofrequency

3.1 Introduction

Magnetic resonance imaging (MRI) is now contraindicated for patients implanted with pacemakers (PMs) and implantable cardioverter-defibrillators (ICDs) (1– 6). The potential effects of MRI on PMs, ICDs, and other active implantable medical devices (AIMDs) include: force and torque effects (7,8); an undefined reedswitch state within the static magnetic field (9); the potential risk of heart stimulation and inappropriate pacing (10,11); and heating effects at the lead tip (12– 14).

The radio-frequency (RF) field used in MRI procedures may induce high current density around the lead tip (14–16). The amount of heating has been investigated by several groups who observed temperature increases from non-significant values up to tens of degrees. For example, Achenbach et al (12) reported a temperature increase of 63.1°C for a pacemaker lead; Rezai et al (17) measured 25.3°C at the end of a deep brain stimulation electrode; Roguin et al (16) reported a maximum increase of 5.7°C at 3.54-W/kg average whole-body specific absorption rate (WB-SAR), as shown on MRI. Sommers et al (13), with a WB-SAR of 1.3 W/kg, obtained temperature increases ranging from 0.1° to 23.5°C, depending on the electrode type. Several factors influence the degree of heating:

1. The WB-SAR, which has been shown to correlate with temperature increase (18).
2. The cooling effect of the blood around the leads, which is seldom quantified.
3. The length and geometric structure of the lead.
4. The implant location, which may change the current induced.

Among these variables, we focused our attention on those characterizing real implants in clinical practice. In this study we investigate the effect of the lead geometry and the lead and pacemaker can placement of an implantable pacemaker on lead heating induced by MRI.

3.2 Materials and methods

We performed tests in vitro using two saline gel phantoms. The first test consisted of a rectangular box inside an MRI birdcage coil, and the second used a human shaped phantom inside a real MRI system.

The first setup was used for heating measurements, using a dual-chamber pacemaker (Elect D; *Sorin Biomedica* CRM, Italy) and a biventricular three-chamber pacemaker (New Living CHF; *Sorin Biomedica*) and two different leads, one unipolar and the other bipolar (Models S80T and S80TB; *Sorin Biomedica*).

Based on the results obtained, we conducted a second series of experiments with a human-shaped phantom at an MRI clinical facility, using a dual-chamber pacemaker connected to a bipolar lead.

The lead had a length of 62 cm for all experiments, with an active tip area of 6 mm2 and an active ring area of 36 mm2. Both the rectangular box and the human shaped phantom were filled with a gel composed of the following materials (in percent, by weight): 2% hydroxyethylcellulose (HEC; commercial name *Natrosol*); 97.64% water; and 0.36% sodium chloride. The gel has conductivity of 0.59 Sm1 at 64 MHz and heat capacity of 4178.3 J/kg K1 (19,20). These values have been chosen to most closely approximate those of human tissues at the frequencies of interest (i.e., 64 MHz), as specified by ASTM Standard F2182-02a (20).

A fluoroptic thermometer (*Luxtron* Model 3100; SMM Probes) was used to measure the temperature rise while minimizing perturbations to the RF fields (20). This thermometer has a resolution of 0.1°C and performs up to 8 measurements per second. A similar setup was used by Bassen et al (21) for an investigation of MR Iinduced heating of metallic implants.

3.2.1. Rectangular Box Simulator

The rectangular box simulator consists of a rectangular box (60 30 20 cm) filled with saline gel. A 30 20-cm plastic grid submerged in the gel supports the implant and maintains consistent separation distances between the implant, phantom surface, and temperature probes. The grid can be adjusted so that the top of the implant can be positioned below the gel surface. The pacemaker and the leads were arranged in the gel 5 cm below the phantom's gel surface simulating the implanted lead in the human body. The phantom was placed in the middle of the MRI birdcage coil (i.e., with the center of mass of the box coinciding with the coil isocenter), housed in an anechoic chamber. The birdcage structure consists of 16 65-cm-long rods closed

by two 62-cm-diameter external rings; the RF coil type is low-pass, with a tuning capacitor placed along each rod and a metallic shield. A 64-MHz quadrature sinusoidal excitation to the coil was delivered by a 100-W RF amplifier. The output power was measured continuously by a directional coupler and power meter. Using this setting, the RF energy delivered to the box corresponds to a WB-SAR of 1.0 W/kg (Fig. 1).

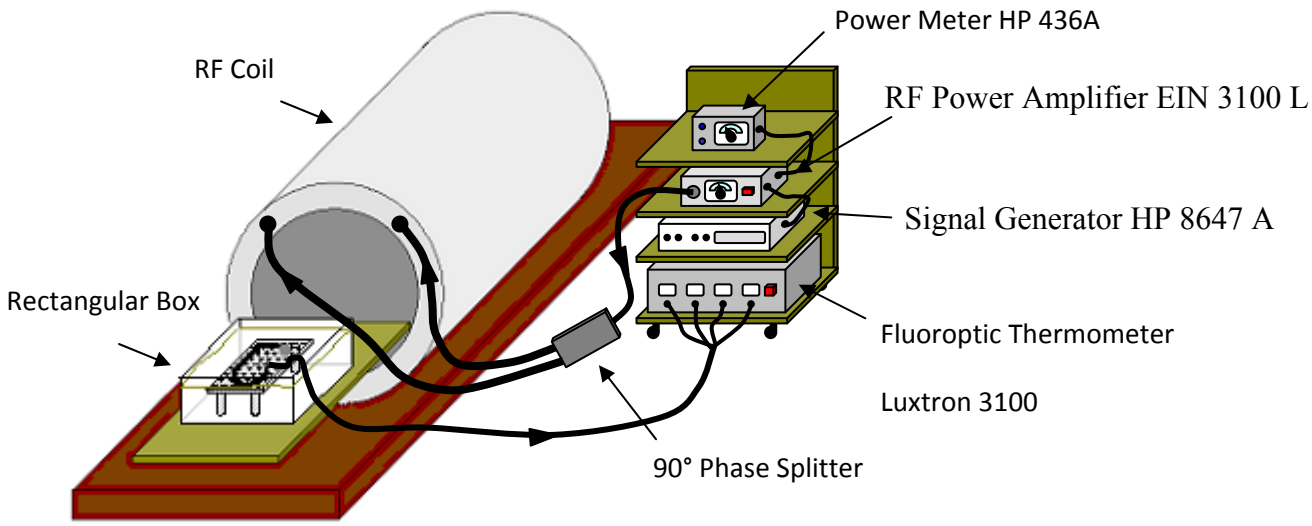

Figure 1. Schematic representation of the rectangular box simulator and the MRI simulator. The instruments used to feed the RF coil and measure the heating are also shown.

This value was obtained using a calorimetric method: the box, filled with 0.36% saline, was surrounded by a 2-cm-thick layer of foam rubber to ensure adiabatic conditions. Exposure to the RF signal lasted 1 hour and produced an average temperature increase of 0.9°C. Under these conditions, the WB-SAR can be determined according to the following SAR definition:

$$WB\ SAR = \frac{\Delta Temp}{\Delta time} \cdot C_p \qquad (1)$$

where WB-SAR is specific absorption rate (W/kg), Cp is the specific heat of a lossy medium (joules/kg/°C), and $\frac{\Delta Temp}{\Delta time}$ is the rate of temperature rise (°C/sec).

3.2.2. Human-Shaped Phantom

Experiments in a real MRI scanning system were performed using a human-shaped torso simulator (Fig. 2). The simulator is a transparent polyvinyl chloride (PVC) torso of a 70-kg male (Fig. 2A), with a 32-L internal volume (20). Inside the torso, a PVC grid supports the pacemaker, its leads, and the temperature probes (Fig.

2B). The torso was filled with the same saline gel as used in the simulated MRI experiments. Implant Geometry Configuration The actual geometry of a pacemaker implant may vary between patient2. The pacemaker can be implanted in the left or in the right side of the chest. Up to three leads may be advanced into the veins to reach the right atrium, the right ventricle, and the coronary vein. Because the length of the lead may not fit the patient's anatomy and size, the excess length is usually wrapped near or around the PM can.

Figure 2. The torso simulator filled with gel (A) and equipped with a plastic grid, which supports the PM implant and the fluoroptic probes (B). The phantom prepared for a real MRI scan is shown in (C).

In the experiments with the rectangular box, the total lead area of the implant was varied by wrapping the excess lead near the PM can or by changing the lead path. An example of varying the lead geometry is shown in Figure 3: When the lead forms loops around the PM the magnetic induction area is reduced (Fig. 3, upper panel); the lead area also changes by varying the lead path (Fig. 3, lower panel). For each configuration we computed the total lead area of the implant and the exposed lead length. The total lead area was calculated as the area delimited by the lead, the PM can, and the line connecting the lead tip to the PM center of mass (Fig. 3, shaded areas); the exposed length was defined as the lead length not wrapped around the PM can. In the experiments using the rectangular box simulator the PM was always positioned as a left-side implant. In the human-shaped phantom, both right- and left-side implants were tested (Fig. 4).

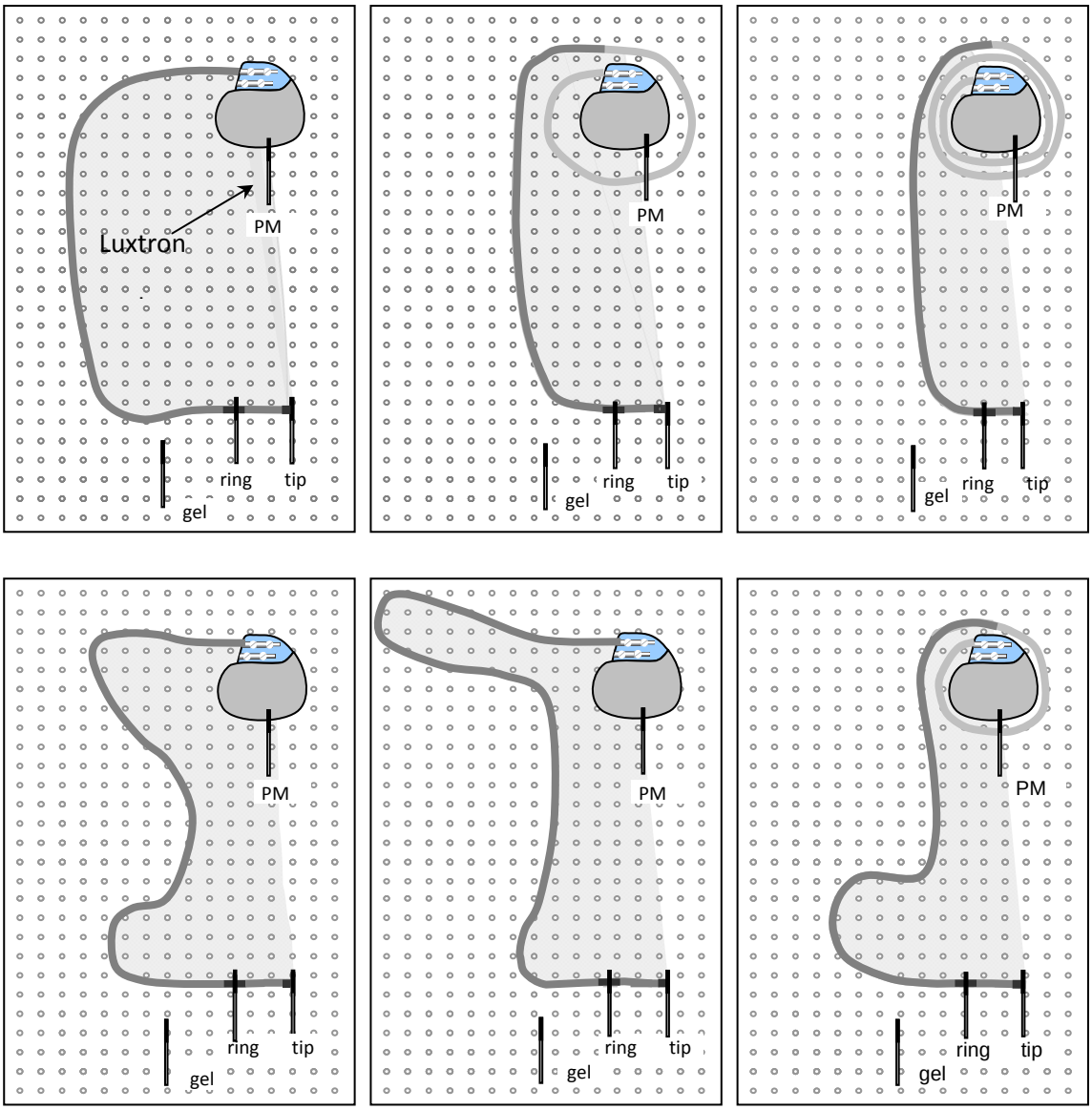

Figure 3. Examples of implant configurations tested in the MRI simulator. Lead area has been changed both by wrapping the lead around the PM (top panel: no-loop, 1-loop, and 2-loops) and/or by changing the lead path (bottom panel). The lead area of the implant (shaded) and the effective lead length (dark gray) are depicted. The positions of the optical probes are also shown (gel, ring electrode, lead tip, and PM case).

3.2.3. Temperature Measurements and SAR Calculation

According to Bassen et al (21), local SAR is a reliable indicator of the maximum heating capability of an implant in vitro. In a previous study, Mattei et al (22) investigated the positions and mounting of the temperature probes, which gives the minimum error for temperature and SAR measurements. The best positioning is obtained when the Luxtron probe tip (at the center of the pigmented part) is in direct contact with the lead tip or the ring electrode. In this configuration, the Luxtron probe tip and the lead tip or ring electrode are perpendicular to each other. Care was taken to ensure contact of the sensitive region of the Luxtron probe (center of the pigmented end of the Luxtron probe) and the lead tip or ring electrode. This

configuration is also mechanically stable and reproducible. Another probe was used to monitor the temperature increase of the PM can. Last, a fourth probe measured the gel temperature 6.5 cm away from the lead tip. Configurations using two or three leads were investigated in a similar way using a second Luxtron thermometer. Before each experiment the probes were calibrated, immersed in the gel, and finally thermally equilibrated. All measurements started at the same baseline temperature.

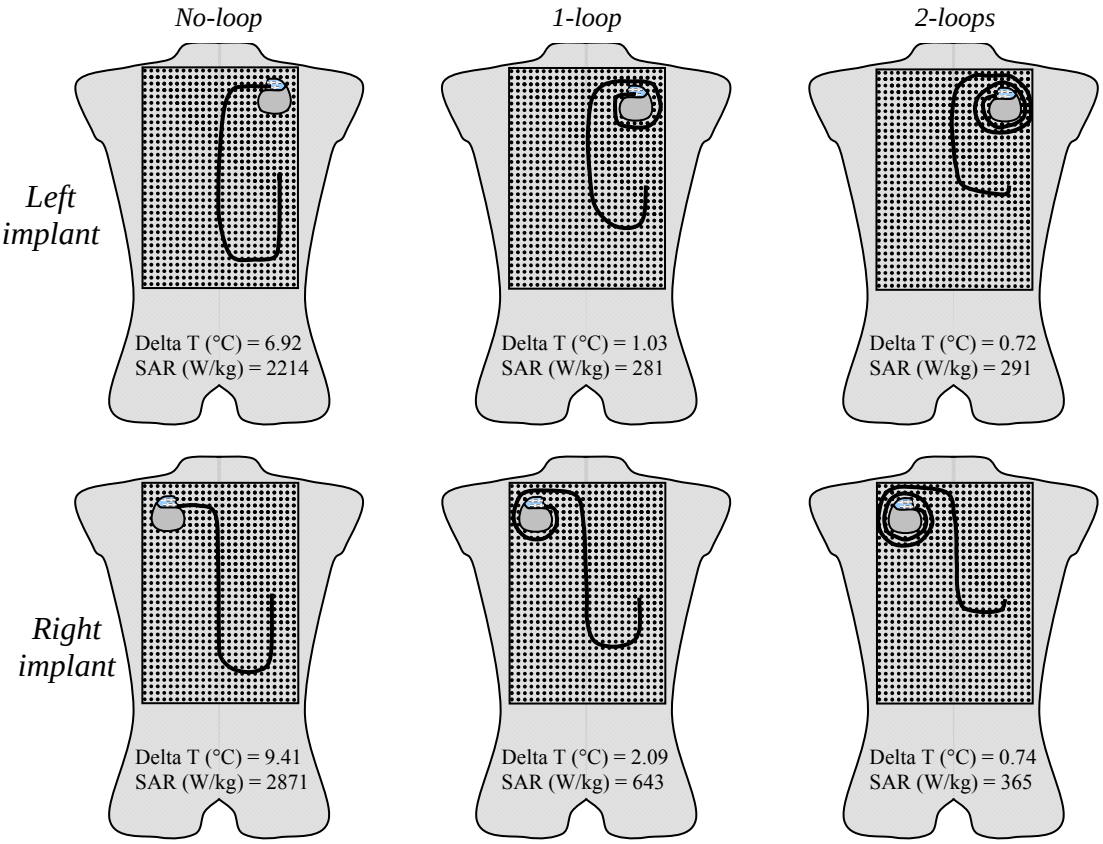

Figure 4. The six implant configurations tested in a real MRI using the human-shaped phantom: no-loop, 1-loop, and 2-loops for both left and right chest implantation. Local SAR and heating at the lead tip during a short fast spin-echo sequence, with WB-SAR of 1.94 W/kg (right implant) and 1.96 W/kg (left implant), are also shown.

3.2.4. Experimental Protocols

- *Rectangular Box Simulator in MRI Simulator* Forty-two lead geometries were tested. The position of the PM and the lead tip was kept unchanged throughout the experiments. Different lead areas were obtained by changing the lead geometry, as explained previously. Each experiment consisted of a measurement of the baseline temperature for about 1 minute, followed by 2 minutes of RF exposure. Higher absolute temperatures would occur with prolonged exposure times.

- *Human-Shaped Phantom in Real MRI System* Experiments were performed on a 1.5-T scanner (Magnetom Sonata Maestro; Siemens) (Fig. 2C). The main parameters of the sequences used are summarized in Table 1. MRI parameters (TR, TE, and flip angle) were adjusted not to exceed a WB-SAR of 2 W/kg as estimated by the scanner. The torso was placed in the MRI coil and its position was adjusted to have the MRI isocenter at the lowest part of the sternum (xiphoid process), a common position in clinical practice. The lead geometry included left and right PM placements. For each implant, three lead paths were tested (Fig. 4): without a lead loop around the PM (no-loop configuration) and with the lead forming one or two loops around the PM can (one-loop and two-loop configurations, respectively). For each lead path, the length and the position of the linear section of the lead as well as the position of the lead tip were kept constant. Only the PM was moved either to the left or to the right, without changing the sense of the winding of the loops, if any. For all experiments the total lead length was 62 cm. The PM was interrogated before and after each scan sequence to detect any possible changes in the programmed parameters.

Table 1. Main Parameters of MRI Clinical Sequences Used during Human-Shaped Phantom Experiments in a Real MRI Scanner

Siemens sequence name	Sequence type	TR (ms)	TE (ms)	Flip Angle	Length (s)
FLASH (short)	Spoiled gradient echo	960	40	20	53
FLASH (long)	Spoiled gradient echo	960	40	20	417
TrueFISP (short)	Steady state free process	3.78	1.89	54	38
TrueFISP (long)	Steady state free process	3.78	1.89	54	379
HASTE (short)	Single shot (turbo fast) spin echo	1190	83	150	42
HASTE (long)	Single shot (turbo fast) spin echo	1190	83	150	402

3.3 Results

Figure 5 shows an example of temperature increase during exposure to a real MRI sequence in the human shaped phantom and to a continuous sinusoidal RF field in the rectangular box simulator. The highest rise occurred within the first minute; a lower but stable increase was observed after 100 seconds, then an almost

steady state was reached, with temperature continuing to increase, yet very slowly. After each test the PM was interrogated. No changes in any programmed parameters were observed in either the RF coil or the real MRI scanner.

3.3.1. Rectangular Box Simulator

The greatest temperature increase was always observed at the lead tip. No significant increase in temperature (< 1°C) was observed at the PM can or in the gel far from the lead. No differences were observed between the two PM models. The ring electrode of the bipolar leads showed a much smaller temperature increase than the lead tip in all measurements. We observed no differences in the temperature of the lead tips whether unipolar or bipolar, or when PM programming was changed from unipolar to bipolar sensing/pacing. When the PM was connected to multiple leads simultaneously (right atrium, right and left ventricles), we did not observe a significant change in the amount of heating of each lead tip with respect to the single lead configuration.

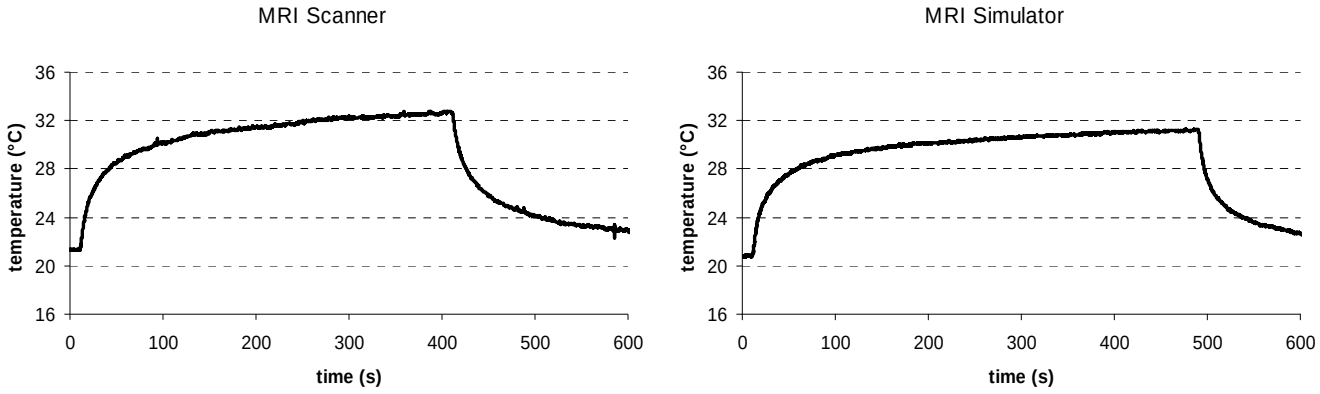

Figure 5. Example of a temperature increase during exposure to MRI RF. (Left) Temperature increase of lead tip from exposure to a clinical MRI sequence. (Right) Temperature increase during exposure to continuous sinusoidal RF from the MRI simulator.

Figure 6 (top image) shows the temperature increase at the lead tip for various lead areas; the bottom image shows the local SAR values at the lead tip, for the same experiments, plotted as a function of the lead area. As the lead area increased, we observed an increase in final temperature and the local SAR. Figure 7 shows the temperature increase at the lead tip as a function of the exposed lead length. Note that geometries with short exposed lengths always indicated negligible temperature increases, whereas, as the exposed length increased, the heating increased with lead tip heating up to 12°C. The increase of temperature and local SAR at the lead tip seems to be related to the lead area and the exposed lead length (Fig. 6).

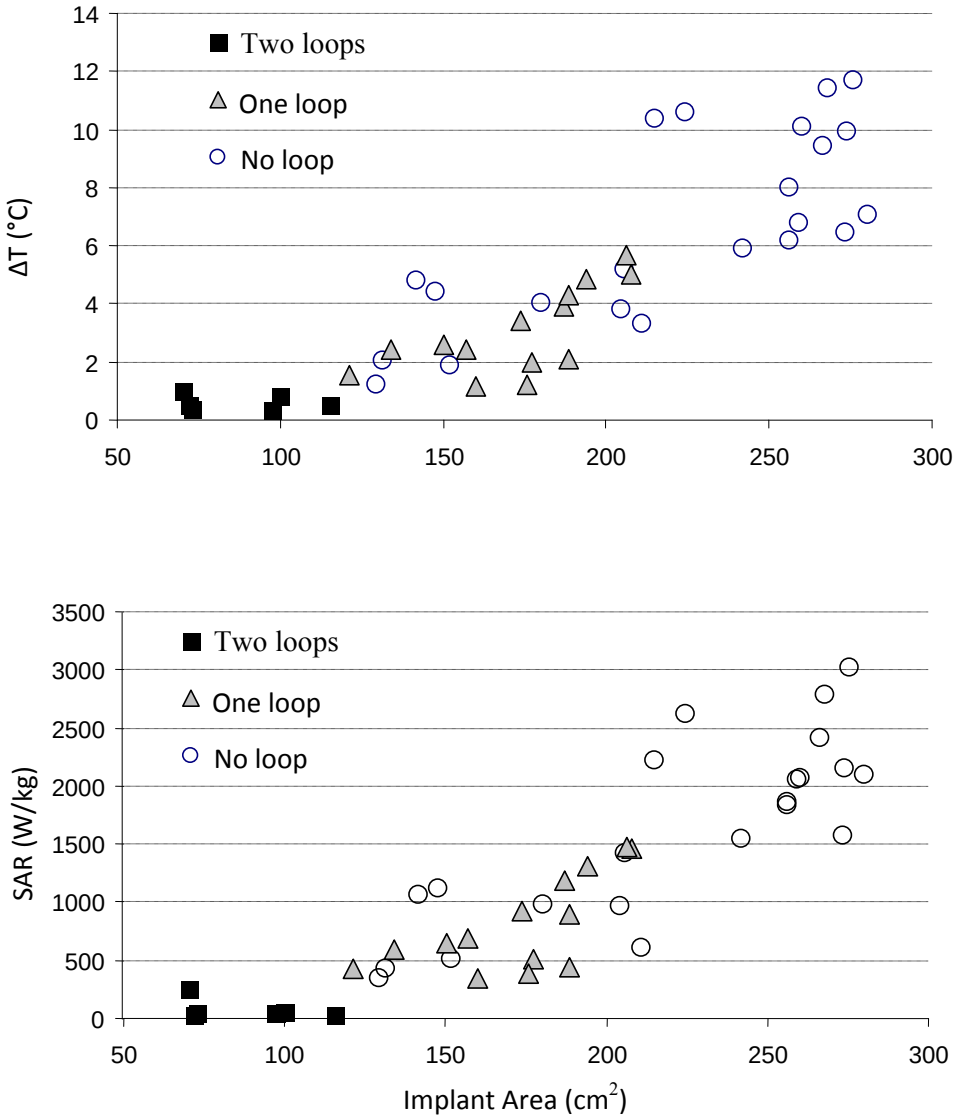

Figure 6. Plot of temperature increase (top) and local SAR at the lead tip (bottom) as a function of the lead area, from experiments performed using the rectangular box simulator. Different lead areas were obtained either by wrapping the lead around the PM can or by changing the lead path. Local SAR was estimated using the slope of the temperature increase (see text).

The lead around the PM can or the number of loops did not seem to play a significant role. The no-loop and one-loop configurations, with the same lead areas, produced a similar temperature increase and local SAR. However, the no-loop configuration showed, with increasing lead area, increased heating and local SAR values. Two experiments showed a temperature increase and local SAR values significantly higher than what could be expected from their relatively large lead area. A retrospective analysis of these configurations showed that the lead had a relatively long, straight path (approximately 20 cm). Based on our experiments we cannot conclude whether a straight lead is always more heated than other lead paths. All of the aforementioned measures were done with the center of the box positioned in the isocenter of the RF coil.

3.3.2. Human-Shaped Phantom

The temperature increase and local SAR values for the experiments using a real MRI scanner are reported in Table 2. As for the clinical sequences, the gradient-echo (FLASH) induced no detectable temperature increase (below the Luxtron probe sensitivity, 0.1°C) in all configurations tested. Sequences with a relatively high WBSAR, led to temperature increases of up to 12.3°C. When the PM was implanted in the left chest area, the lead area involved in the lead path appeared to be the major factor relevant for the lead heating. The no-loop configuration (large lead area) always showed a greater temperature increase than one- and two-loop configurations. Surprisingly, when the PM was implanted in the right chest area, the lead length seemed to play a major role; that is, the no-loop configuration again always showed temperature increases significantly greater than the one- and two-loop configurations. In addition, the temperature increases were always greater than those for the left implants. In both left and right implants the temperature increase and local SAR were proportional to the WB-SAR reported by the scanner.

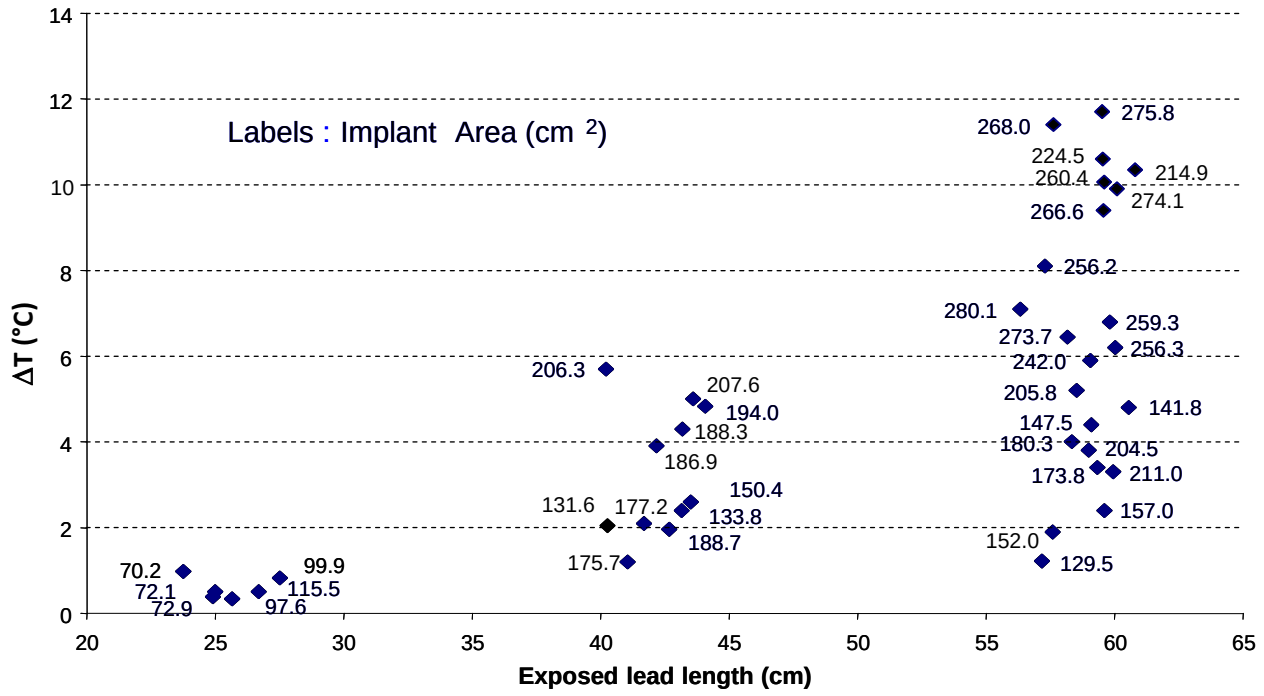

Figure 7. Plot of the temperature increase at the lead tip as a function of the exposed lead length, from the same experiments as in Figure 6. Exposed lead length was defined as the length of lead not wrapped around the PM can. The three clusters of data correspond to the no-loop, one-loop, and twoloops lead configurations, respectively.

The comparison between short and long sequences showed that, as observed during continuous sinusoidal RF exposure in the rectangular box simulator, the largest temperature increase occurred within the first minute. Figure 4 summarizes the local SAR and heating at the lead tip during a short fast spin-echo sequence for the six geometries tested.

All experiments were repeated with changing MRI parameters, such as the center of view (chest, abdomen, and pelvis) and the field of view (200, 300, and 400 mm), but also with various PM settings (unipolar vs. bipolar sensing and pacing, pacemaker on and off), without significant changes in the heating.

Table 2. Temperature Increase (°C) and Lead Tip Local SAR (W/kg) of Human-Shaped Phantom Experiments*

	Left pectoral implant			**Scanner**	**Right pectoral implant**			**Scanner**
Geometry	*No loop*	*1-loop*	*2-loops*	**Reported SAR* (W/kg)**	*No loop*	*1-loop*	*2-loops*	**Reported SAR* (W/kg)**
Exposed length (cm)	61.1	36.8	18.9		61.1	36.8	18.9	
FLASH (short)	0.1 (---)	<0.1 (---)	<0.1 (---)	0.02	<0.1 (---)	<0.1 (---)	<0.1 (---)	0.02
FLASH (long)	0.1 (---)	<0.1 (---)	<0.1 (---)	0.02	<0.1 (---)	<0.1 (---)	<0.1 (---)	0.02
TrueFISP (short)	4.2 (1055)	0.6 (---)	0.4 (---)	1.72	8.2 (2192)	1.9 (---)	0.6 (---)	1.70
TrueFISP (long)	6.2 (1255)	1.0 (---)	0.6 (---)	1.70	12.3 (2375)	2.5 (536)	1.0 (---)	1.70
HASTE (short)	6.9 (2214)	1.0 (281)	0.7 (291)	1.96	9.4 (2871)	2.1 (643)	0.7 (365)	1.94
HASTE (long)	6.3 (1362)	0.9 (---)	0.7 (---)	1.70	11.9 (2345)	2.7 (641)	1.0 (---)	1.72

***SAR: WB-SAR calculated by the MRI scanner;**
(---) SAR not estimable, due to low temperature increase.

3.4 Discussion

The major objective of this study was to determine the effect of implant geometry on the lead tip heating. Previous studies investigating MRI-induced PM lead heating reported a large variability in the induced heating. All investigations showed that the maximum RF-induced heating occurred at the lead tip. However, temperature increases at the lead tip have been reported to vary between 0.1°C (14) and 63.1°C (13).

Such variability depends on a number of factors, such as the type and positioning of the temperature probes next to the lead tip, the WB-SAR used, the cooling effect of the blood flow, the lead structure, the lead

length, the geometry of the PM implant, the location of the implant in the RF coil, and the position inside the body.

Previous studies stated that the lead area, which is the area formed by the lead, the PM can, and the straight line connecting the lead tip to the PM can, plays a significant role in lead tip heating (13,19). Most of our experiments were performed to quantify the contribution of the implant area to the heating, as an independent parameter. Our data clearly show a temperature increase proportional to the lead area, although, in some cases, similar lead areas gave different temperature increases. Thus, the implant area may not be the only factor determining the temperature increase.

We also found that wrapping the excess lead near the PM can does not contribute to lead tip heating; that is, given comparable implant areas, the presence of loops did not systematically affect the temperature increase produced at the lead tip. We also investigated the contribution of exposed lead length to the amount of heating (Fig. 7).

We found a negligible temperature increase in all the geometries with short exposed lead length (about 20 cm), but for longer exposed leads the temperature increase ranged from 1° to 12°C. These results suggest that the lead couples with the electric field and that large areas will also lead to RF-induced currents, because they generally imply a longer exposed lead segment. Thus, more so than area, the crucial factor that affects the amount of heating at the implant tip is the length of the exposed lead. This has also been confirmed by the high heating observed in linear lead configurations, which have been investigated in several studies (12,14,15). We found that unipolar and bipolar leads, but also different PM settings (unipolar vs. bipolar sensing and pacing), produced similar lead heating. The lead heating obtained for a left-sided PM inside the human shaped phantom exposed in a real MRI system was consistent with findings obtained with the rectangular box exposed in the MRI birdcage coil. The exposed lead length and the lead areas are contributing factors to lead heating. When PMs are implanted in the right side of the chest the resulting lead areas are smaller than for the left-side PMs. However, we observed a greater temperature increase, suggesting that the lead also couples to the electrical field. A resonance phenomenon in various kinds of linear structures (eg, catheters used in interventional radiology) has been hypothesized (4,15). A pacemaker lead is a conducting object embedded in an isolator, which is placed in a conducting media, thus the calculation of a resonant length has to take into account factors such as the conductivity and dielectric constant of the medium, as well as the structure of the lead (eg, number and disposition of internal conductors, insulation sheets, and the terminations at both ends). Nitz et al estimated that, at 64 MHz, the critical length ($\lambda/2$) of a conductive straight wire immersed in blood is 28.8 cm (15). This value is close to the length of the linear section of the lead in our torso simulator experiments. The induced current on the different segments of the lead may either add to, or subtract from, one another, depending on the phase of the electrical field. Such behavior may explain the differences between left and right implants. The amount of heating at the lead tip is the result of the coupling between the local electrical field at the segments of the lead. Such coupling may result in addition- or subtraction-induced currents, depending on the phase of the local electric field.

Using a WB-SAR of approximately 1 W/kg we observed, in the worst case, a temperature rise of up to 12°C and a local SAR of up to 2300 W/kg. The in vitro test methods used herein were not intended to simulate the dynamics of blood and body fluids, but rather to simulate the nearly instantaneous energy deposition. Thus, for patients, the temperature rise may be reduced by blood flow.

In bipolar leads we also measured the temperature increase at the ring electrode and found very limited heating (<2°C). Similar results were found by other groups (19). The larger surface area of the ring electrode reduces the current density and therefore the temperature increase is much lower compared with the lead tip.

In our investigation of whether other PM settings could change the lead heating we found that lead heating is insensitive to PM programming (eg, unipolar/ bipolar sensing and pacing) and that there were no significant differences between bipolar and unipolar leads. The simultaneous use of two or three leads did not change the heating systematically.

Baker et al (18) demonstrated that the WB-SAR calculated by different MRI systems is not a reliable metric for RF-induced heating. In addition, the methods used by the various manufacturers in calculating SAR values are not only different but in some cases proprietary, and thus it becomes rather difficult to compare results obtained with different scanners, even with the same value of WB-SAR.

We found similar differences when we compared, for a given WB-SAR, the heating obtained in the calibrated simulator with a real MRI system.

Using the simulator with a calorimetrically measured WB-SAR of 1.0 W/kg we detected a temperature increase of about 12°C for a given lead configuration. In a real MRI system the same configuration showed an increase of about 6°C for a WB-SAR (as reported by the MRI system) of 1.70 W/kg. An overestimation of the WB-SAR by the real MRI system may explain the disparity. In this case, the real MRI system overestimated the WB-SAR by a factor of 3.4. Such a WB-SAR overestimation may lead to the same factor for underestimation of implant heating because most testing of implant heating relates the temperature increase to the WB-SAR given by the MRI system (MWB- SAR). This may be due to the use of different assumptions and algorithms by the MRI systems and also to the fact that M-WB-SAR estimation might not be valid for phantoms. Further research and a comparison and re-evaluation of WB-SAR estimation and the SAR distribution of real MRI systems for humans and phantoms are urgently needed to resolve this problem.

In conclusion, our data show that the amount of MRI-induced lead tip heating strongly depends on the implant geometry, consisting of the lead area, the exposed lead length, and the position of the implant in the phantom. Critical lead tip heating was found for the longer leads. Therefore, to minimize MRI-induced lead tip heating the PM lead should be as short as possible. Implants with a relatively large lead area (i.e., 250 to 300 cm2), exposed to a WB-SAR of about 1 W/kg, may heat at the lead tip up to 12°C with a local SAR of up to 3000 W/kg. Significant heating may also occur for smaller lead areas, depending on the degree of coupling with the electric field. An estimation of lead heating, however, is very complicated because it involves several factors aside from implant geometry, such as lead structure, lead dimension, and relative position within the MRI coil. In conclusion, implant geometry has to be accounted for as an important factor

with regard to the wide variations in temperature increase reported in the literature. Future MRI-compatible pacemaker systems should aim to minimize the lead length.

Study Limitation

Our study investigated only the heating of MRI on pacing leads in vitro. Other potential risks of MRI in pacemaker recipients, such as fast pacing, inhibition of stimulation, or direct stimulation of the heart caused by the RF or gradient fields, require further investigation.

Disclaimer

The opinions and conclusions stated in this study are those of the authors and do not represent the official position of the Department of Health and Human Services. The mention of commercial products, their sources, or their use in connection with the materials reported herein is not to be construed as either an actual or implied endorsement of such products by the Department of Health and Human Services.

Acknowledgments

The authors thank G. Gaggini (Sorin Biomedica Cardio) for providing the PMs and their leads; Monica Brocco for language revision of the manuscript; Giorgio De Angelis for preparation of the human-shaped phantom; Professor Paolo Pavone for suggestions on the MRI clinical sequences; Aniello Cipolletta for the assistance during MRI scanning; and Rosanna Pinto and Giorgio Lovisolo (Italian National Agency for New Technologies, Energy and the Environment) for the measurement of the electrical conductivity of the gel.

References

[1] Fetter J, Aram G, Holmes DR Jr, et al. The effects of nuclear magnetic resonance imagers on external and implantable pulse generators. *Pacing Clin Electrophysiol* 1984;**7**(4):720-7

[2] Kanal E, Borgstede JP, Barkovich AJ, et al. American College of Radiology white paper on MR-safety. *AJR Am J Roentgenol* 2002;**178**:1335–1347

[3] Gimbel JR, Johnson D, Levine PA, et al. Safe performance of magnetic resonance imaging on five patients with permanent cardiac pacemakers. Pacing Clin Electrophysiol 1996;**19**(6):913-9

[4] Duru F, Luechinger R, Scheidegger MB, et al. Pacing in magnetic resonance imaging environment: clinical and technical considerations on compatibility. Eur Heart J 2001; **22**(2):113-24

[5] Zaremba L. FDA guidance for MR system safety and patient exposures: current status and future considerations. In: Shellock FG, editor. Magnetic resonance procedures: health effects and safety. Boca Raton, *FL: CRC Press* 2001;183–196

[6] Shellock FG. Cardiac pacemakers and implantable cardioverter defibrillators. In: Reference manual for magnetic resonance safety, implants and devices. *Biomedical research publishing group* 2007;163-176

[7] Luechinger R, Duru F, Scheidegger MB, et al. Force and torque effects of a 1.5-Tesla MRI scanner on cardiac pacemakers and ICDs. *Pacing Clin Electrophysiol* 2001;**24**:199–205

[8] Shellock FG, Tkach JA, Ruggieri PM, et al. Cardiac pacemakers, ICDs, and loop recorder: evaluation of translational attraction using conventional ("long-bore") and "short-bore" 1.5- and 3.0-Tesla MR systems. *J Cardiovasc Magn Reson* 2003;**5**(2):387-97

[9] Luechinger R, Duru F, Zeijlemaker VA, et al. Pacemaker reed switch behavior in 0.5, 1.5, and 3.0 Tesla magnetic resonance imaging units: are reed switches always closed in strong magnetic fields? *Pacing Clin Electrophysiol* 2002;**25**:1419–23

[10] Erlebacher JA, Cahill PT, Pannizzo F, et al. Effect of magnetic resonance imaging on DDD pacemakers. *Am J Cardiol* 1986;**57**:437–40

[11] Hayes DL, Holmes DR Jr, Gray JE. Effect of 1.5 tesla nuclear magnetic resonance imaging scanner on implanted permanent pacemakers. *J Am Coll Cardiol* 1987;**10**:782–86

[12] Achenbach S, Moshage W, Diem B, et al. Effects of magnetic resonance imaging on cardiac pacemakers and electrodes. *Am Heart J*. 1997;**134** 467–473

[13] Sommer T, Vahlhaus C, Lauck G, et al. MR imaging and cardiac pacemakers: in-vitro evaluation and in-vivo studies in 51 patients at 0.5 T. *Radiology* 2000;**215** 869–879

[14] Luechinger R, Zeijlemaker VA, Pedersen EM, et al. In vivo heating of pacemaker leads during magnetic resonance imaging. *Eur Heart J* 2005;**26**(4):376-83

[15] Nitz, WR, Oppelt, A, Renz, W, et al. On the Heating of linear conductive structure as Guide Wires and Catheters in Interventional MRI. *Journal of Magnetic Resonance Imaging* 2001;**13**:105-114

[16] Roguin A, Zviman MM, Meininger GR, et al. Modern Pacemaker and Implantable Cardioverter/Defibrillator Systems Can Be Magnetic Resonance Imaging Safe. In Vitro and In Vivo Assessment of Safety and Function at 1.5 T. *Circulation* 2004;**110**:475-482

[17] Rezai AR, Finelli D, Nyenhuis JA, et al. Neurostimulation systems for deep brain stimulation: in vitro evaluation of magnetic resonance imaging-related heating at 1.5 tesla. *J Magn Reson Imaging* 2002;**15**(3):241-50

[18] Baker KB, Tkach JA, Nyenhuis JA, et al. Evaluation of Specific Absorption Rate as a Dosimeter of MRI-Related Implant Heating. *Journal of Magnetic Resonance Imaging* 2004;**20**:315–320

[19] Ruggera PS, Witters DM, von Maltzahn G, et al. In vitro assessment of tissue heating near metallic medical implants by exposure to pulsed radio frequency diathermy. *Phys Med Biol* 2003;**48**:2919–2928

[20] American Society for Testing and Material (ASTM) Designation: F2182-02a. Standard Test Method for Measurement of Radio Frequency Induced Heating Near Passive Implants During Magnetic Resonance Imaging, 2004

[21] Bassen H, Kainz W, Mendoza G, et al. MRI-induced heating of selected thin wire metallic implants -- laboratory and computational studies -- findings and new questions raised. *Minim Invasive Ther Allied Technol* 2006;**15**(2):76-84

[22] Mattei E, Triventi M, Calcagnini G, et al. Temperature and SAR measurement errors in the evaluation of metallic linear structures heating during MRI using fluoroptic® probes. *Phys Med Biol* 2007;21;**52**(6):1633-46

[23] C95.3-2002: Recommended Practice for Measurements and Computations with Respect to Human Exposure to RadioFrequency Electromagnetic Fields, 100 kHz to 300 GHz, *Institute of Electrical and Electronics Engineers* (IEEE) 2002

Chapter 4

Numerical FDTD models of the birdcage RF coil of a MRI scanner: comparison between different solutions

E Mattei[1]**, M Triventi1, G Calcagnini**[1]**, F Censi**[1]**, and P Bartolini**[1]

[1] Department of Technologies and Health, Italian National Institute of Health, Roma, Italy

Published on Proceedings of the Sixth IASTED International Conference, Biomedical Engineering, Innsbruck, Austria 2008, ISBN Hardcopy: 978-0-88986-721-5/CD 978-0-88986-722-2

Abstract

Numerical models represent a very useful approach to investigate the effects of MRI on implanted medical devices. The finite-difference time-domain (FDTD) method was used to model the radiofrequency (RF) field generated by a birdcage resonator. We developed four numerical models which differ in terms of RF excitations and computational complexity, but which all produce a circular-polarized magnetic field at 64 MHz: a realistic 16-leg birdcage tuned by capacitors; a 16-leg birdcage with leg currents fixed to a specified value; a 2-plane waves excitation model and a 4-plane waves excitation model. Our interest was to evaluate the computational efficiency of the models, and to compare the resulting field pattern, as well as the induced specific absorption rate (SAR). It is shown that the assumption of fixed current inside the coil's leg does not significantly affect the results only when the study involved homogeneous domain, but not in the case of implanted objects. Moreover, by using a superposition of four plane waves, it is possible to obtain a field distribution surprisingly similar to the one of a fully modelled birdcage, drastically reducing the computation effort required by the simulation.

4.1 Introduction

Magnetic resonance imaging (MRI) has become an established diagnostic modality. The clinical usefulness of in-vivo magnetic resonance spectroscopy (MRS) was demonstrated in several instances and is being explored further. These techniques involve exposure of the patient to static and time-varying magnetic fields and radiofrequency (RF) electromagnetic (EM) fields. In particular, the RF energy deposition may induce elevation of temperature to levels at which local thermal injury or systemic thermal overload may occur. Such a potential health hazard becomes more dangerous when the patients is implanted with metallic objects, as pacemakers (PM), implantable cardioverter defibrillators (ICD), brain stimulators, cochlear implants and so on. The scientific and medical literature have deeply investigated this issue: Sommer et al. - 2000 demonstrated the potential for heating as much as 23.5°C at specific absorption rate (SAR) levels of only 1.3 W/kg in a 0.5 Tesla MRI unit. Achenbach et al. - 1997 reported pacing lead tip temperature elevation in leads not attached to an implanted pulse generator (IPG) of >63°C during 90 seconds of MRI. Konings et al. – 2000 reported heating around intravascular guide wires by resonating RF waves of 26°C to 74°C after 30 seconds. Bassen et al – 2006 measured a temperature rise of about 0.5°C (local SAR=320 W kg^{-1}) for a stent exposed to the RF field of a 1.5 T MRI birdcage coil at 64 MHz; using the same experimental set-up, a temperature increase of 8.6 °C was observed at the bare end of an insulated 24-cm long wire (local SAR=5680 W kg^{-1}). Rezai et al. – 2005 reported deep brain stimulator temperature elevations at the electrode tip of >25°C within 15 minutes of MR imaging. This data is particularly disturbing when one realizes that thermal ablation procedures are typically performed at temperatures of approximately 50–60°C. At the same time, over 300 patients to date have been scanned without any significant clinical difficulty or complication (*Kanal 2005*).

Such widely varying results indicate how complex the problem is and that several factors influence the degree of heating: the whole body specific absorption rate, the patient position in the coil, the type of imaging sequence, the patient characteristics, the duration of imaging procedure, the body structure being imaged, the type and position of transmit coil, the lead design, the lead orientation within the patient, the degree of perfusion near the device, the temperature measurement procedure, the respiratory phase, etc. Many of these parameters are currently either not recognized or inadequately addressed by existing testing methods (*Helfer et al. 2006*).

Beside these wide experimental data available in literature, only a few studies have been published for computer simulations that have been used to calculate MRI induced heating of thin-wire medical implants (*Ho 2001, Bassen et al. 2006*). Simplified, low resolution simulations are not useful for small metallic structures and thin wires exposed to the RF field of MRI coils. For an ideal computation, the entire RF coil (with the actual power supply and the tuning capacitors able to produce a typical circularly polarized magnetic field) and the thin metallic wire must be simulated using high resolution. However, in order to decrease the computational effort requested by the model, in most of the numerical studies (*Ho et al 2001, Trakic et al 2004, Liu et al 2005*) the birdcage is modelled without the capacitors, forcing an appropriate current distribution inside the coil.

The challenge is to combine a simulation of large dimensions (i.e. MRI RF coil length > 1 m) and small structures (i.e. the thin wire << 1 mm).

In this paper we numerically computed the EM field resulting from four FDTD models: aim of the study is to evaluate the differences between the three models, in terms of type of source adopted, computational power required and resulting filed pattern. No experimental measures were performed: the numerical simulations are intended to find which simplifications can be made to an entire RF coil model, so to decrease the computational effort, without modifying the EM field distribution and the thermal effects on a metallic implant placed inside the coil.

4.2 Materials and methods

A MRI scanner generates a circular-polarized RF field (B_1 field) on the plane perpendicular to the direction of the main static field (B_0 field). Inside a birdcage coil typically used for MRI total body investigations, B_0 has the direction of the long axis of the coil: thus, B_1 rotates on the plane perpendicular to the main axis of the RF resonator. For an MRI scanner that works with a static field of 1.5 T (typical value for clinical applications), the frequency of the B_1 RF field is 64 MHz.

We developed four numerical models which differ in terms of RF excitations and computational complexity, but which all produce a circular-polarized magnetic field. We used commercial FDTD (Finite Difference Time Domain) software (SEMCAD X, version 11.0, SPEAG, Zurich) that incorporated native drawing and importing of 3-D CAD object models in ACIS (.sat) format. The software had a variable grid

(graded-mesh) generator and was used on a personal computer with a 2.4 GHz, 32-bit processor, 2 GB of RAM, and a Windows XP operating system. An accelerator card (*aXware V1.5 Card*) was used to speed up the solution time required by the numerical models.

Four models were developed using the FDTD software:

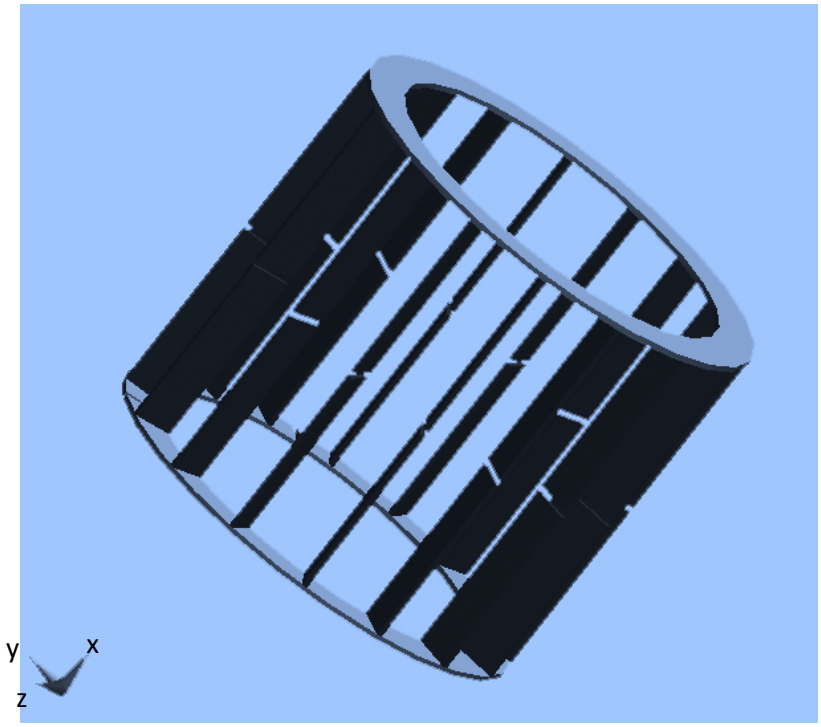

Figure 1. FDTD model of the MRI birdcage RF coil.

4.2.1. Model A – Birdcage with capacitors

We started our numerical study reproducing a realistic geometry of a 16-leg birdcage coil (figure 1): we chose rectangular legs (7x2 cm) so that they can be align with the FDTD grid. The birdcage is 65 cm high and has an internal diameter of 62 cm. In the middle of each leg we placed a 1 cm wide air gap and a capacitor was inserted to link the two sides of the metallic branches. The whole birdcage was model as a perfect electric conductor (PEC).

We performed a preliminary study to identify the correct capacitors value for the RF coil resonance. A broadband analysis allowed to set the capacitors so that the birdcage had its main resonance mode at 64 MHz, that is the RF typically used in clinical MRI scanners. In this first model, also the RF source was represented to most closely approximate the actual feeding line of a birdcage coil: two 64 MHz sinusoidal excitations were placed on one of the external rings of the coil, with 90° shift both in time and in space.

Both the geometry and the power supply used for the birdcage model reproduce realistically the structure of a physical model of an MRI coil adopted in previous studies (*Bassen et al. 2006*) to perform experimental measures on the induced heating of implanted thin metallic objects.

Besides the several calculations needed to adjust the capacitors to the resonance value, the computational effort required by this model is very high too: the dimensions and the geometry of the coil oblige to keep a quite fine mesh all over the domain. In particular, the capacitors need a discretization on at least two voxels (grid step < 0.5 cm).

4.2.2. Model B – Birdcage with current generators

A first simplification of the model can be obtained with the removal of all the lumped elements: in the centre of the birdcage legs, the capacitors are replaced by current generators, with sinusoidal time behaviour (64MHz) and a phase delay equal to the azimuthal angle, so to obtain circular polarization. This corresponds to an increasing 22.5° phase shift between the generators at each birdcage legs. This current is able to simulate the quadrature excitation adopted in the previous numerical model: in this case the resonance mode is no more achieved by tuning the capacitors, but forcing the right current distribution inside the birdcage legs. The absence of the capacitors implies that the broadband analysis that in the model A was required to characterize the frequency-dependent behaviour of the coil is now no more necessary.

An edge source like current generators does not need a mesh as fine as a lumped element; moreover, the two voltage sources on the coil ring are no more necessary, and thus the number of voxels required to generate the FTDT grid can be significantly reduced. However, the computational effort needed by the model is still high, due to the presence of the whole birdcage coil.

Such a model is the solution typically adopted to compute the electromagnetic field distribution generated by an MRI coil in a numerical analysis.

4.2.3. Model C – Two plane waves excitation

The electromagnetic field within a MRI coil is complex and the ratio of magnitudes of the E and B fields depends on the location within the coil. In the centre of the coil B dominates whereas close to the end of the RF coils the E field is dominant. The use of simple RF sources to simulate the behaviour of a birdcage coil undoubtedly implies some approximations in the resulting EM field distribution, but allows to save computational resources which could be spent to increase the mesh quality in other domains of the model (e.g. human anatomy structures, implanted electromedical devices, etc.)

To simulate the complex fields within an MRI coil we used a superposition of plane waves, which propagate at 64 MHz and create a rotating *B* field inside the central area of the model. This can be easily achieved by using two plane waves which propagate on orthogonal directions, with a time delay of 90°.

4.2.4. Model D – Four plane waves excitation

In order to create a more uniform E field distribution in the central area of the model, a second combination of plane waves was also adopted: we used two couples of plane waves; in each couple, the

plane waves propagate on parallel but opposite directions, with concordant B vector component and opposite E vector component. Between the two couples, a 90° shift both in space and in time was applied.
Our interest was to evaluate the electromagnetic field distribution generated by the different numerical models above described, inside a domain with physical properties similar to those of biological tissues. A dielectric 40x20x10 cm^3 box (phantom) was thus placed in the centre of each model, in a symmetric position respect to the RF source (birdcage coil or plane waves' propagation domain). The dielectric properties of the box were chosen as specified in the ASTM standard for RF measurements (F2182-02a): density = 1007.5 kg m^{-3}; specific heat capacity = 4178.6 J kg^{-1} K^{-1}; relative permittivity = 79; electrical conductivity = 0.6 Sm^{-1}. We used the same graded-mesh (min. step = 5 mm, max. step = 10 mm, max. grading ratio = 1.3) for the dielectric box in all the models we studied, so to ensure a consistent and uniform analysis of the EM field pattern. Also the magnitude of the RF sources used in the four models was set so to produce an equal mean SAR of 1W kg^{-1}, averaged over 1 g mass, inside the phantom.
In a second group of numerical simulations we compared the SAR value reached at the tip of a thin metallic wire (radius = 1 mm) placed inside the dielectric box in the four models developed. Two configurations of the wire were reproduced: a 26 cm-long straight wire and a loop with a radius of 10 cm. Both the lengths were chosen to match the theoretical resonance length at the frequency of interest (i.e. 64 MHz).
The metallic implants were positioned next to the edges of the dielectric domain, 2 cm inside the box, so to simulate a peripheral implant in the human trunk.

Table 1. Computational complexity of the FDTD numerical models.

Model type	Box not implanted with any object	Box implanted with a straight wire	Box implanted with a loop wire
Birdcage with capacitors	2.44488Mcells	11.3771Mcells	10.9561Mcells
Birdcage with current generators	1.76684Mcells	7.98244Mcells	8.68534Mcells
Two plane waves excitation	0.217152Mcells	1.38915Mcells	1.67409Mcells
Four plane waves excitation	0.217152Mcells	1.38915Mcells	1.67409Mcells

In table I, we reported the number of voxels required to generate the FDTD grid for the numerical models we developed: the number of voxels is proportional to the solution time, so a finer mesh implies a longer time for the simulation to be completed. The use of the accelerator card allowed to speed up the simulation of about a factor 10. The data in the table show how the presence of a thin structure implies a marked increase in the number of voxels used to generate the FDTD grid, in all the models we developed.

Since a low resolution discretization cannot be adopted for small metallic structures and thin wires exposed to the RF field of MRI coils, we indeed define a very fine mesh in the area covered by the implant (min. step = 0.25 mm, max. step = 0.5 mm, max. grading ratio = 1.3).

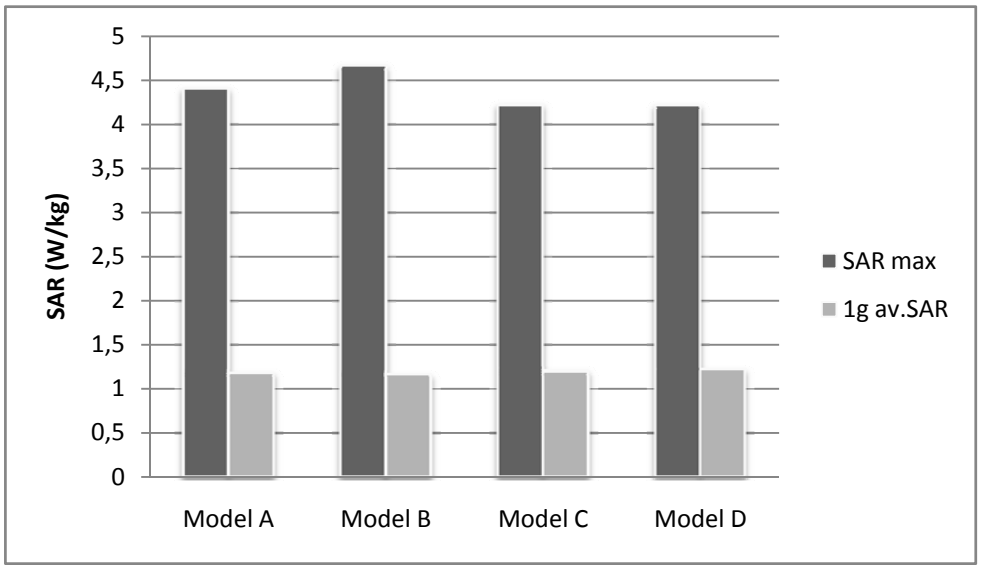

Figure 2. Maximum SAR (averaged over a single voxel: 5 mm3) and mean SAR (averaged over 1g mass) for the four numerical models.

In each of the four FTDT models, the circular-polarized magnetic field was generated both with a clockwise and anticlockwise orientation, in order to investigate how the inversion of the rotating *B* vector would affect the field distribution and the amount of heating induced inside the dielectric domain and at the tip of the metallic implants.

4.3 Results

In a preliminary group of numerical simulations, the RF excitations (voltage gaps on the ring coil – model A; current generators at the centre of each leg – model B; intensity of the plane waves – model C and D) was adjusted in order to produce the same value of mean SAR inside the dielectric domain of all the models developed. In figure 2 we reported the mean SAR averaged over 1 g mass and the maximum SAR calculate inside a single voxel (5x5x5 mm^3) for the four numerical models.

The SAR distribution inside the dielectric box was then mapped on a plane through the centre of the coil and on a plane 2cm below the phantom surface (implants location). As reported in figure 3, a symmetric distribution of SAR is obtained only in the first case (with the exception of the 2 plane waves model), whereas far from the centre of the coil, a higher value of SAR is reached at one side of the phantom.

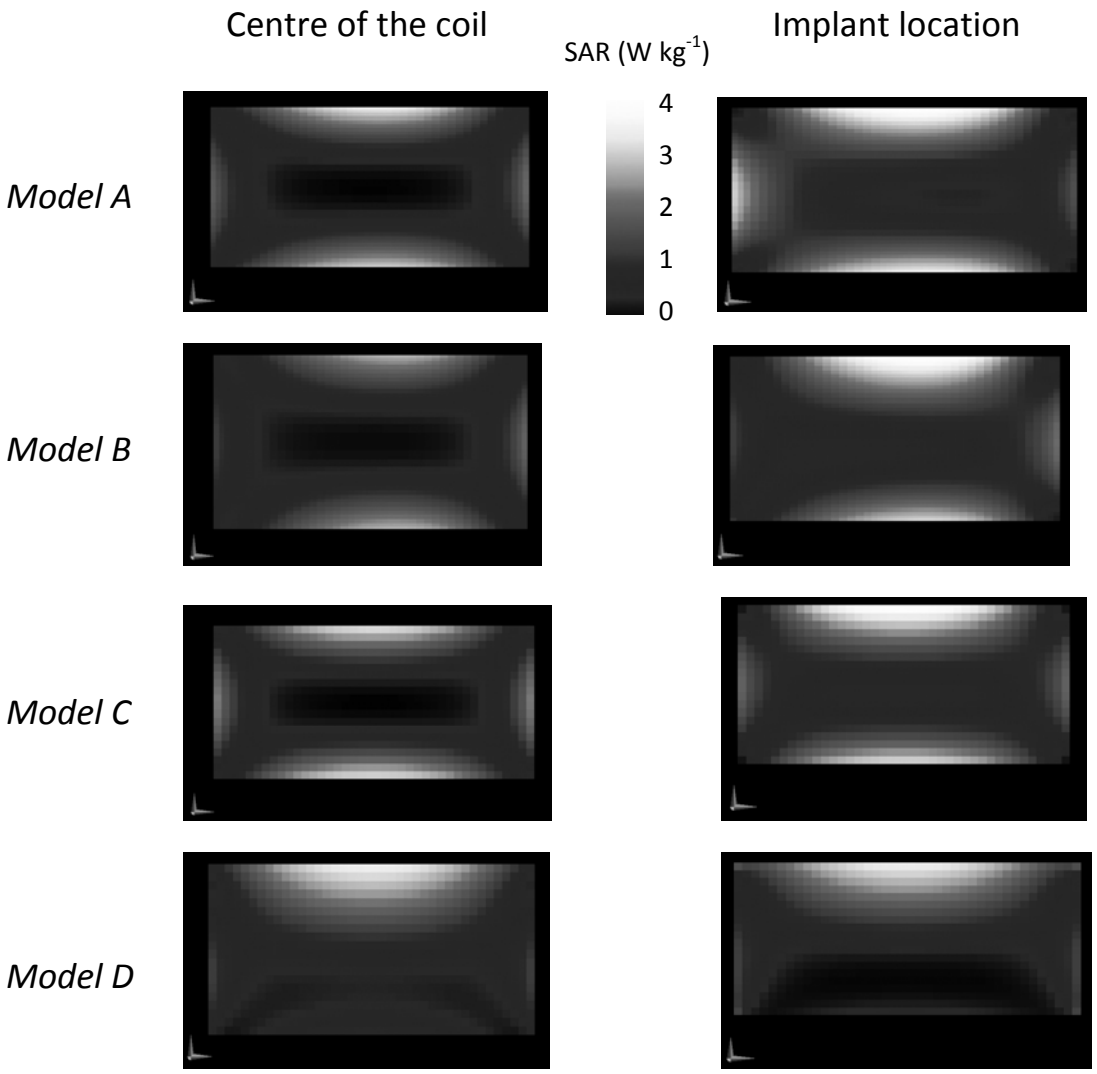

Figure 3. SAR maps on a transversal plane through the phantom: at the center of the coil (left panels) and at the implant location (right panels).

When the RF excitation in the four models is modified in order to invert the rotating *B* vector, we observed no changes on the plane through the centre of the coil, whereas at the implant location the SAR distribution is just the opposite of the one reported in figure 3.

The graphs in figure 4 show the value of the *B* and *E* field inside the coil at the implant location, along a line parallel to the longitudinal axes (x dir. – a, c) and to the transversal axes (z. dir. – b, d) of the coil. A magnification of the same graphs is reported in figure 5, where the electromagnetic field was calculated only inside the dielectric domain.

The metallic implant placed inside the phantom acts as a SAR amplifier and produces an increase in the maximum local SAR value computed in the models of a factor of 100 (loop implant) – 1000 (wire implant).

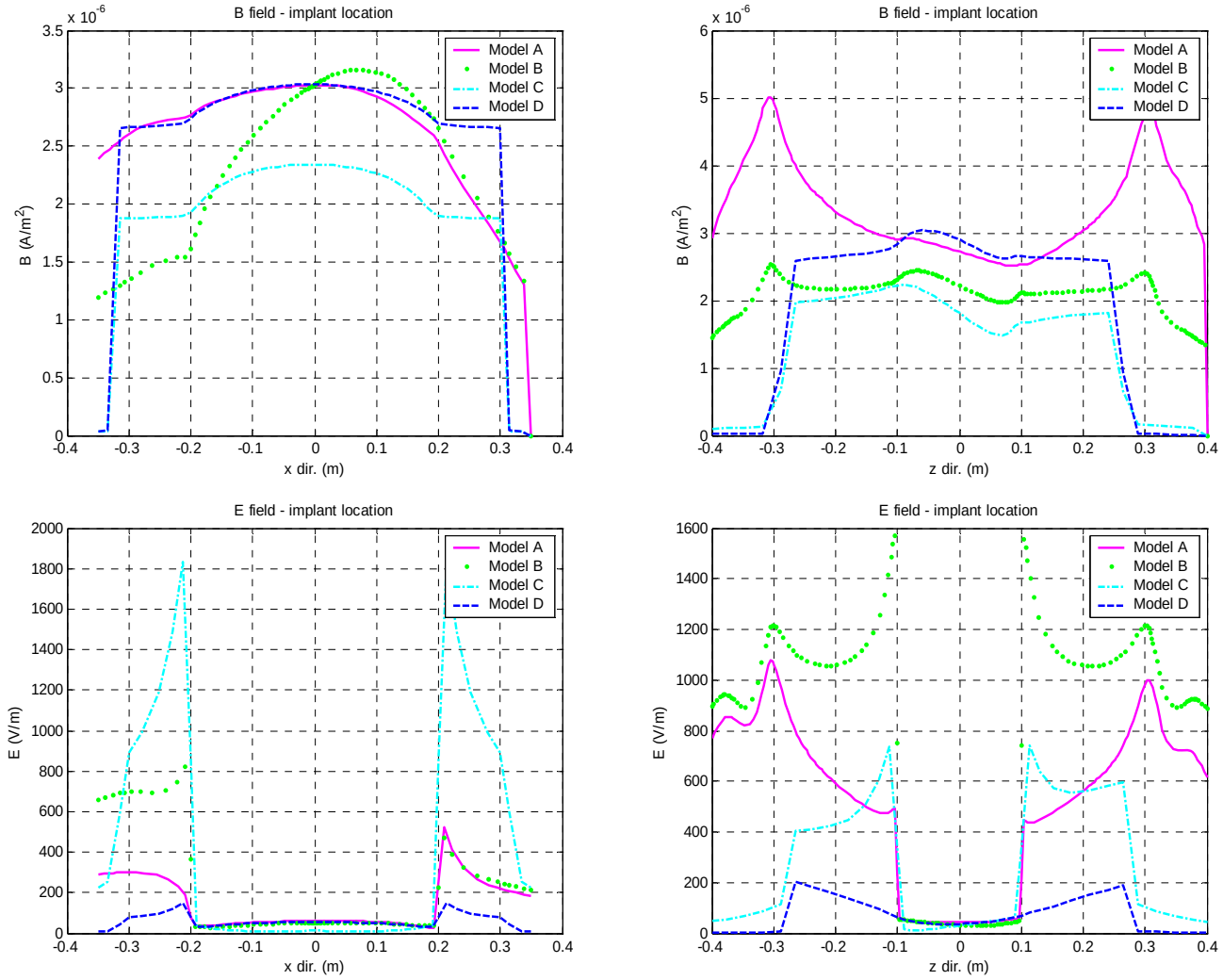

Figure 4. *B* and *E* filed distribution along a longitudinal (x dir.) and transversal (z dir.) line inside the RF coil, through the point of implant positioning

In figure 6 is shown the SAR distribution resulting from the 4 plane waves model with the metallic wire (a) and loop (b) placed inside the dielectric domain. A similar behaviour was as well observed for the other models we developed.

The value of SAR reached at the implant tip is correlated to the level of *E* field at the implant location. For all the simulations performed, we computed the root-mean-square (RMS) value of the *E* vector in the areas covered by the metallic object and we averaged the local SAR over a 2x2 mm^2 surface next to the implant tip (figure 7). Our results show that not only the RMS magnitude of the *E* field is important to determinate the induced SAR, but also the orientation of the vector and the relative magnitude of its components (x, y, z) has to be taken into account. In figure 8 we reported the amplitude of the *E* field components at the implant location for the four models we tested.

As proved by the SAR maps of the phantom with no implants inside, the inversion of the rotating *B* vector modifies the power deposition pattern and thus the amount of SAR reached at the implant tip. Figure 9 refers to the SAR computed at the end of the loop wire, for the two possible orientations of the *B* field.

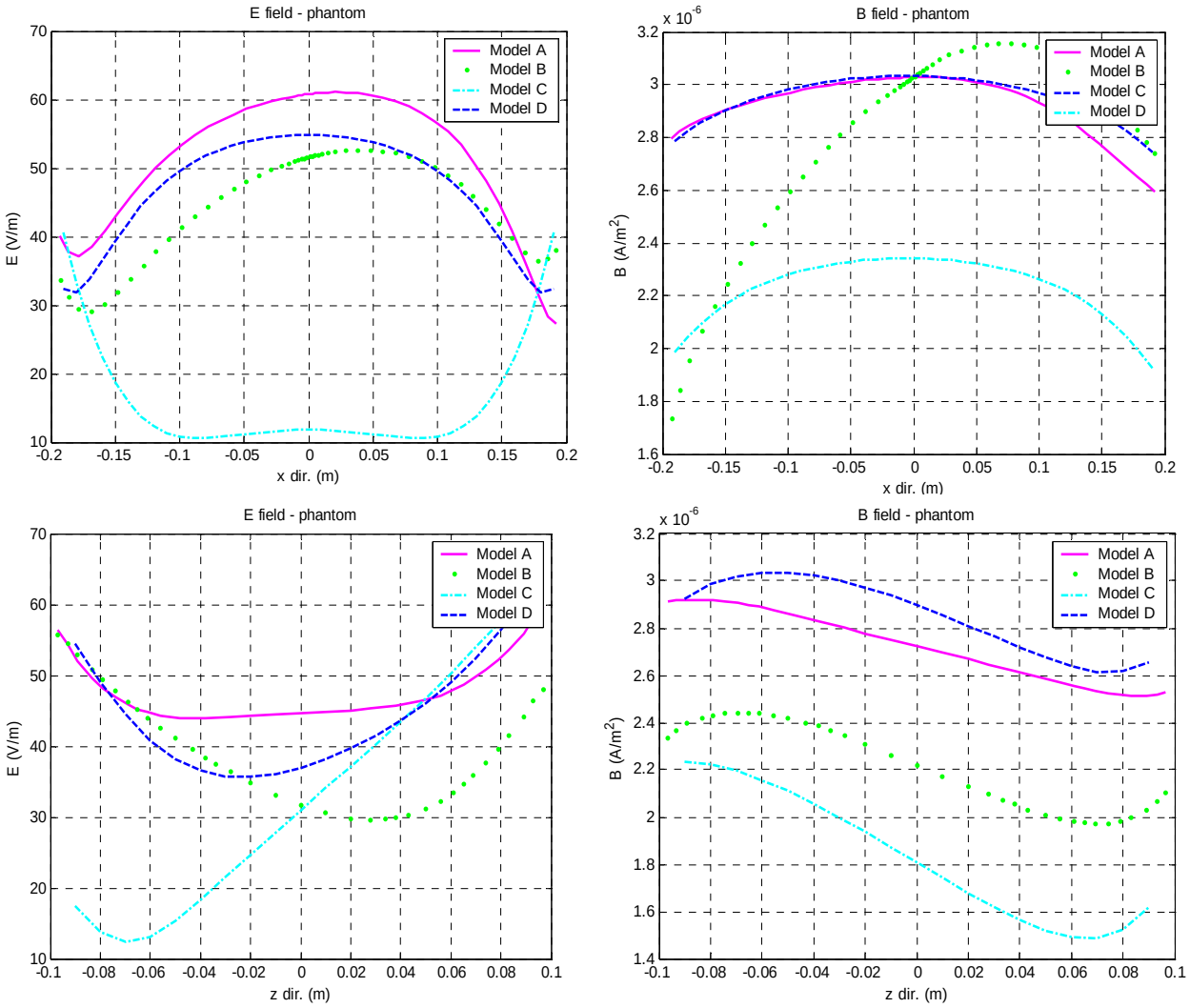

Figure 5. *B* and *E* filed distribution along a longitudinal (x dir.) and transversal (z dir.) line inside the phantom, through the point of implant positioning.

4.4 Discussions

The large number of variables which may be involved in the amount of MRI induced heating on metallic structures make difficult to perform extensive and exhaustive experimental measures. For this reason, the development of numerical models represents a very useful approach to investigate the potential effects of MRI on PMs, ICDs and other active implantable medical devices (AIMDs). However, an ideal simulation

implies that the entire RF coil with its power supply and tuning elements has to be modelled. Such a method

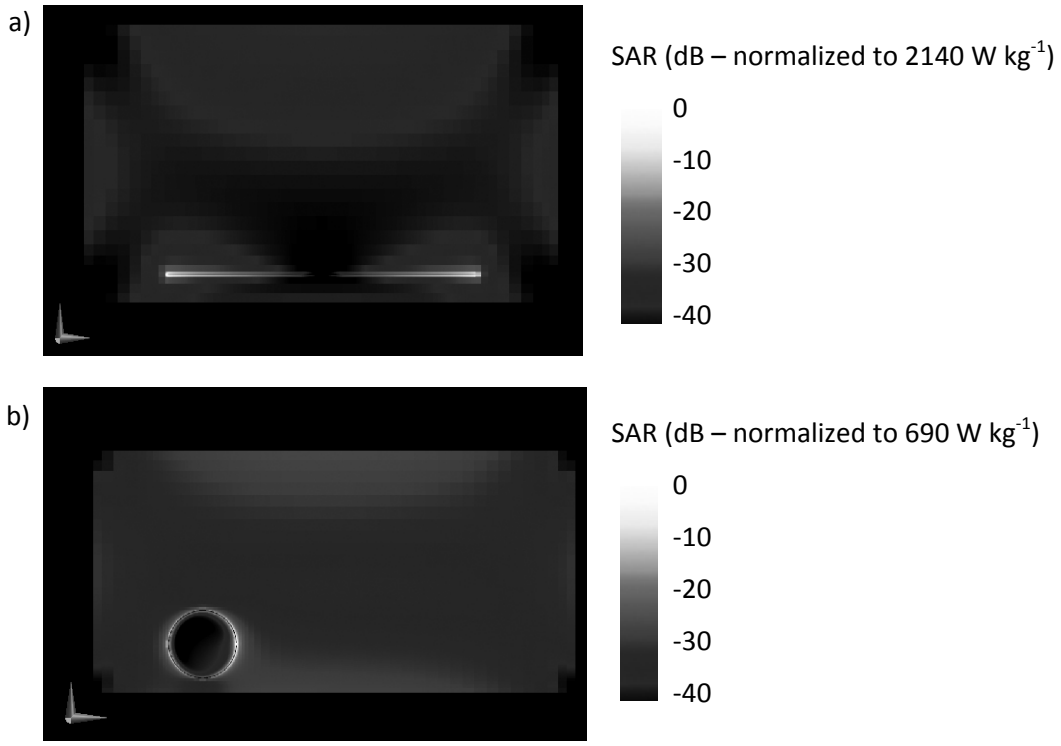

Figure 6. Effect of the presence of the metallic implant inside the dielectric domain on power deposition pattern: straight wire (a) and loop wire (b). The gay-scale maps refer to the 4-plane waves model (model D).

needs very high computational requirements and does not allow to obtain a high resolution in other part of the model, different from the coil (i.e. the patient model or the implant one). In most of the papers dealing with numerical models of MRI RF coil, the circular-polarized *B* field is obtained providing the birdcage resonator with an ideal sinusoidal current distribution: the phase of the waveform of each current source placed in the middle of the birdcage legs, shifted progressively, producing a uniform, circularly polarized RF magnetic field along the circular cross sectional plane inside the coil. Such a model reduces the computational efforts since it does not require the capacitors to tune the coil at the frequency of interest. However, the geometry of the birdcage makes the numerical simulation still rather complex.

The goal for a further simplification should be to model the complex electromagnetic field within an MRI coil with a combination of plane waves, removing completely the birdcage structure. This would make it possible to reduce the computation space to only the patient simulator and the metallic implant. In addition, this would allow computationally efficient investigation of the heating of implants composed of very small structures like thin wires (coiled stent or pacemaker lead) or thin metallic lattices (conventional blood vessel stents with meshes of wires).

The numerical simulations we performed showed clearly that the circular-polarized *B* field cannot be the only element to be reproduced for implants heating computations. The electromagnetic field distribution resulting from the combination of 2 plane waves with a geometrical and time shift of 90° (model C) produces a rotating and homogeneous *B* vector inside the patient simulator, but the SAR map differs substantially from the one of a realistic model of a birdcage coil (model A). Also the temperature increase induced at the tip of the metallic implants (both the straight wire and the loop) are significantly lower than the values computed in the other models.

The comparison between the fully-modelled birdcage (model A) and the coil forced with a sinusoidal current distribution at the middle of each legs (model B) show that, for the same value of SAR averaged over 1 g mass, also the maximum local SAR reached inside the patient simulator does not substantially differ.

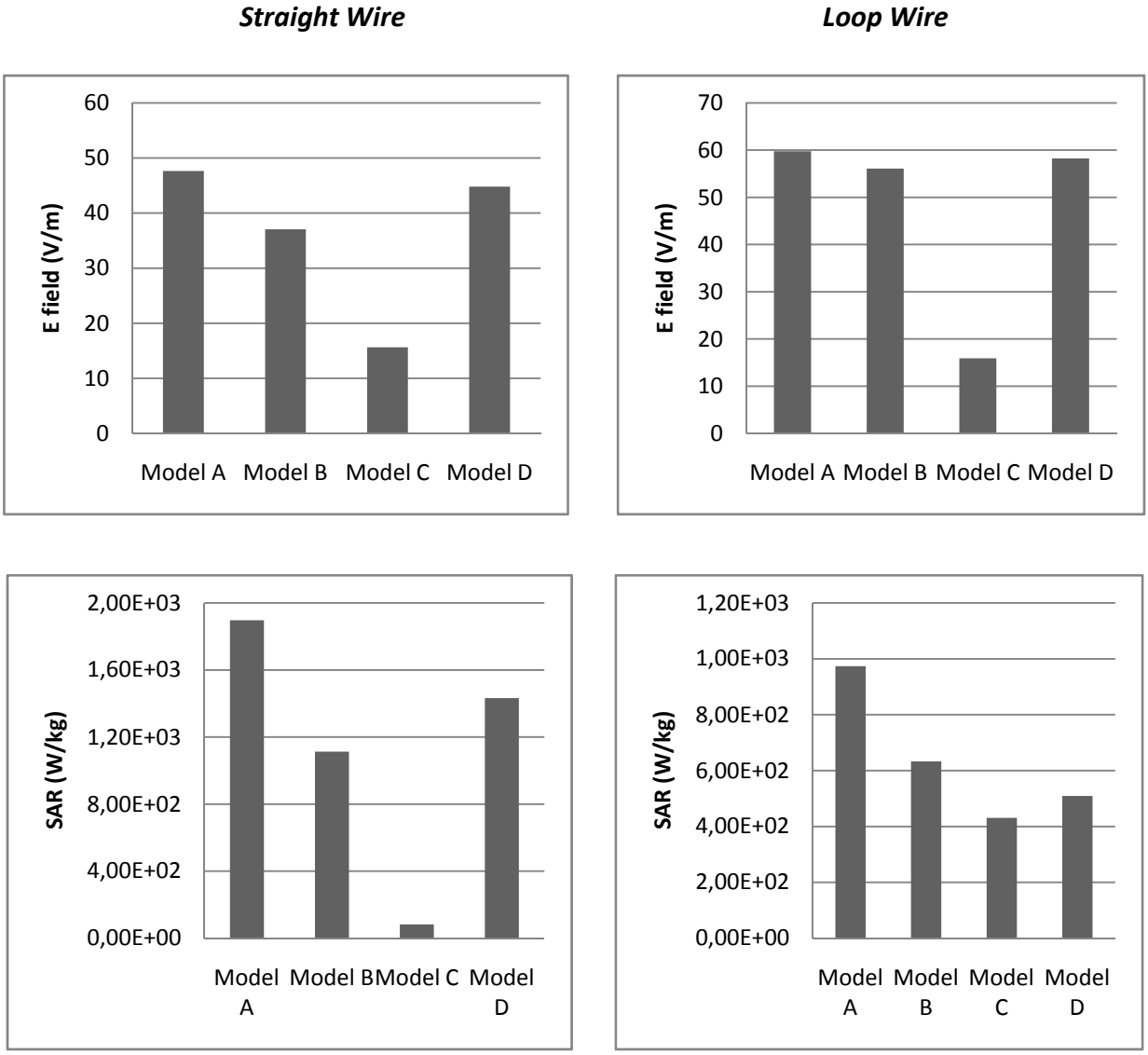

Figure 7. Comparison between the RMS value of the *E* vector in the areas covered by the metallic implants (upper panels) and the local SAR averaged over a 2x2 mm^2 surface next to the implant tip (lower panels).

It means that when the numerical studies aim at calculating the power distribution inside biological tissue with no implants (i.e. where a very fine mesh is not required), the two models can be considered equivalent.

Marked differences are instead shown outside the phantom, near the conductive elements of the coil. The presence of current generators, which impose a fixed current on each leg, determinates high voltage gaps and a high local *E* field. Such differences are significantly reduced inside the dielectric domain, where the field distributions appear quite similar in the two models. However, in model B, both the *E* and *B* field values mapped along a longitudinal and transversal line along the coil are less uniform than in model A, particularly when moving far from the centre of the RF cage. This behaviour may be the explanation for the different amount of SAR computed with the metallic implants inside the phantom: for both the straight wire and the loop, the SAR reached at the implant tip is 35-40% lower in model B than in model A.

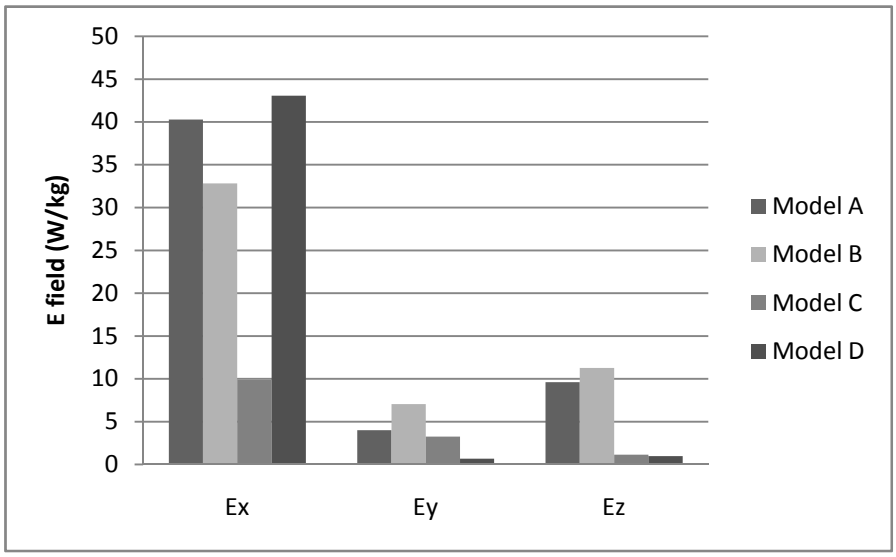

Figure 8. *E* field components at the implant location, for the four FDTD models.

The 4 plane waves model (model D) produced a significant increase in the computational efficiency of the simulation, drastically reducing the number of elements of the FDTD grid and thus the solution time. At the same time, the resulting EM field distribution inside the phantom is surprisingly similar to the one of a fully modelled birdcage coil. Also the SAR computed at the tip of the straight wire is comparable in the two cases. A different behaviour is instead shown with the metallic loop placed inside the phantom: in model D, the amount of SAR is about 50% lower the in model A. The 4 plane waves produce an ideal electromagnetic field: the *B* vector rotates exactly on the y,z plane (transversal respect to the coil), with a null component along the x direction; likewise, the *E* field as only a component greater than zero (E_x), that is the one along the longitudinal axes of the coil. A full modelled birdcage does not produce such an

ideal behaviour, owing to the inevitable differences in the discretization of the different parts of the model. As a consequence, both the *B* and the *E* field will have all the three components greater than zero, producing a better coupling with loop structures.

The simulations performed inverting the rotating *B* vector, demonstrate that the orientation of the magnetic field deeply influences the power deposition pattern and thus the amount of SAR reached at the implant tip, if it is not placed on the plane through the centre of the coil. High SAR areas induced at one side of the phantom may lead to an increase in power deposition higher than 50% respect to the same implant, located in the opposite side of the phantom. The more we move far from the centre of the coil, the more the influence of the *B* field orientation becomes marked.

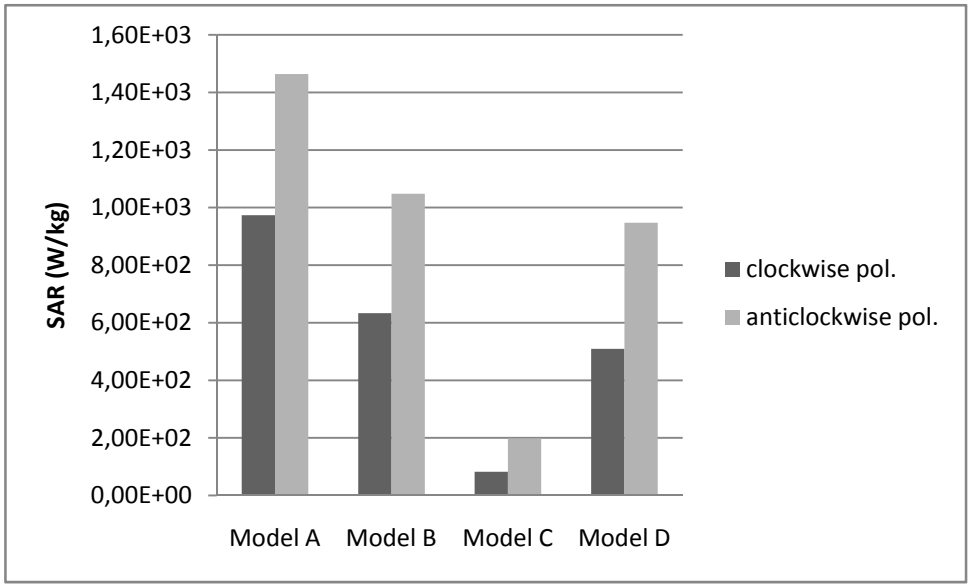

Figure 9. Effect of the *B* vector polarization on the amount of heating induced at the tip of the loop wire.

4.5 Conclusions

Numerical models represents a very useful approach to investigate the amount of SAR induced during MRI procedures on patient implanted with metallic devices. However, in order to obtained reliable results, some important aspects have to be considered during the develop of the model. In most of the MRI birdcage models, the circularly polarized magnetic field is achieved by forcing a sinusoidal current distribution on each leg of the RF coil. Such a simplification leads to similar results respect to a fully modelled birdcage when the numerical study aims at calculating the power distribution inside biological tissue with no implants. If a higher resolution is required, as it happens for the study of the induced heating on thin metallic implants, this model may loose in accuracy and reliability.

In addition, a much more significant simplification can be obtained removing the whole birdcage structure and generating the EM filed inside the RF coil using a combination of plane waves. To this aim, not only the circularly polarized magnetic field but also a homogeneous and symmetric *E* field distribution have to be reproduced: two couples of plane waves that propagates along perpendicular direction allow to achieve the goal.

References

[1] Sommer T, Vahlhaus C, Lauck G, von Smekal A, Reinke M, Hofer U, Block W, Traber F, Schneider C, Gieseke J, Jung W, Schild H. MR imaging and cardiac pacemakers: in-vitro evaluation and in-vivo studies in 51 patients at 0.5 T. Radiology 2000 Jun;215(3):869-79

[2] Achenbach S, Moshage W, Diem B, Bieberle T, Schibgilla V, Bachmann K. Effects of magnetic resonance imaging on cardiac pacemakers and electrodes. Am Heart J. 1997 Sep;134(3):467-7

[3] Konings MK, Bartels LW, Smits HF, Bakker CJ. Heating around intravascular guidewires by resonating RF waves. J Magn Reson Imaging. 2000 Jul;12(1):79-85

[4] Bassen H, Kainz W, Mendoza G, Kellom T. MRI-induced heating of selected thin wire metallic implants--laboratory and computational studies -- findings and new questions raised. Minim Invasive Ther Allied Technol. 2006;15(2):76-84

[5] Rezai AR, Baker KB, Tkach JA, Phillips M, Hrdlicka G, Sharan AD, Nyenhuis J, Ruggieri P, Shellock FG, Henderson J. Is magnetic resonance imaging safe for patients with neurostimulation systems used for deep brain stimulation? Neurosurgery 2005 Nov;57(5):1056-62

[6] Kanal E. White Paper on MRI Safety. American Society of Neuroradiology, May 24, 2005, Toronto, Canada

[7] Helfer JL, Gray RW, MacDonald SG, Bibens TW. Can pacemakers, neurostimulators, leads, or guide wires be MRI safe? Technological concerns and possible resolutions. Minim Invasive Ther Allied Technol. 2006;15(2):114-20

[8] Ho H. Safety of Metallic Implants in Magnetic Resonance Imaging. Journal of Magnetic Resonance Imaging. 2001;14: 472–7

[9] Trakic A, Crozier S, Liu F. Numerical modelling of thermal effects in rats due to high-field magnetic resonance imaging (0.5-1 GHZ). Phys Med Biol. 2004 Dec 21;49(24):5547-58

[10] Liu F, Beck BL, Fitzsimmons JR, Blackband SJ, Crozier S. A theoretical comparison of two optimization methods for radiofrequency drive schemes in high frequency MRI resonators. Phys Med Biol. 2005 Nov 21;50(22):5281-91

[11] ASTM F2182–02a – ‘‘Standard Test Method for Measurement of Radio Frequency Induced Heating Near Passive Implants During Magnetic Resonance Imaging’’, ASTM International, 100 Barr Harbor Drive, PO Box C700, West Conshohocken, PA, 19428–2959 USA

Chapter 5

Radiofrequency dosimetry in subjects implanted with metallic structures undergoing MRI: a numerical study

E Mattei[1]**, M Triventi**1**, G Calcagnini**[1]**, F Censi**[1]**, and P Bartolini**[1]

[1] Department of Technologies and Health, Italian National Institute of Health, Roma, Italy

Abstract

A numerical study to investigate the effects of the exposure to radiofrequency (RF) field on biological tissues implanted with thin metallic structures has been carried out, using the finite difference time domain (FDTD) solution technique. The particular case of the RF used in the clinical 1.5 T magnetic resonance imaging (MRI) scanners has been studied. The results of the model show that the presence of a metallic wire yields to a significant increase in the local specific absorption rate (SAR) and in temperature around the implant. Present standards or guidelines do not specifically address this problem and use threshold levels and methods to define safe exposure conditions that cannot apply to reveal high SAR gradients, such as the ones generated by thin metallic implanted objects. In particular, an averaging mass of 10 g, typically used as averaging volume for SAR calculation to evaluate the effect of RF exposure of biological tissues, is too big if compared to the SAR gradient generated by thin metallic structures. The SAR estimation according to this method cannot be considered a reliable indicator to evaluate the potential damage due to the RF induced heating at the interface between the implant and biological tissues. Five wires of different lengths and thicknesses were simulated and the SAR at the wire tip was evaluated over 10g, 1g, 0.1g averaging mass: the SAR underestimation related to the 10g and 1g masses, compared to 0.1g mass, was greater than 90 % and 60 %, respectively. In conclusion, present standard cannot be applied to thin metallic implants. The amount of averaging mass should be chosen as a function of the dimension of the implanted object and of the SAR gradient that is generated around it. At the same time, the averaging volume has to be not too small to be just a single "hot spot", not relevant for the evaluation of potential tissue damage due to RF exposure.

5.1 Introduction

Everyone is exposed to a complex mix of radiofrequency (RF) electromagnetic fields range that permeate our environment and that are increasing significantly as technology advances unabated and new applications are found. Exposure to RF involved either unintentional and intentional electromagnetic (EM) sources: unintentional exposures are generated by all sources that are not indented to interact directly with biological tissues, such as high voltage power lines, broadcasting networks, mobile telephones and their base stations. On the other hand, intentional sources generate EM field in order to produce a specific effect on particular body regions. The radiofrequency signal used in magnetic resonance imaging (MRI) represents an example of an intentional RF source. Public and workers exposure to RF is regulated by a variety of voluntary and legal limits, together with various international and national safety standards. In the 1998, the International Commission on Non-Ionizing Radiation Protection (ICNIRP) published a guideline for limiting RF exposure and for providing protection against known adverse health effects, both from intentional and unintentional sources, direct and indirect effects [1]. Direct effects result from direct interaction of fields with the body; indirect effects involve

interactions with an object at a different electric potential from the body and coupling mechanisms of RF to medical devices worn by, or implanted in, an individual. The ICNIRP standards identify the exposure limits for time-varying electric, magnetic and electromagnetic fields, up to 300 GHz, and also address a particular chapter to the threshold levels of exposure during MRI examinations. These documents deeply analyse the direct effects of RF exposure and fix the threshold levels at which potential adverse health consequences might occur. Instead, the coupling mechanisms of RF to implanted medical devices are not considered in these guidelines.

MRI has become an established diagnostic modality. The clinical usefulness of in-vivo magnetic resonance spectroscopy (MRS) was demonstrated in several instances and is being explored further. These techniques involve exposure of the patient to static and time-varying magnetic fields and radiofrequency electromagnetic fields. In particular exposure situations, these fields may pose a health hazard, especially with regards to RF energy deposited (specific absorption rate – SAR) in the body during an MRI examination and that is converted to heat, which will be distributed largely by convective heat transfer through blood flow. As the body temperature increases, there will be an increase in blood flow and cardiac output, as well as an increase in sweat secretion and evaporation.

ICNIRP guidelines provide information on levels of exposure and health effects from magnetic and radiofrequency electromagnetic fields associated with MRI diagnostic devices, and on precautions to be taken to minimize health hazards to patients undergoing MRI examinations. Concerning with the RF field, for whole-body exposures or exposures to the head and trunk, no adverse health effects are expected if the increase in body temperature does not exceed 1 °C. In the case of infants, pregnant women, and persons with cardiocirculatory impairment, it is desirable to limit temperature increases to 0.5°C. In practice, due to its thermal capacity, no tissue will increase in temperature at a rate more than 1°C h^{-1} for each W kg^{-1} of power deposition. Considering the modifying effects of blood flow and environmental heat exchange, no adverse health effects are to be expected in persons without cardiovascular abnormalities exposed to 2 W kg^{-1} for 1 h. In persons with cardiovascular abnormalities, 1 W kg^{-1} for 1 h is an acceptable level, provided proper monitoring is instituted.

In MR exposures up to 1 h, the total body exposure should be limited to a total energy deposition of 120 W min kg^{-1} in order not to overload the thermoregulatory system. To avoid overheating any local area, the product of time and local SAR should not exceed:

- 60 W min kg^{-1} averaged over the head, or
- 120 W min kg^{-1} averaged over the trunk, or
- 180 W min kg^{-1} averaged over the extremities,

provided that the instantaneous SAR does not exceed:

- 4 W kg^{-1} averaged over the head, or
- 8 W kg^{-1} averaged over the trunk, or
- 12 W kg^{-1} averaged over the extremities.

To protect poorly perfused tissues, the eyes for example, such tissues should not be exposed to a local SAR of more than 10 W kg^{-1}, averaged over 10 g for more than 10 min.

Since the exposure to the MRI field is not supposed to be a usual condition for public, such thresholds extend towards higher levels the general safety values recommended by ICNIRP. In the frequency range from 100 kHz to 10 GHz, the limit for head and trunk is 10 W kg^{-1} averaged over any 10 g mass of tissue for occupational situations; for the general public, this value goes down to 2 W kg^{-1}, always averaged over any 10 g mass of tissue. However these values are intended to limit the temperature increase induced by EMF for general public and consider only the different sensitivity of various types of tissue to thermal damage. To extend such limit values also to patients implanted with metallic wires and/or active medical devices some considerations are needed. When a patient implanted with conductive structures is exposed to EMF, the metallic object may operate as an antenna which causes an increase in power deposition around the wire or catheter. With regards to the RF field generated by an MRI scanner, several studies have investigated, both in vivo and in vitro, the potential adverse effects on PMs (PM), implantable cardioverters (ICD) [2-6], brain stimulator [6,7], cochlear implants [8], stent [9,10] and other similar implantable devices. This increase in the local SAR is generally limited to a very small region (comparable to the dimensions of the metallic wire [11]), so that the induced temperature increase is unlikely to produce dangerous systemic effect for the patient. However, harmful effects in the region the surrounds the metallic implant might still occur and modify the interface between the implant and biological tissues. As a consequence, if the implanted device implies energy transfer towards biological tissues (as for the case of leads used in PM, ICD, cochlear implants, brain stimulators…) the correct behaviour of the device could not be guaranteed any more.

In this study we numerically reproduce an EMF exposure at 64 MHz (RF field used by 1.5 T MRI clinical scanners) that results in maximum SAR values below the safety thresholds of the present international standards and guidelines, on a rectangular phantom which simulates biological tissues, implanted with a thin metallic wires.

Aims of the paper are:

1. to show the effect of thin metallic structures on the local distribution of the electric field and the associated SAR;
2. to determine to what extent the present standard methods for SAR evaluation are appropriate in the presence of thin metallic structures;
3. to propose a refinement of the actual standard to meet the constraint of this particular application.

5.2 Methods and materials

We developed a simple numerical model in order to calculate the SAR distribution inside a homogeneous domain, with electromagnetic properties similar to those of biological tissues, implanted with metallic

wires (Figure 1). The model was exposed to a combination of plane waves, able to generate a pure circular polarized magnetic field [12], that is the typical exposure used during MRI investigations. We used commercial FDTD (Finite Difference Time Domain) software (SEMCAD X, version 11.0, SPEAG, Zurich) that incorporated native drawing. The software had a variable grid (graded-mesh) generator and was used on a personal computer with a 2.4 GHz, 32-bit processor, 2 GB of RAM, and a Windows XP operating system.

The frequency we tested is 64 MHz, corresponding to the RF used by the MRI scanners today most used in the clinical practice, that work with a static magnetic field of 1.5 T. The plane waves propagates inside an 610mmx350mmx115mm box, drawn by using the native 3-D modelling section of the software and simulating a homogeneous portion of biological tissues. The physical properties assigned to this domain are reported in Table I. A rectangular plastic box filled with saline solution has been widely used in both numerical and in-vitro studies on electromagnetic interference to simulate the human trunk [11,13,14]. Inside the box we placed metallic wires of different thickness and length:

1) wire 1: diameter =1 mm; length =25 cm;
2) wire 2: diameter =2 mm; length =25 cm;
3) wire 3: diameter =3 mm; length =25 cm;
4) wire 4: diameter =2 mm; length =15 cm;
5) wire 5: diameter =2 mm; length =40 cm;

The thickness of the wires were chosen according to what are the typical dimensions of a metallic implant, such as a PM, ICD or brain stimulator lead. A 25 cm-long wire is close to the theoretical resonance length at 64 MHz inside the dielectric domain we modelled; 15 cm and 40 represent a condition of an implant far from its resonance length, too short or too long, respectively. All the wires were positioned 2 cm far from the side surfaces of the box.

The graded mesh software allowed us to generate a non-uniform grid for the FDTD solution: at the lead tip, the mesh was generated with a fixed step of 0.25 mm. Over the area covered by the implant a minimum step of 0.5 mm, a maximum step of 5 mm and a growth factor of 1.3 were used. In the other parts of the model the grid parameters are: 1 mm minimum step; 50 mm maximum step; 1.3 growing factor. The duration of the RF exposure was 10 periods, with an initial ramped interval of 2 periods. SEMCAD implements a particular algorithm for the SAR extraction according to the IEEE P1529 standard (Recommended Practice for determining the spatial-peak SAR associated with the use of wireless handsets - computational techniques) [15]. This algorithm allows to compute the spatial-peak SAR over any required mass. All different tissue types, organs or parts of the model can be selected for the averaging process.

Table I. Physical properties of the dielectric material used in the numerical model to simulate biological tissues.

Properties	Value @ 64 MHz	Unit
Rel. Permittivity	79	-
Rel. Permeability	1	-
Electrical Conductivity	0.6	S m^{-1}
Magnetic Conductivity	0	Ohm m^{-1}
Density	1007.5	Kg m^{-3}
Specific Heat Capacity	4178.6	J kg^{-1} K^{-1}
Thermal Conductivity	0.2	W m^{-1} K^{-1}

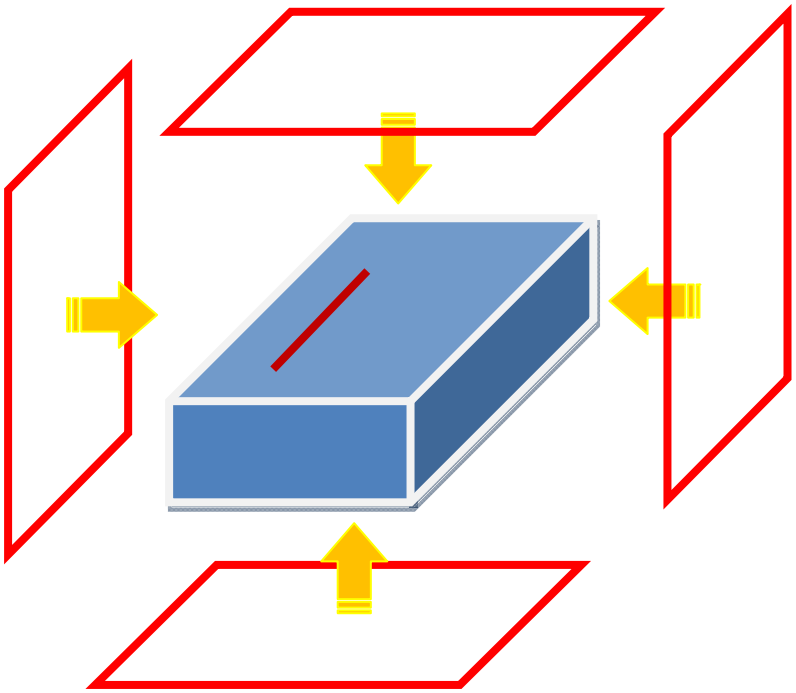

Figure 1. Schematic representation of the numerical model. The exposure conditions are obtained using two couples of plane waves; in each couple, the plane waves propagate on parallel but opposite directions, with concordant B vector component and opposite E vector component. Between the two couples, a 90° shift both in space and in time was applied. A circular-polarized magnetic field is thus reproduced.

We performed preliminary simulations without the wire, in order to set the amplitude of the plane waves to produce inside the dielectric domain a whole-body mean SAR of 2 W kg^{-1}, (maximum value accepted in standard MRI clinical investigations). The FDTD grid adopted in these simulations was the same used in the following numerical studies, where a metallic implants was placed inside the dielectric material: a much finer grid was thus produced in the area where the metallic wires will be located, so to ensure a correct comparability for the results computed.

Keeping the amplitude of the plane waves constant, we repeated the simulations with the wires placed inside the dielectric domain. We calculated the values of SAR averaged over 1 g (SAR_{1g}) and 10 g ($SAR1_{0g}$), using the IEEE P1529 algorithm. In order to evaluate the SAR field distribution in close proximity to the wire tip surface, we averaged the local SAR over 0.1 g mass ($SAR_{0.1g}$) of the dielectric material. Given the physical properties of the domain used to simulate biological tissues, a 10 g mass corresponds to a cubic region of 22x22x22 mm^3, 1 g mass to a 10x10x10 mm^3 region, 0.1 g mass to a 5x5x5 mm^3.

Additional simulations were performed increasing the number of voxel in the model, in order to be sure that a finer mesh do not affect any of the parameters we used in our analysis.

For the five wires, the SAR gradient has been computed and compared: as outcome of the study, we want to identify a possible relation between the implant dimensions and the SAR gradient, so to find the optimal averaging mass as a trade-off between a volume small enough to cover significantly high SAR value and, at the same time, big enough to avoid the case of a local “hot spot”, not relevant for the tissue damage.

Always using the same grid, we then coupled the electromagnetic solution with a thermal analysis inside the dielectric domain. As done for the SAR calculation, we first computed the temperature increase without the wire; then we investigated how the presence of the metallic implant might change the temperature distribution. With regard to the thermal properties assigned to the dielectric domain, we reproduced a worse-case condition, since we assumed the conduction as the only contribute to the heat transfer (no convection).

The thermal simulation was performed for a total time of 2000 s, with the RF source active after 200 s to the end.

5.3 Results

The plane waves at 64 MHz used as RF source produced a maximum SAR_{10g} of 7.6 W kg^{-1} inside the dielectric material, without the metallic wire. If averaged over 1 g or 0.1 g, no significant changes were observed in the maximum SAR value computed (7.1 W kg^{-1} and 7.8 W kg^{-1}, respectively).

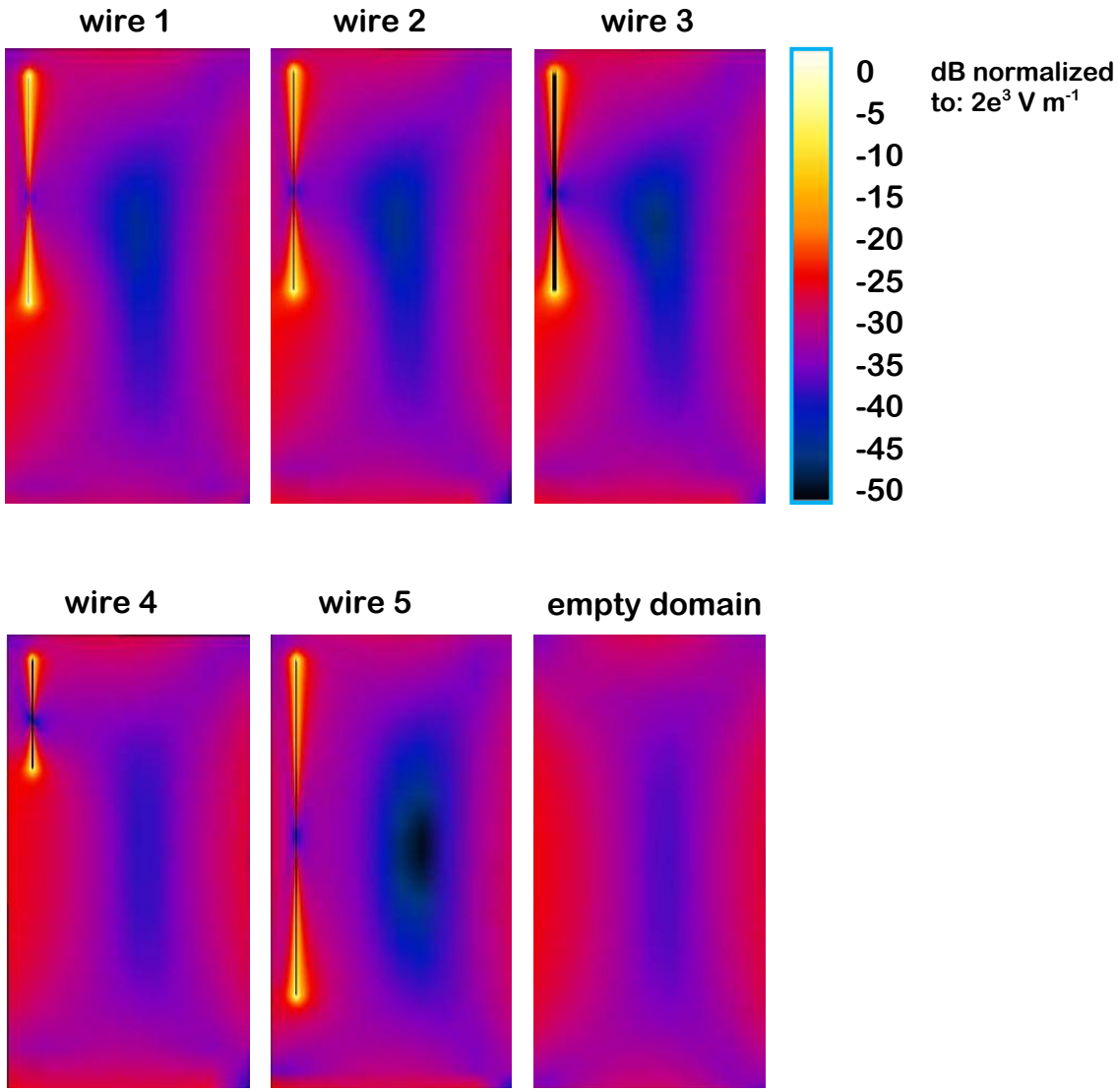

Figure 2. E field pattern inside the dielectric domain. Wire 1: diameter=1 mm; length=25 cm; wire 2: diameter=2 mm; length=25 cm; wire 3: diameter=3 mm; length=25 cm; wire 4: diameter=2 mm; length =15 cm; wire 5: diameter =2 mm; length=40 cm.

The electromagnetic pattern deeply changes when a metallic implant is placed inside the box. In Figure 2 we reported the E field distribution inside the dielectric domain, with and without the metallic implants, for the five wires we studied. Figure 3 shows the SAR distribution resulting from the numerical model of the dielectric material implanted with the 2 mm-thick wire. The increase in the local SAR is detectable either if using the 10 g, 1 g and 0.1 g averaging mass, even if the estimated maximum deposited power at the lead tip markedly differs (SAR_{10g} =44.0 W kg^{-1}, SAR_{1g}=197.0 W kg^{-1}, $SAR_{0.1g}$ =737.1 W kg^{-1}). In order to compare the averaging volumes with the dimensions of the SAR gradient, we plotted over the power distribution resulting around the lead tip, the cubic regions corresponding to 10 g, 1 g and 0.1 g mass. Figure 4 refers to the 2 mm-thick, 25 cm-long wire.

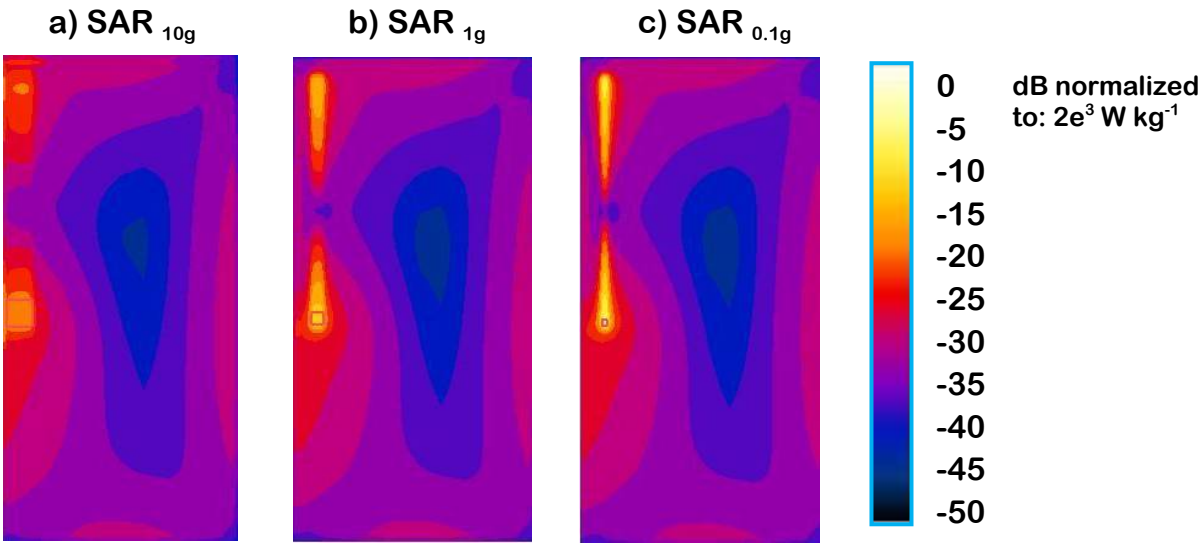

Figure 3. SAR distribution resulting from the numerical model of a dielectric box implanted with the 2 mm-thick, 25 cm-long wire: transversal section through a plane containing the implant. a) SAR averaged over 10 g mass; b) SAR averaged over 1 g mass; c) SAR averaged over 0.1 g mass.

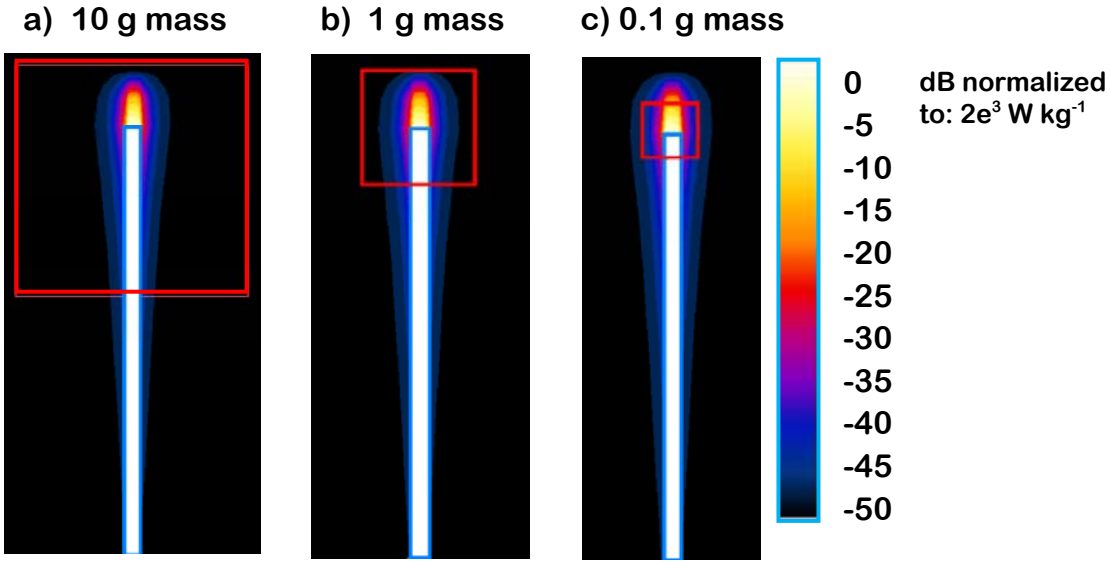

Figure 4. Comparison between the RF induced SAR gradient around the lead tip and the averaging mass use to evaluate the local SAR: a) 10 g mass; b) 1 g mass; c) 0.1 g mass.

In figure 5, a, the SAR_{10g}, SAR_{1g} and $SAR_{0.1g}$ are compared for the five wires we modelled. Keeping the SAR value averaged over 0.1 g as reference, we calculated the underestimation related to bigger averaging masses (10 g and 1g), for the three thicknesses and the three lengths we simulated : the results are presented as percentage underestimation in figure 5, b.

We also compared the dimensions of the SAR gradients: the graphs reported in figure 6, a, show the SAR exponential decrease along a line parallel to the wire, starting from the tip towards the dielectric domain.

For the 1 mm-thick wire, SAR goes down to the 20% of the maximum value at about 2.5 mm from the metallic surface. As the dimensions of the tip increase, the extent of the SAR peak becomes larger: the 20 % of the maximum value is reached approximately at 3 mm away for the 2 mm lead and at 4 mm away for the 4 mm lead.

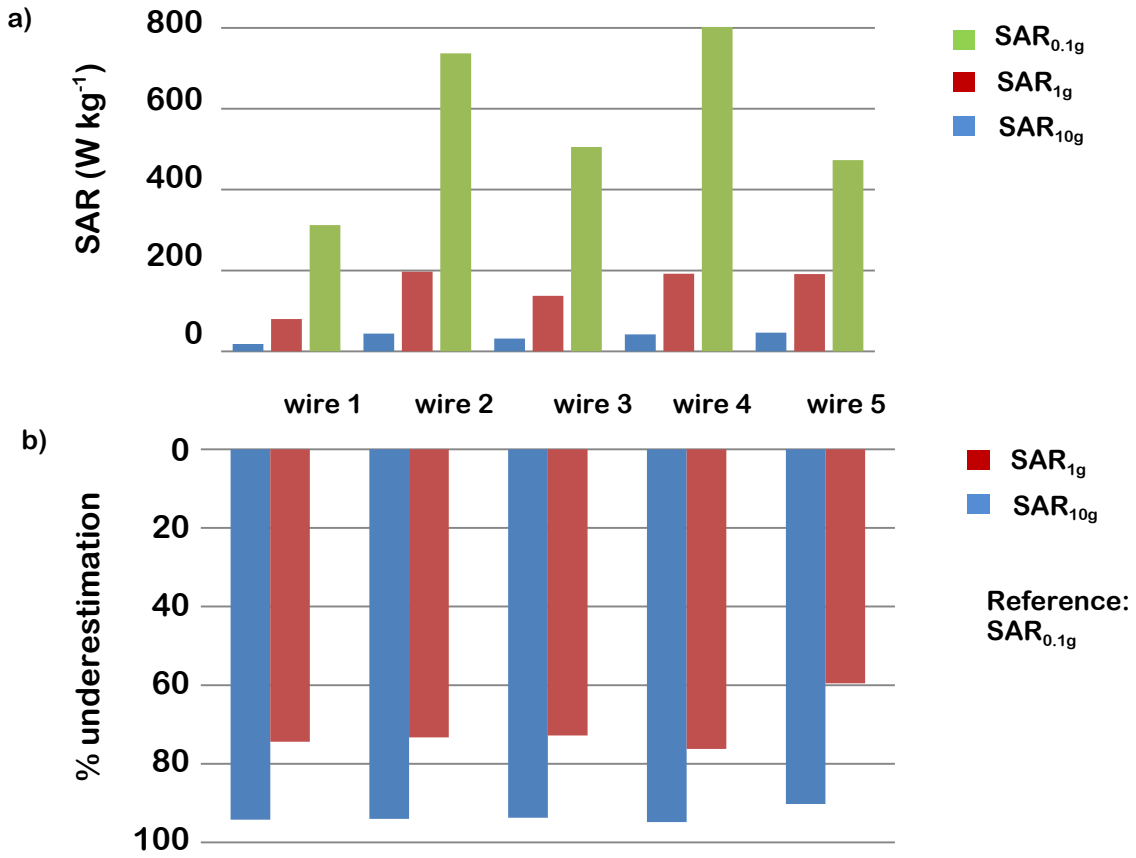

Figure 5. a) Comparison between the maximum SAR computed over different averaging masses. b) Percentage underestimation related to the SAR calculation made on an average volume of 10 g and 1 g, having as reference the SAR value computed over 0.1 g. Wire 1: diameter=1 mm; length=25 cm; wire 2: diameter=2 mm; length=25 cm; wire 3: diameter=3 mm; length=25 cm; wire 4: diameter=2 mm; length =15 cm; wire 5: diameter =2 mm; length=40 cm.

On the other hand, the SAR gradient computed for the wires of different length is much more similar, in spite of quite different maximum SAR value reached at the wire tip (Figure 6, b).

The thermal analysis performed assuming no convection inside the dielectric domain, for a heating period of 1800 s, reveals that the induced current flowing from the metallic lead inside the lossy material generates high temperature increase all around the tip. The heating induced by the RF source in the empty phantom is, on the other hand, rather low (≈ 2°C). In figure 7 we reported the temperature rises at different distances from the lead tip, for the 1 mm, 2 mm and 4 mm-thick wires. The highest temperature is obtained for the thinnest wire (temperature increase ΔT=30.8°C), whereas for the 2 mm and for the 4

mm lead the temperature increase is as low as ΔT=15.9°C and ΔT=9.1°C, respectively. The tip dimensions influence also the temperature gradient that rises around the implant: the thicker is the wire, the less is the difference between the temperature profiles sampled at 0 mm, 1 mm, 2 mm and 3 mm away from the tip.

On the other hand, when comparing the induced heating for the wires of different length (figure 8), the temperature gradients seem quite similar, in spite of pretty different absolute temperature values reached at the wire tip.

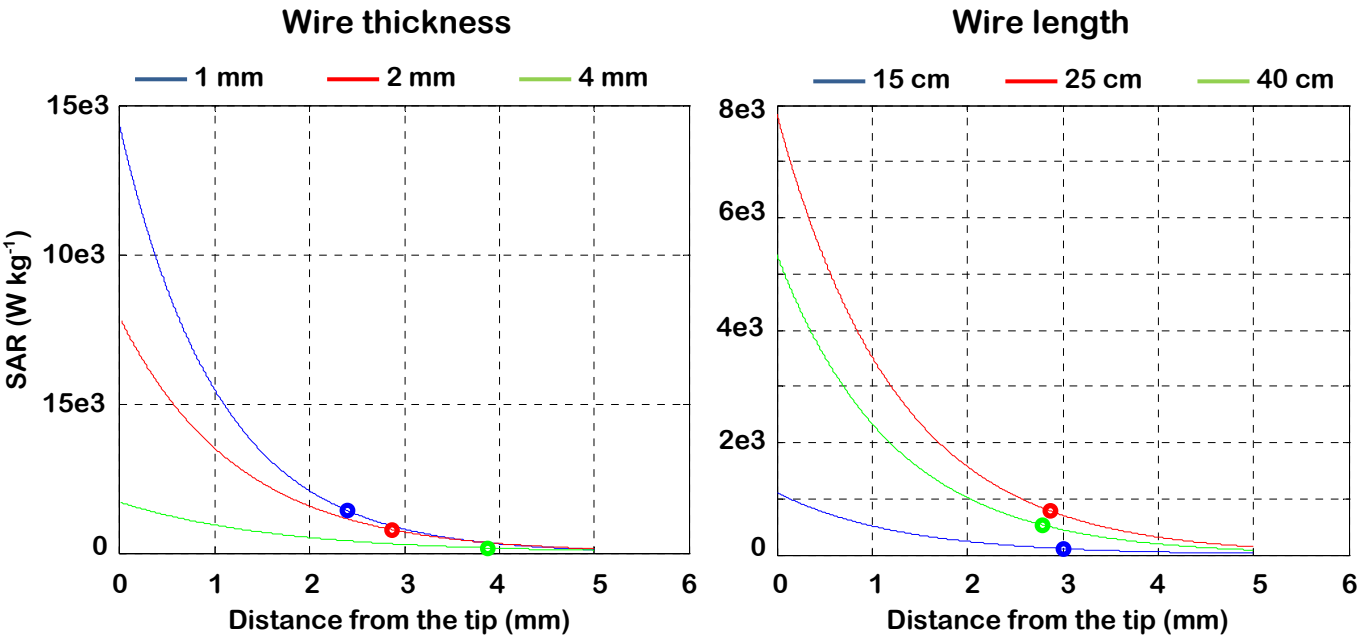

Figure 6. SAR exponential decrease along a line parallel to the wire, starting from the tip towards the dielectric domain. a) 1 mm, 2 mm, and 4 mm-thick wires. b) 15 cm, 25 cm, and 40 cm-long wires. Circles indicate the distance at which the 20% of the maximum SAR is reached.

5.4 Discussion

In the 100 kHz to 10 GHz frequency range, a limit of 2 W kg^{-1} represents the highest threshold below which no significant harmful effects occur to any kind of biological tissues, according to the present international standards. For the exposure of biological tissues to the RF field generated by an MRI scanner, ICNIRP guidelines extend towards higher levels than the general safety values. In the frequency range from 100 kHz to 10 GHz the maximum localized SAR in the head and trunk is limited to 10 W kg^{-1} averaged over any 10 g mass of tissue, in case of occupational situations; for the general public, this value goes down to 2 W kg^{-1}, always averaged over any 10 g mass of tissue.

However, such values come out from several studies [16-19] involving general public and cannot be immediately extended also to patients implanted with metallic devices, such as PMs, ICD, brain

stimulator or cochlear implants. In particular, the methods suggested in present standards for the local SAR evaluation do not take into account the presence of thin metallic implants, which might cause very high SAR gradient, and thus could result in misleading evaluations of the deposited power.

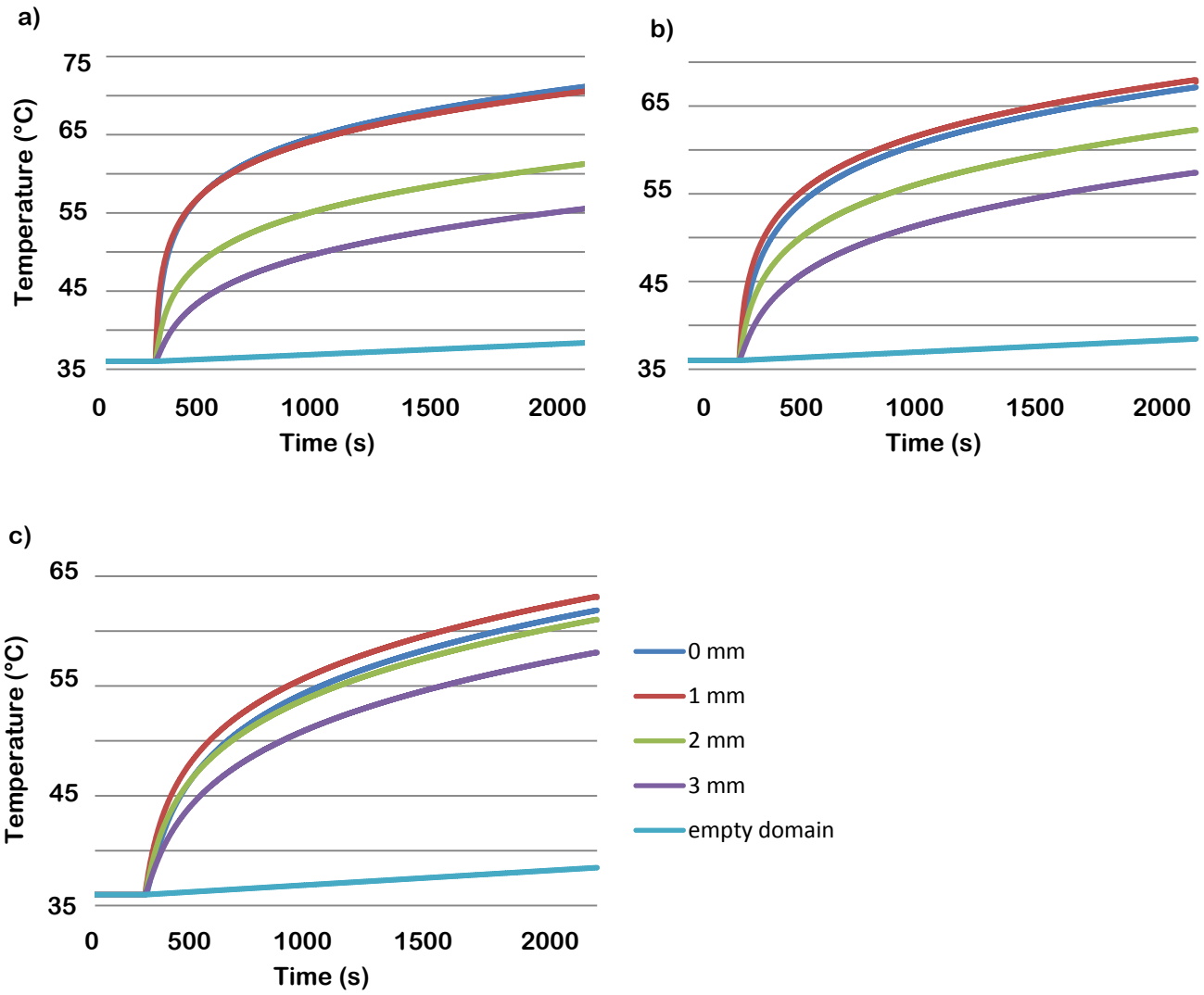

Figure 7. Temperature increase at different distances (0 mm, 1 mm, 2 mm, 3 mm) from the wire tip: a) 1 mm-thick wire; b) 2 mm-thick wire; c) 4 mm-thick wire. In each graph the temperature increase cause by the RF source inside the empty phantom is also reported.

In this paper we developed a numerical model to show the effect of thin metallic structures on the local distribution of the electric field and the associated SAR, and to determine to what extent the currently accepted methods for SAR evaluation are appropriate in the presence of thin metallic structures; In addition we propose a criteria to chose an appropriate averaging mass to be used to evaluate the power deposited by thin metallic structures in biological tissues.

The presence of a metallic object may cause an increase in the power deposition which might lead to adverse health consequences. Calculations of RF induced temperature increase for a realistic numerical

model of human tissues, in absence of metallic structures, developed both with the finite element or the FDTD technique [20,21], show a maximum rise of about 1 °C from the absorption of 10 W kg^{-1}. ICNIRP localised SAR limits have been chosen not to exceed such a value, and it is recommended that an averaging mass of 10 g is used to calculate the induced SAR. Such a value is chosen to take into account the inhomogeneous spatial distribution of energy absorbed, which may result in significant heating of particular anatomic districts.

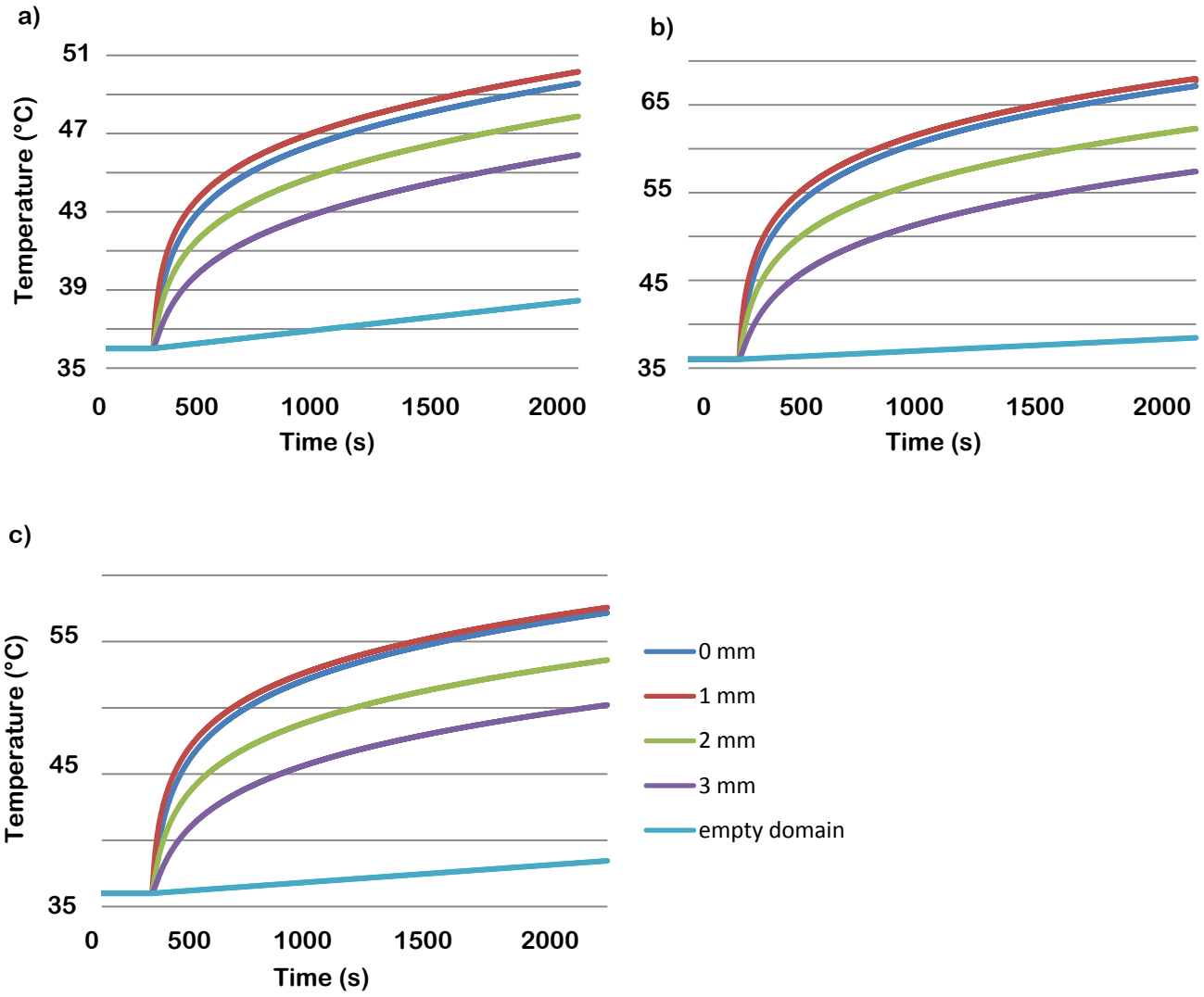

Figure 8. Temperature increase at different distances (0 mm, 1 mm, 2 mm, 3 mm) from the wire tip: a) 15 cm-long wire; b) 25 cm-long wire; c) 40 cm-long wire. In each graph the temperature increase cause by the RF source inside the empty phantom is also reported.

When a RF field interacts with tissues implanted with thin metallic structures, it generates very high SAR gradients, which make the spatial distribution of energy absorbed much more inhomogeneous. Inside the metallic object, considered as a perfect conductor, the E field disappears, whereas outside the field lines bend perpendicular to the surface of the implant. If the surface area is small, a dense electromagnetic flux

may arise near the wire. In lossy tissues, this leads to higher power absorption near the implant, compared to the same tissue with no implant. Thus, in case of thin metallic structures, an averaging mass of 10 g might be too big to reveal the local increase in power deposition and significantly underestimate the effect of EMF exposure. SAR values computed for lead models of different radius show that the SAR gradient decreases to negligible values at a distance from the tip comparable to the diameter of the lead itself. For a 2 mm-thick wire (value close to the real dimension of a PM or ICD lead), a 10 g mass results in a cube whose side is more than 10 bigger than the diameter of the lead. If averaged over 0.1 g mass (i.e. over a 5x5x5 mm^3 region), the resulting maximum local SAR at the lead tip is about 90% greater than the 10 g averaged SAR. The results of the numerical model we developed show that even the 1 g averaging mass is too big if compared to the dimensions of the SAR gradient that rises around the wire tip (about 70% less than the 0.1 g averaged SAR).

The comparison between the SAR distributions computed for wires of different thickness and length shows that the diameter of the metallic implant is the element that plays the major role in determining the gradient dimensions: the thicker is the wire, the slower is the exponential decay of the deposited power around the tip. Another aspect that needs to be taken into account is the SAR peak value at the wire tip; however, the SAR gradients that rises around wires of different length have comparable dimensions, in spite of SAR peak values pretty different. It suggests that, more than the length, the thickness of the metallic implant is the discriminate element that must be considered in order to identify the optimal averaging mass for a reliable SAR evaluation.

The localised SAR values we found were significantly higher than the limits defined by the ICNIRP guidelines. Such limits have been chosen for averaging volumes of 1 g and 10 g, in order not to exceed 1°C in temperature rise, threshold beyond which adverse health effects may occur [1]. In our numerical study, SAR was computed over smaller volumes and thus our results cannot be immediately related to a increase in local temperature dangerous for the patient. High SAR values involve only very small region, comparable with the dimension of the implant, and thus are unlikely to cause adverse systemic effects that could compromise the patient safety. However, some considerations still need to be done. In particular, the RF power deposited around the metallic structure might modify the interface between the implant and the biological tissue, causing, for example, a variation in the contact impedance seen by the implant. As a consequence, all the medical devices that require an energy transfer from the implant to the tissue or that need to read biological signals, might not work properly anymore.

The thermal analysis shows that the induced current which flows from the metallic lead inside the dielectric domain produces high temperature increases around the tip. These results are obtained assuming no contribution from convection; the expected induced temperature increase inside real biological tissues perfused with blood would thus be much lower, but some considerations could be still valid: the highest heating is obtained for the thinnest wire, where the electromagnetic flux that arises near the implant is more dense than for larger surfaces. As a consequence, the resistive losses inside the dielectric domain are higher, as well as the induced heating. Even if the temperature increases resulting

from the numerical study cannot be immediately related to an actual damage for biological tissues, owing to the very simplicity of the model, the values we found suggest in any case that the heating induced by the RF field on implanted patients needs particular attention and further investigation.
In the numerical model, we used as RF source a combination of plane waves at the typical frequencies clinical MRI scanner (i.e. 64 MHz). However, even if the local SAR values and the temperature increases may vary as a function of the frequency, of implant geometry and position, most of the considerations relating to the SAR evaluation can be reasonably extended to all the RF range.

5.5 Conclusions

In order to evaluate the thermal effects of RF exposure on patients implanted with electrical active devices, it is necessary to refine the actual measure methods. In particular, present standards choose an averaging mass of 10 g of tissue to estimate the localised SAR induced by the RF: it would lead to a significant underestimation of the local SAR of the tissues near the implant. The amount of averaging mass should be chosen as a function of the dimension of the implanted object and of the SAR gradient that is generated around it. At the same time, the averaging volume has to be not too small to be just a single "hot spot", not relevant for the evaluation of potential tissue damage due to RF exposure. A good trade-off could be to choose the averaging mass with dimensions doubled than the thickness of the exposed metallic part of the implant.

References

[1] International Commission on Non-Ionizing Radiation Protection (ICNIRP) 1998 Guidelines for Limiting Exposure to Time-varying Electric, Magnetic, and Electromagnetic Fields (up to 300 GHz*), Health Physics*, **74**: 494-522

[2] Duru F, Luechinger R, Scheidegger MB, Luscher TF, Boesiger P, Candinas R 2001 Pacing in magnetic resonance imaging environment: clinical and technical considerations on compatibility. Eur. Heart. J. Jan; 22(2):113-24

[3] Luechinger R, Duru F, Zeijlemaker VA, Scheidegger MB, Boesiger P, Candinas R. 2002 Pacemaker reed switch behavior in 0.5, 1.5, and 3.0 Tesla magnetic resonance imaging units: are reed switches always closed in strong magnetic fields? *Pacing Clin. Electrophysiol*. **25**:1419–1423.

[4] Martin ET, Coman JA, Shellock FG, Pulling CC, Fair R, Jenkins K 2004 Magnetic resonance imaging and cardiac pacemaker safety at 1.5-Tesla. *J Am Col Cardiol*. **43**(7):1315-24

[5] Kalin R and Stanton MS. Current clinical issues for MRI scanning of pacemaker and defibrillator patients. 2005 *Pacing Clin Electrophysiol.* **28**(4):326-8

[6] Helfer JL, Gray RW, MacDonald SG, Bibens TW: Can pacemakers, neurostimulators, leads, or guide wires be MRI safe? Technological concerns and possible resolutions. Minim Invasive *Ther Allied Technol* 2006, **15**(2):114-20

[7] Baker KB, Tkach JA, Nyenhuis JA, Phillips M, Shellock FG, Gonzalez-Martinez J, Rezai AR 2004 Evaluation of Specific Absorption Rate as a Dosimeter of MRI-Related Implant Heating, *Journal of Magnetic Resonance Imaging* **20** 315–320

[8] Fritsch MH, Mosier KM. MRI compatibility issues in otology 2007 *Curr Opin Otolaryngol Head Neck Surg*. **15**(5):335-4

[9] Nitz WR, Oppelt A, Renz W, Manke C, Lenhart M, Link J 2001 On the Heating of linear conductive structure as Guide Wires and Catheters in Interbentional MRI. *Journal of Magnetic Resonance Imaging* **13** 105-114

[10] Busch M, Vollmann W, Bertsch T, Wetzler R, Bornstedt A, Schnackenburg B, Schnorr J, Kivelitz D, Taupitz M, Grönemeyer D. On the heating of inductively coupled resonators (stents) during MRI examinations 2005 *Magn Reson Med*.**54**(4):775-82

[11] Mattei E, Triventi M, Calcagnini G, Censi F, Kainz W, Mendoza G, Bassen HI, Bartolini P. Complexity of MRI induced heating on metallic leads: experimental measurements of 374 configurations Biomed Eng Online. 2008 Mar 3;**7**:11

[12] Mattei E, Calcagnini G, Censi F, Triventi M, Bartolini P. Numerical FDTD models of electromagnetic field generated by the RF coil of a MRI scanner: comparison among different solutions. *Proceedings of the Sixth IASTED International Conference*, Biomedical Engineering, Innsbruck, Austria 2008, ISBN Hardcopy: 978-0-88986-721-5/CD 978-0-88986-722-2

[13] ANSI/AAMI PC69:2000 Active implantable medical devices – Electromagnetic compatibility – EMC test protocols for implantable cardiac pacemakers and implantable cardioverter defibrillators American National Standard

[14] Bassen H, Kainz W, Mendoza G, Kellom T 2006 MRI-induced heating of selected thin wire metallic implants-- laboratory and computational studies-- findings and new questions raised. *Minim Invasive Ther Allied Technol*. **15**(2):76-84

[15] C95.3-2003: Recommended Practice for Measurements and Computations with Respect to Human Exposure to RadioFrequency Electromagnetic Fields, 100 kHz to 300 GHz, 2003 *Institute of Electrical and Electronics Engineers (EEEI)*

[16] Balzano Q, Garay O, Steel FR 1978 Heating of biological tissue in the induction field of VHF portable radio transmitters IEEE *Trans. on Vehicular Technology* VT-**27** (2): 51-56

[17] Chatterjee I, Yong-Gong G, Gandhi OP 1985 Quantification of electromagnetic fields in humans from body-mounted communication receivers, *IEEE Transactions Vehicular Technology* VT-**34** (2): 55-62

[18] Cleveland RF, Athey TW 1989 Specific absorption rate (SAR) in models of the human head exposed to hans-held UHF portable radios, *Bioelectromagnetics* **10**: 173-186

[19] Kuster N, Balzano Q 1992 Energy absorption mechanisms by biological bodies in the near field of dipole antennas, IEEE *Trans. on Vehicular Technology* VT-**41**: 17-23

[20] Saunders RD, Kowalczuk CI, Sienkiewicz ZJ 1991 Biological effects of exposure to non-ionising electromagnetic fields and radiation, III. Radiofrequency and microwave radiation, *Chilton*, NRPB-R240 (London, HMSO)

[21] Scott J 1988 A finite element model of heat transport in the human eye *Phys. Med. Biol*. **33**: 227-41

Chapter 6

A study of the interaction between implanted pacemakers and the radio-frequency field produced by magnetic resonance imaging apparatus

S Pisa[1], G Calcagnini[2], M Caravagno[1], E Piuzzi[1], E Mattei[2], and P Bernardi[1]

[1] Department of Electronic Engineering, Sapienza University of Rome, Italy
[2] Department of Technologies and Health, Italian National Institute of Health, Roma, Italy

Published on IEEE Transactions On Electromagnetic Compatibility, Vol. 50, No. 1, February 2008

Abstract

Specific absorption rate (SAR) and temperature increases produced inside a thorax model by an MRI apparatus equipped with a birdcage antenna operating at 64 MHz have been studied both experimentally and numerically. Considering a pacemaker(PM) equipped with a unipolar catheter inserted inside the thorax model, peak SARs averaged over 1 mg between 240 and6400 W/kg, depending on the catheter section and length, on its position inside the phantom, and on field polarization have been obtained close to the catheter tip. On the other hand, the average SAR in the whole thorax is not influenced by the presence of the PM. Temperature increments from 0.6 ◦C to 15 ◦C have been obtained for 6-min MRI investigations with the lowest values when the radio-frequency (RF) magnetic field is linearly polarized along a direction perpendicular to the implant plane.

Index Terms*—Cardiac pacemakers, dosimetry, magnetic resonance imaging (MRI), temperature.*

6.1 Introduction

Magnetic resonance imaging (MRI) is a tomography technique that measures the radio-frequency (RF) field produced by the magnetic moments of hydrogen nuclei during their precession following the application of RF pulses superimposed to a static magnetic field.MRI is a widely accepted tool for the diagnosis of a variety of diseases. Nowadays, however, MRI is contraindicated for patients implanted with pacemakers (PMs) and implantable cardioverter defibrillators (ICDs) [1]–[3]. Potential effects of MRI on PMs, ICDs, and other active implantable medical devices include force and torque effects on the PM [4], undefined reed-switch state [5], and potential risk of heart stimulation and inappropriate pacing [6]. However, the most adverse effect seems to be the heating of the heart tissue around the catheter tip produced by the high currents induced on the catheter by the RF field used in MRI technique [7]–[10]. The amount of heating has been investigated in several studies on phantoms, and observed temperature elevations spread from not significant values up to tens of degrees. For example, Achenbach et al. [7] reported a temperature increase of 63.1 ◦C for a particular PM lead, Sommer et al. [8] obtained temperature increase ranging from0.1 ◦C to 23.5 ◦C, depending on the electrode type, while in [9]and [10], a maximum temperature increase of about 6 ◦C has been found. In order to avoid thermal hazards, international agencies have issued guidelines reporting recommended limits. The International Commission on Non-Ionizing Radiation Protection(ICNIRP) [11] considers that, for whole-body exposures to MRI apparatus, no adverse health effects are expected if the increase in body core temperature does not exceed 1 ◦C. With regard to localized heating, ICNIRP assumes that adverse effects are avoided with a reasonable certainty if temperature remains lower than 38 ◦C in localized regions of the head, lower than 39 ◦C in the trunk, and less than 40 ◦C in the limbs. Consequently, in [11], limitations have been reported with reference to whole body Specific absorption rate (SAR) (SAR_{WB}) and

local SAR as averaged over 10 g of tissue (SAR10). In particular, in normal conditions, the SAR_{WB} should not exceed 2 W/kg, whileSAR10 is limited to 20 W/kg in the extremities and 10 W/kg in the head and trunk; however, care should be taken to ensure that the temperature rise is limited to 1 ◦C in the eye. It must be noted that the temperatures considered safe in [11]are very conservative with reference to the heart. In fact, literature data on cardiac ablation indicate the development of abnormal automaticity and irreversible loss of cellular excitability of cardiac tissue for temperatures greater than 45 ◦C and 50 ◦C, respectively [12].The thermal studies available in the literature[7]–[10] evidence, as previously discussed, strong variations in temperature at the catheter tip in PM holders during MRI. The steady-state temperatures are often above ICNIRP recommended limits, and in some cases, above the threshold for the loss of cellular excitability [12]. The reported variability in peak temperatures can be ascribed to the differences in power radiated by the MRI antenna, the length and the geometric structure of the lead, and the implant location. Consequently, an accurate analysis of the coupling between the RF field and the catheter appears to be very important. In this paper, the power absorption and the temperature elevations induced by an MRI apparatus in a homogeneous thorax model, where a PM with a monopolar catheter is implanted, will be studied both experimentally and numerically. In particular, the effect of field polarization and the influence of the catheter geometry and radius on SAR and temperature increments will be analyzed.

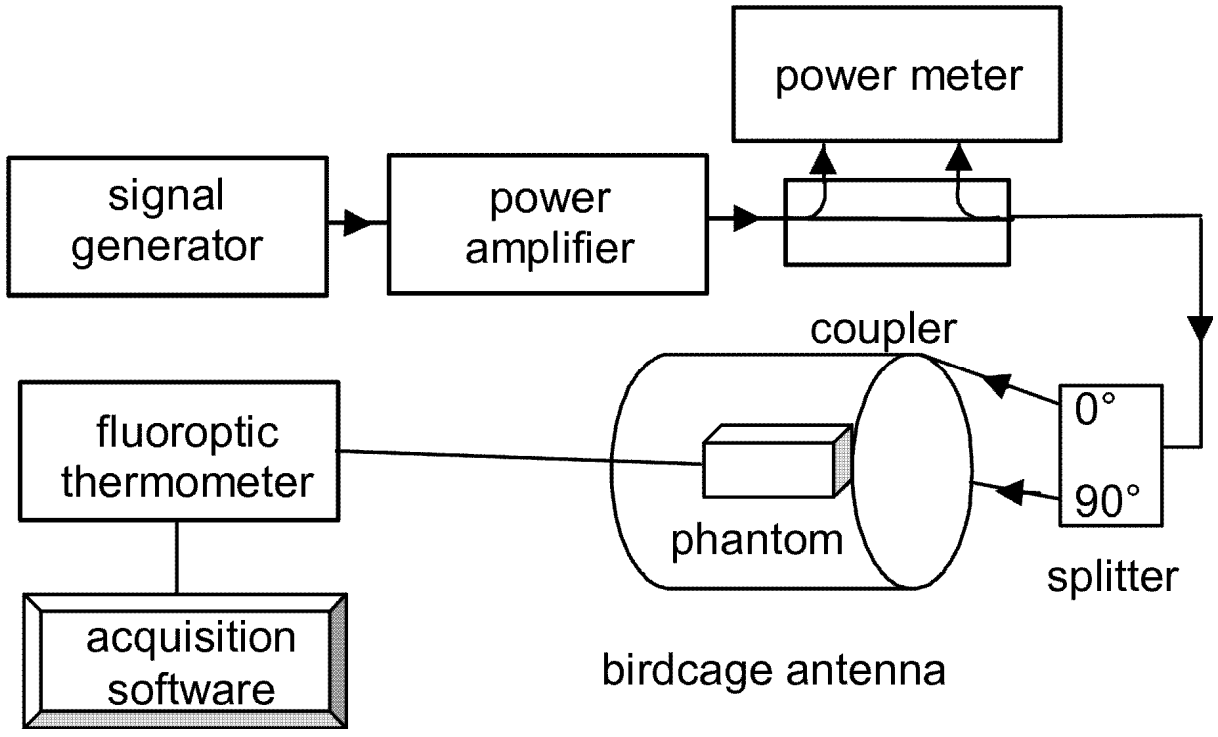

Figure 1. Experimental setup.

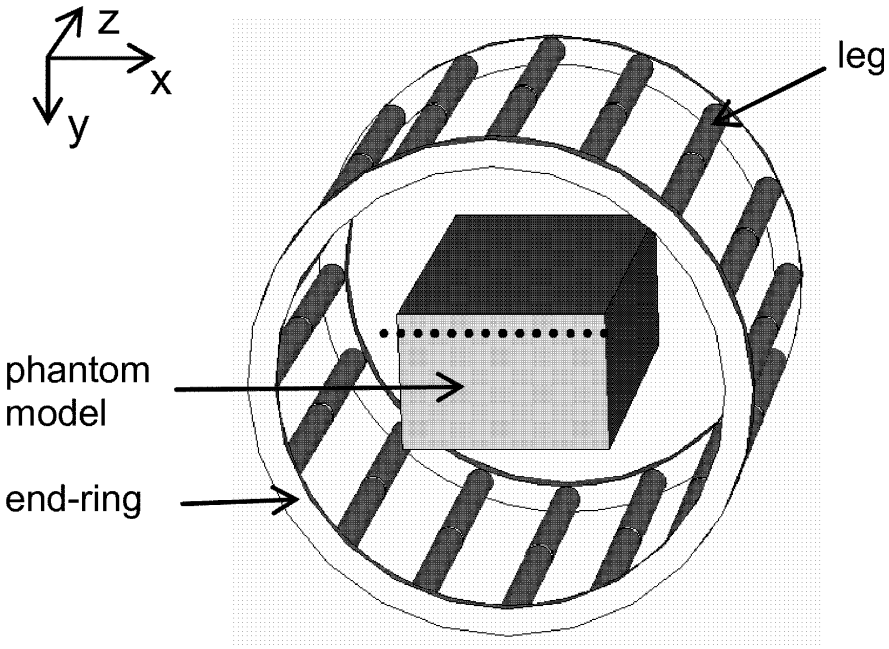

Figure 2. Phantom model placed inside the birdcage antenna.

6.2 Methods

6.2.1 Experimental Setup

Experimental data have been provided by the Italian National Institute of Health. Fig. 1 shows the experimental setup. The64-MHz signal is first amplified, and then, sent to the birdcage antenna through a power splitter with 90◦ output shift. The applied RF power is monitored with a power meter. The birdcage has an internal diameter of 62 cm, a height of 65 cm, and16 legs (see Fig. 2).The physical phantom is a parallelepiped box (30 cm × 20 cm × 60 cm) filled with gelled saline material (HEC 2%,NaCl 0.36%) that mimics the electrical and thermal properties of an average human tissue at the considered frequency [13].The measured permittivity and conductivity values of the gelled material are equal to 78.2 and 0.6 S/m, respectively [14]. A tissue density (ρ) of 1006 kg/m3 , together with a thermal conductivity(K) equal to 0.2 W/(m ·◦ C) and a specific heat (C)of 4178 J/(kg · ◦C) have been provided by the HEC manufacturer[15].A unipolar PM with a 60-cm-long catheter (see Fig. 3), which represents the usual length for commercial catheters, is fixed to a plastic grid and immersed in the phantom at a depth of 1 cm inside the saline material. Temperature increments are monitored via a four-probe Luxtron3100 fluoroptic® TM thermometer equipped with SMM probes accurate to 0.1 ◦C at the point of calibration (21 ◦C in our case). SAR (in watts per kilogram) values are extrapolated from initial temperature rise rate through the equation

$$SAR = C\frac{dT}{dt}|_{t=0} \quad (1)$$

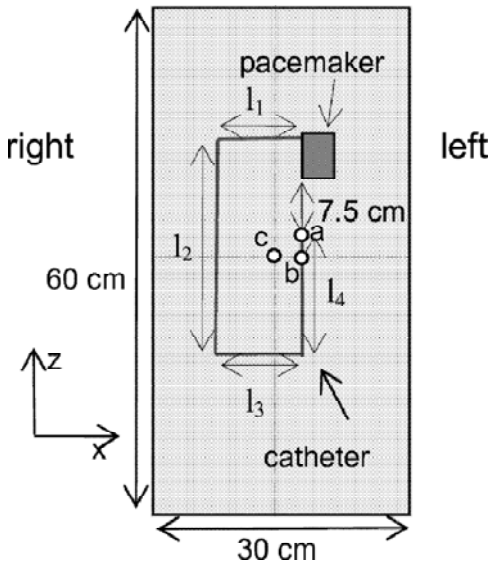

Figure 3. Section of the phantom model 1 cm below the phantom surface (dotted line in Fig. 2) showing the geometry of PM and catheter.

In order to reduce the thermal diffusion influence on SAR determination, he temperature variation is computed between 3 and10 s from the beginning of the exposure.

6.2.2 Electromagnetic Model

Numerical simulations have been performed using a code based on a conformal finite-difference time-domain (FDTD) scheme [16] with graded mesh (C-GM-FDTD) [17], [18]. The investigated region has been divided in cells of variable size, from 1 to 10 mm (with the smaller cells in the catheter region),and the different structures (metallic birdcage, dielectric phantom, and metallic PM and catheter) have been modeled, assigning to each cell an equivalent permittivity and conductivity evaluated as the weighted fraction of the materials contained in the cell, according to the conformal scheme described in [16]. The FDTD domain has been closed with uniaxial perfectly matched layer (UPML) boundary conditions (four cells, 0.01% reflection, parabolic profile) [19]. A current excitation with sinusoidal time behavior has been imposed at the center of the birdcage legs. A phase delay equal to the azimuthal angle, corresponding to an increasing 22.5° phase shift between elements, has been applied to produce a left circular magnetic polarization with respect to the positive z-axis. This polarization is necessary for having the maximum coupling between the RF field and the nuclear proton spin [20].Linear polarizations can also be applied with a birdcage antenna. These are simulated by imposing current excitations with the same phase but with amplitudes varying cosinusoidally or sinusoidally with the azimuthal angle in order to obtain a y directed or an x-directed magnetic field linear polarization, respectively [21]. However, it must be noted that a linear polarization can be divided in the sum of a left and a right circular polarization. Hence, to achieve, in this case, a circularly polarized magnetic field component having a magnitude equal to that obtained for the previously considered excitation, the power to be sent to the birdcage should be doubled [21]. Once the steady-state conditions are reached and the amplitude of the

three electric field components are determined in the center of each cell inside the phanthom, the SAR is evaluated as

$$SAR(i,j,k)=\frac{\sigma(i,j,k)\left[E_x^2(i,j,k)+E_y^2(i,j,k)+E_z^2(i,j,k)\right]}{2\rho(i,j,k)} \quad (2)$$

where σ(i,j,k) and ρ(i,j,k) are the conductivity and density of the tissue filling the (i,j,k) cell. The considered values are the SAR averaged over 1 mg (≈ 1 mm^3) which is the quantity usually measured in experimental studies, its peak value inside the thorax (SAR_{PEAK}), and the average over the whole thorax (SAR_{WB}) which quantifies the total power absorption.

6.2.3 Thermal model

The temperature distribution T = T(**r**,t) has been simulated by solving Fourier's heat transfer equation (FHE) [22] inside the phantom:

$$\nabla\cdot\left(K(\mathbf{r})\,\nabla T\right)+Q_v(\mathbf{r})=C(\mathbf{r})\,\rho(\mathbf{r})\,\frac{\partial T}{\partial t} \quad [\mathrm{W/m^3}] \quad (3)$$

The two terms on the left side of (3) represent the heat transfer through internal conduction, and the electromagnetic power deposition (Q_v [W/m^3]). These terms are equated with the temperature increase (or decrease) per unit time multiplied by the thermal capacitance of 1 m^3 of tissue (right side). The thermal capacitance is given by the product between the tissue specific heat and the density. The above described FHE, in order to be solved, must be completed by an appropriate boundary condition, able to model heat exchange from the phantom surface to the external environment. This boundary condition is obtained by imposing the continuity of the heat flow perpendicular to the phantom surface, and can be expressed as [22]:

$$-K(\mathbf{r})\left(\nabla T\cdot\boldsymbol{n_0}\right)_S=H\left(T_S-T_A\right) \quad [\mathrm{W/m^2}] \quad (4)$$

where S is the phantom surface, and n_0 is the unit vector normal to S. The term on the right side of (4) models heat losses due to convection and radiation, proportional to the difference between temperature of the phantom surface (T_S) and external temperature (T_A) through the parameter H [$W/(m^2{\circ}C)$]. A convection coefficient equal to 10 $W/(m^2\,°C)$ and an external temperature T_A equal to 21 °C have been assumed in all the simulations. To obtain a finite-difference formulation of the FHE and boundary condition, the phantom is divided in cubic cells of 1 mm side, and the temperature is evaluated in a grid of points defined at the centers of the cells. The equation (3) is then solved by using an alternate direction implicit finite difference (ADI-FD) formulation [23].

6.3 Results

6.3.1 Thorax Exposure Without the Pacemaker

At first, the exposure of the thorax phantom without the pacemaker has been studied both experimentally and numerically.

During the experiments, the birdcage antenna operates at 64 MHz with a radiated power of 100 W that is close to the average power delivered by MRI apparatus during a typical sequence for imaging acquisition. Calorimetric measurements performed on the exposed phantom revealed that the SAR_{WB} is equal to about 1 W/kg.

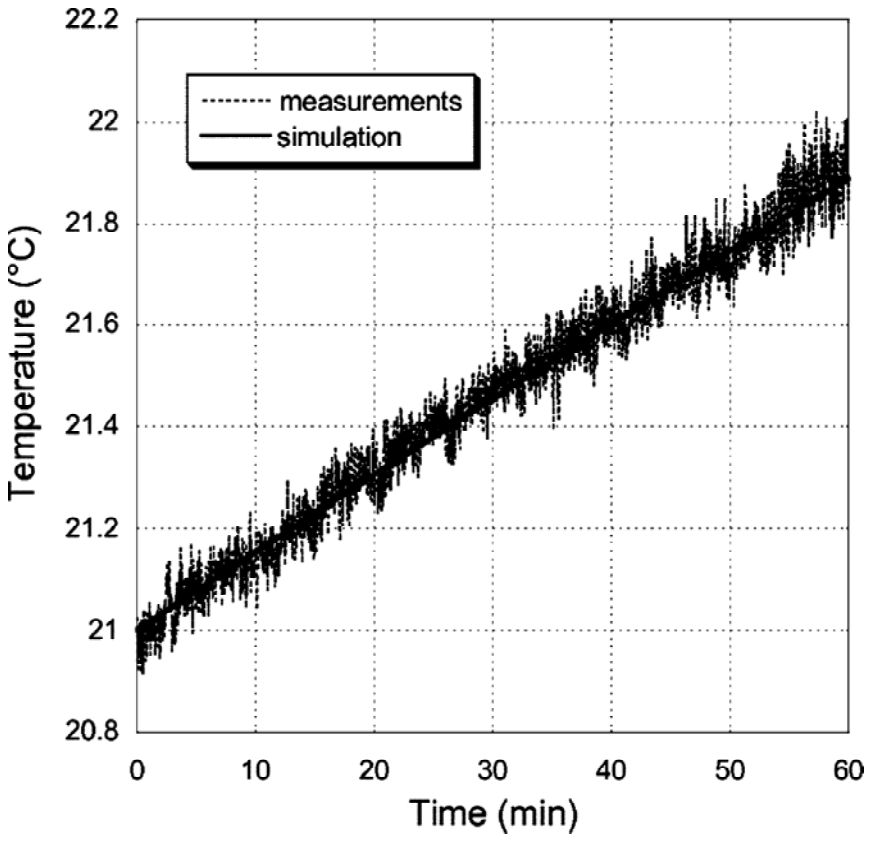

Figure 4. Time behavior of the temperature in the physical and simulated phantoms (without PM) evaluated at point "c" in Fig. 3.

The same exposure has been simulated by using the C-GM-FDTD code for the solution of the EM problem and the ADI-FD code for the solution of Fourier's equation. Due to the differences between the birdcage field excitation in the experimental setup and in the numerical simulations, and in order to compare the results, the current excitation amplitudes in simulations have been chosen to give rise in the thorax model to a SAR_{WB} of 1 W/kg equal to the experimental data. The considered current excitation produces, in the absence of the thorax, magnetic field magnitudes of about 2.5 A/m in the birdcage central

region, that are close to the typical mean field value adopted in the fast spin echo sequences used in MRI [20].

Fig. 4 shows the measured (continuous line) and simulated (dashed line) temperature in the phantom in a point 1 cm below the phantom surface (point c in Fig. 3). A temperature increase of about 0.9 °C after 60 minutes of exposure can be observed. The linear behavior is due to the fact that for the considered problem, and by considering a penetration depth (□) of 0.1 m, a time constant equal to □ = C□ □2/K □ 3000 min is expected [24].

The performed numerical simulation allows us to analyze the field and SAR distributions inside the phantom. Fig. 5(a) shows the obtained electric field z-component on a coronal plane (x-z in Fig. 2) 1 cm below the thorax surface (corresponding to the dotted line section of Fig. 2 where the PM and the catheter will be placed). The figure shows that the induced electric field presents a z-component with the highest values close to the left and right box faces. The electric field x-component (not shown) has lower values (< 30 V/m) with maxima close to the top and bottom faces. Finally, the electric field y-component (not shown) is always lower than 10 V/m.

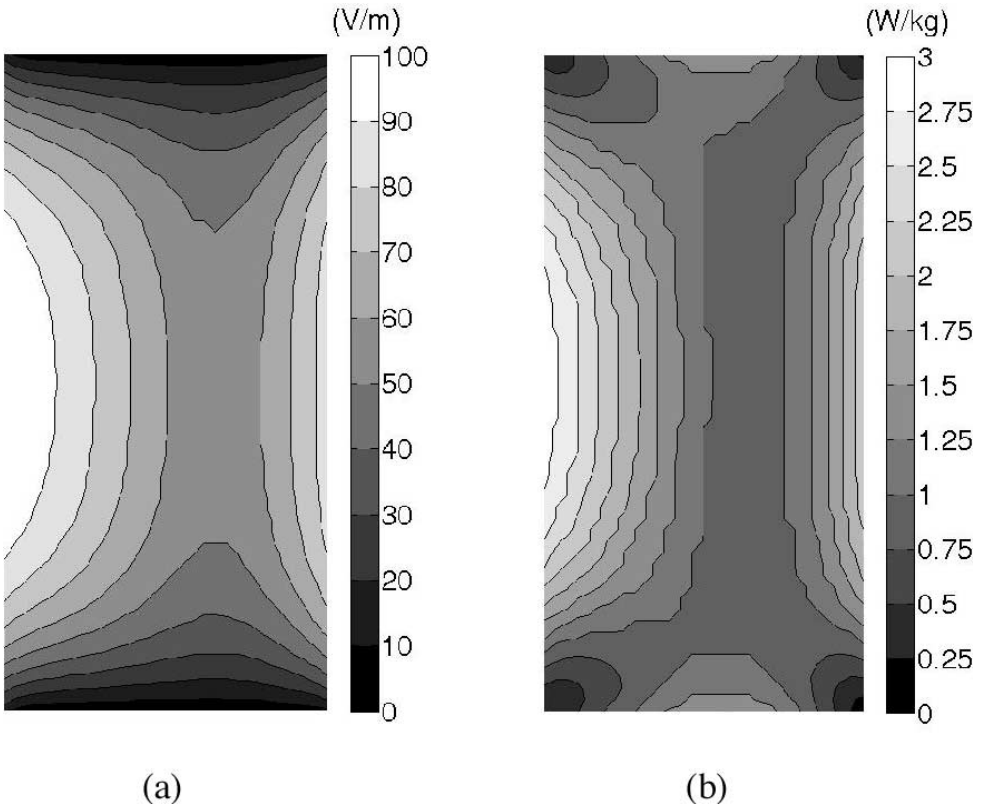

Fig. 5. (a) E_z field distribution on a coronal plane (*x–z* in Fig. 2) 1 cm below the phantom surface for a left circular polarization. (b) SAR distribution on the same section.

The SAR distribution is shown in Fig. 5(b) for the same coronal plane of Fig. 5(a). From the figure it can be noted that this distribution is very similar to that of the electric field z-component, reported in Fig. 5(a). In fact, this is the strongest electric field component and the thorax model is homogeneous. Under

these conditions, a SAR_{PEAK} of 3.1 W/kg has been computed, and, as stated before, the SAR_{WB} is equal to 1.0 W/kg. It is worth noting that both the SAR and field distribution do not show horizontal symmetry. In fact, while the structure is symmetric, the field excitation presents an azimuthal phase shift that gives rise to higher values on the right side of the phantom model.

The same structure has been studied by applying x-directed and y-directed magnetic field linear polarizations. Fig. 6 shows the obtained SAR distributions in the same plane of Fig. 5 with a current excitation settled to achieve a SAR_{WB} of 1 W/kg. Both the x-directed [see Fig. 6(a)] and the y-directed [see Fig. 6(b)] linear polarizations give rise to a symmetric distribution, with respect to the x and z axes, and to a SAR_{PEAK} of about 2.7 W/kg slightly lower with respect to the circular polarization case. However, as discussed in Section II.B, the power to be sent to the birdcage must be doubled, thus doubling SAR values [20]. The electric field simulation results (not reported) show that, as for the circular polarization case, the SAR distribution for linear polarization follows quite well that of the electric field z-component.

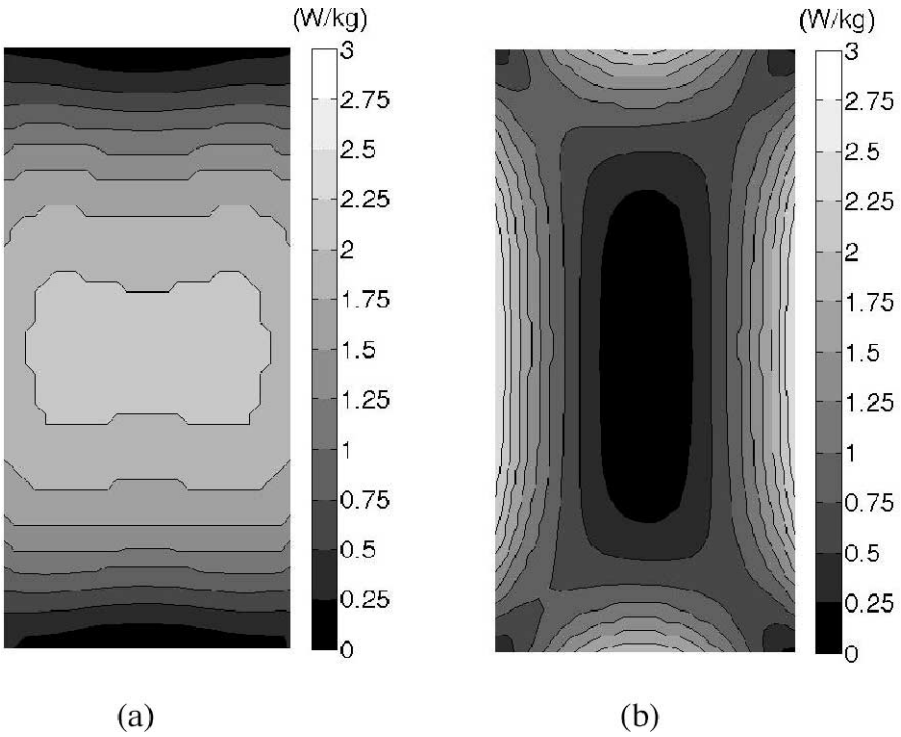

Fig. 6. SAR distribution in the coronal section, 1 cm below the phantom surface, for x-directed (a) and y-directed (b) magnetic field linear polarizations.

6.3.2 Effect of the Pacemaker Geometry and Position

The exposure to a power of 100 W at 64 MHz of the thorax model in the presence of a pacemaker with a unipolar catheter has then been studied both experimentally and numerically.

In the experiments, a commercial PM with a 60-cm long catheter (l1 = 10 cm, l2 = 26 cm, l3 = 10 cm, l4 = 14 cm in Fig. 3) has been placed inside the thorax. The PM is located in the left side in a typical operating position with the catheter tip 7.5 cm from the pacemaker.

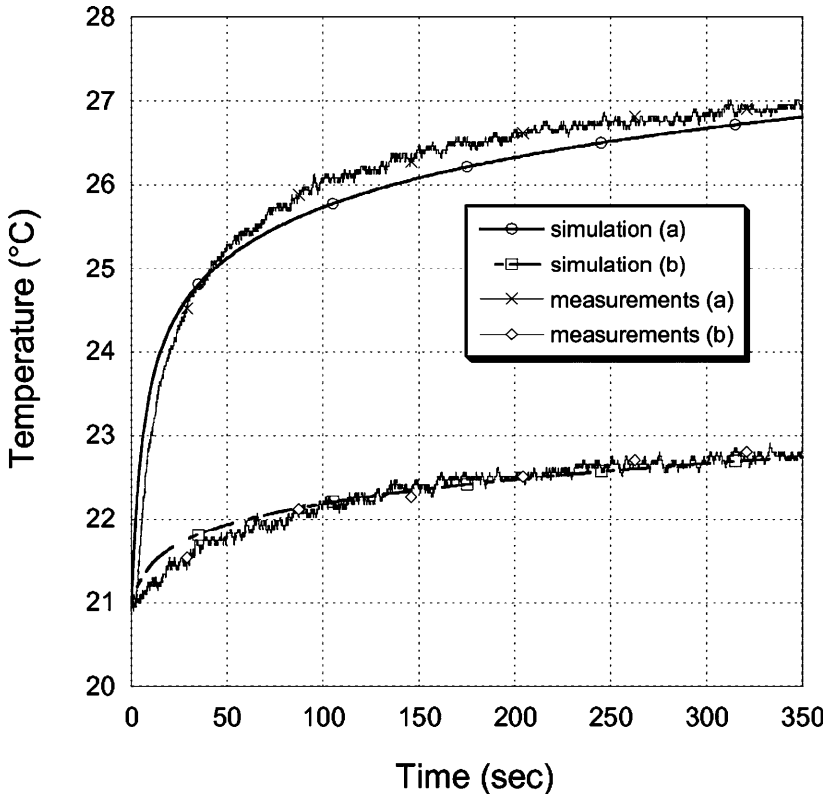

Figure. 7. Time behavior of the temperature on the physical and simulated phantoms (with PM) at the catheter tip (point 'a' in Fig. 3) and 2 cm below the catheter tip (point 'b' in Fig. 3)

The same exposure has been simulated by using the C-GM-FDTD code for the solution of the EM problem and the ADI-FD code for the solution of Fourier's equation. In the EM simulations the PM has been modeled as a copper box (40x10x50 mm3) and the 60-cm long catheter has been modeled has a cylindrical wire of copper with a radius of 0.4 mm with the same rectangular geometry considered in the experiments (see Fig. 3). The same birdcage current excitation applied in the absence of the PM has been adopted.

Fig. 7 shows the time behavior of the measured and simulated temperature. After 6-min exposure, a temperature increment of 6 °C at a point just above the catheter tip (a in Fig. 2) and 1.8 °C at a point 2 cm below the catheter tip (b in Fig. 2), can be observed, with a good agreement between measurements and simulations.

Further numerical simulations have been performed in order to analyze the SAR distributions inside the phantom and the currents along the catheter for circular and linear excitations.

Fig. 8 shows the obtained SAR distributions in the coronal section passing through the catheter. Note that the gray scale is strongly saturated; in fact, the presence of the catheter determines high local SAR values. SAR_{PEAK} of 2400 W/kg, 6400 W/kg, and 250 W/kg have been obtained at the catheter tip for the circular, x-directed and y-directed linear polarizations, respectively. The SAR_{WB} is about 1.0 W/kg in all cases.

Temperature simulations showed temperature increments at the catheter tip of 6 °C, 15 °C and 0.6 °C after 6 min of exposure, for the three considered cases.

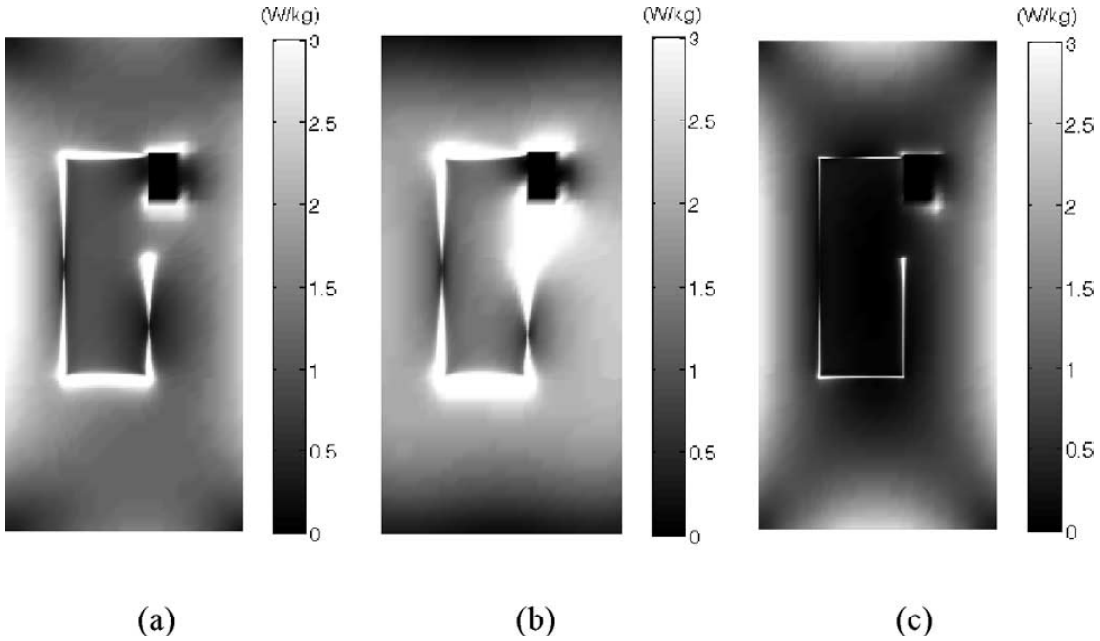

Figure. 8. SAR distributions in the coronal section passing through the catheter (see Fig. 2). (a) left-circular polarization, (b) linear x-directed, (c) linear y-directed polarizations.

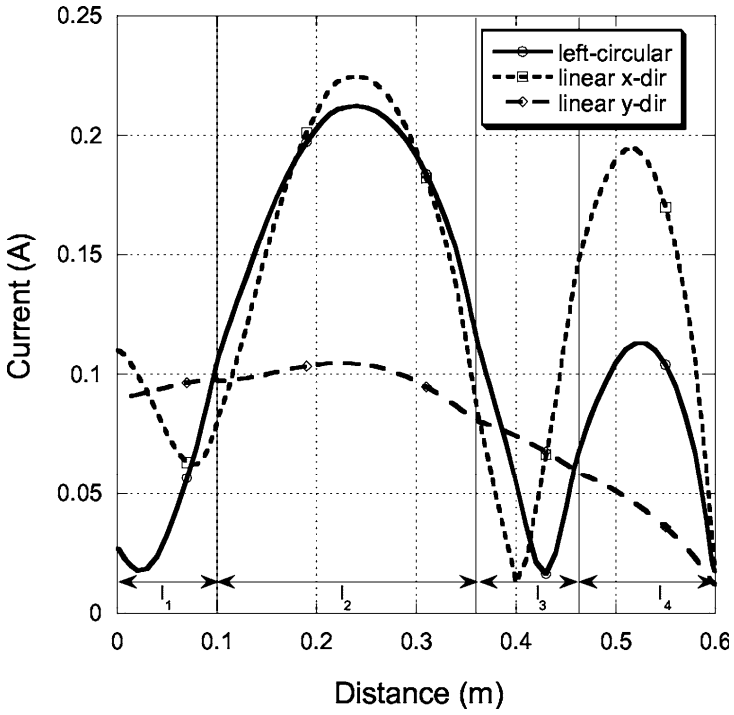

Figure. 9. Current distribution along the catheter for clockwise and linear excitations (pacemaker on the left of the thorax).

The current distribution along the catheter has been computed as the circulation of the magnetic field around the catheter axis. Fig. 9 shows the current distributions obtained for the three considered cases. The distance along the wire from the point in which the catheter is inserted in the pacemaker is reported on the horizontal axis (the catheter length is 60 cm). The obtained current distributions can be explained observing that at 64 MHz and in the presence of the dielectric phantom the wavelength is about 50 cm and hence comparable with the catheter length. Moreover, in quasi static conditions, the current inside the wire is mainly produced by the electric field component, obtained in the absence of the wire (unperturbed field), parallel to the wire axis. Correspondingly, in the considered exposure condition the strongest currents are produced by the E_z field along the l2 and l4 segments while lower currents are produced by the lower E_x component, acting on l1 and l3.

The comparison between the SAR distributions reported in Fig. 8 and the current distributions in Fig. 9 evidences that the current along the wire follows an opposite behavior with respect to the SAR distribution around the wire. In fact, the presence of the wire strongly alters the field distribution as compared to the one obtained without the catheter. Therefore, the SAR (and hence the electric field) decreases close to the wire section where the current grows and vice versa. For example the current presents a maximum at the centre of the l2 and l4 segments where the SAR has a minimum [darker regions in Fig. 8(a)].

A further study has been performed in order to investigate the effect of the catheter cross-section on SAR. To this end, two more wires, of radius 0.2 and 0.8 mm, respectively, have been considered. The simulation results, for a circularly polarized magnetic field, have evidenced that the SAR values at the catheter tip increase when the wire section reduces. SAR_{PEAK} values of 2500 and 760 W/kg have been obtained for wire radius of 0.2 and 0.8 mm, respectively. It is worth noting that the increase of the wire radius determines an increase of the current along the wire and at the tip. However, the corresponding increase of the section produces a reduction of the current density and hence the final effect is a reduction of the SAR at the catheter tip.

The effect of the catheter length has been also investigated by considering catheters with a 0.4-mm radius and different lengths. In the considered simulations the distance between the catheter tip and the pacemaker has been maintained equal to 7.5 cm while the length of the catheter has been changed. Fig. 10 shows the results obtained for a total length of 32 cm (l1 = 7 cm, l2 = 15 cm, l3 = 7 cm, l4 = 3 cm) and for a total length of 44 cm (l1 = 10 cm, l2 = 18 cm, l3 = 10 cm, l4 = 6 cm). In these simulations SAR_{PEAK} of 1000 and 1400 W/kg have been obtained for the two considered lengths.

In the previous analysis the pacemaker was implanted in the left part of the thorax, however in clinical practice the pacemaker can be also implanted on the right part of the thorax. Numerical simulations have been performed in order to study this exposure condition and by considering both circular and linear polarizations. Fig. 11 shows, for the circular polarization case, the SAR distribution in the coronal section passing through the catheter.

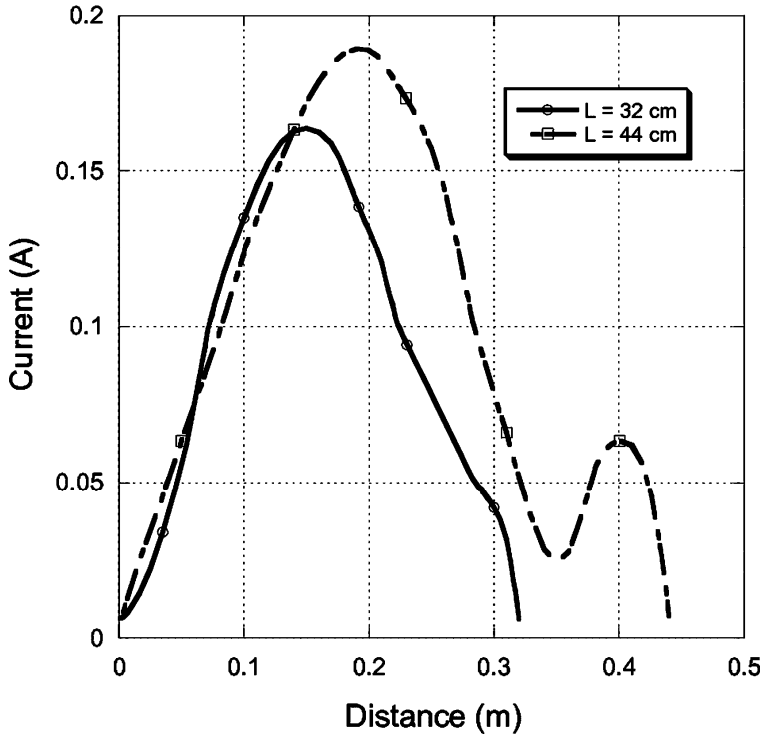

Figure 10. Current distribution along the catheter for clockwise excitations and catheters of different lengths.

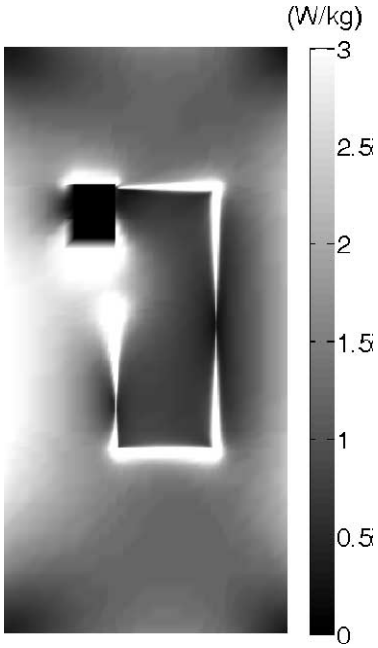

Figure 11. SAR distribution in the coronal section passing through the catheter (see Fig. 2) for left-circular polarization. Catheter in the right part of the thorax.

In the previous analysis the pacemaker was implanted in the left part of the thorax, however in clinical practice the pacemaker can be also implanted on the right part of the thorax. Numerical simulations have been performed in order to study this exposure condition and by considering both circular and linear

polarizations. Fig. 11 shows, for the circular polarization case, the SAR distribution in the coronal section passing through the catheter. The SAR_{PEAK} is always localized at the catheter tip and a value of about 4500 W/kg has been obtained. Moreover SAR_{PEAK} values of 6400 and 240 W/kg have been obtained for the linear x-directed and y-directed polarizations, respectively. These last values are practically identical to those obtained for the left PM placement while in the circular polarization case higher values are obtained with respect to the left placement. This is due to the asymmetry of the E_z field distribution [see Fig 5(a)] with highest field values on the right part of the thorax where the catheter tip is placed in this last exposure condition.

6.4 Conclusions

The SAR induced by an MRI apparatus in a thorax model with an implanted pacemaker equipped with a monopolar catheter has been studied considering different implant geometries and field polarizations.
The study has been limited only to a simple homogeneous phantom because the main aim was to compare numerical results with experimental measurements in order to validate the proposed numerical methodology and to study the effect of catheter geometry and field polarization.
The performed study has evidenced that:

- The region with the highest SAR values is the one around the catheter tip where the current flowing along the catheter wire can induce strong current densities in the tissues.
- The currents along the catheter are mainly induced by the electric field parallel to the catheter axis. Since strong E-field z-components are present, the highest currents are induced along vertical wires.
- Generally, short catheters with short vertical wires give rise to lower SAR at the catheter tip. However the lowest SAR_{PEAK} values have been obtained when the magnetic field is linearly polarized on a direction perpendicular to the implant plane (y direction in Fig. 3).
- The SAR_{PEAK} values obtained for the considered exposure condition give rise to temperature increments at the catheter tip ranging between 0.5 and 15 °C.

It is important to remember that, on the basis of ICNIRP recommendation, no adverse health effects are expected if the temperature in localized parts of the trunk does not exceed 39 °C [11]. On the basis of the present study these limits can be reached for a pacemaker located in a simple homogeneous parallelepiped phantom. However, reductions in peak temperatures are expected if an anatomical body model with a catheter following the vein path is considered together with the presence of blood perfusion and thermoregulation. In fact the insertion of the PM in an anatomical model brings part of the catheter to be placed more deeply inside the body in regions with lower electric fields, and the presence of perfusion and thermoregulation surely reduces the temperature increment also if the percentage of reduction is not predictable due to the complexity of the problem (geometry, thermal parameters etc.). The adopted

techniques, with the inclusion of blood perfusion and thermoregulation in the thermal model [25], will be applied to anatomically accurate body phantoms (e.g. Visible Human [26]) in a future work. Consideration of this anatomical model will make it possible to investigate if, under realistic conditions, the use of particular field polarizations, implant arrangements or any design technique able to reduce the current along the wire can prevent temperature increases from exceeding the levels considered safe by ICNIRP thus allowing MRI to pacemaker holders.

References

[1] J. R. Gimbel and E. Kanal, "Can patients with implantable pacemakers safely undergo magnetic resonance imaging?," *J. Am. Coll. Cardiol.*, vol. 43, no. 7, pp. 1325-1327, Apr. 2004

[2] E. Kanal and F. G. Shellock, "Policies, guidelines, and recommendations for MR imaging safety and patient management. SMRI Safety Committee," *J. Magn. Reson. Imaging*, vol. 2, no. 2, pp. 247-248, Mar.-Apr. 1992

[3] F. G. Shellock, "Magnetic resonance: health effects and safety," Boca Raton, FL: CRC Press, 2001

[4] R. Luechinger, F. Duru, M. B. Scheidegger, P. Boesiger, and R. Candinas, "Force and torque effects of a 1.5-tesla MRI scanner on cardiac pacemakers and ICDs," *Pacing Clin. Electrophysiol.*, vol. 24, no. 2, pp. 199-205, Feb. 2001

[5] R. Luechinger, F. Duru, V. A. Zeijlemaker, M. B. Scheidegger, P. Boesiger, and R. Candinas, "Pacemaker reed switch behavior in 0.5, 1.5, and 3.0 tesla magnetic resonance imaging units: are reed switches always closed in strong magnetic fields?," *Pacing Clin. Electrophysiol*, vol. 25, no. 10, pp. 1419-1423, Oct. 2002

[6] J. A. Erlebacher, P. T. Cahill, F. Pannizzo, and R. J. Knowles, "Effect of magnetic resonance imaging on DDD pacemakers, " *Am. J. Cardiol.,* vol. 57, no. 6, pp. 437-440, Feb. 1986

[7] S. Achenbach, B. Moshage, W. Diem, T. Bieberle, V. Schibgilla, and K. Bachmann, "Effects of magnetic resonance imaging on cardiac pacemakers and electrodes," *Am. Heart. J.,* vol. 134, no. 3, pp. 467-473, Sep. 1997

[8] T. Sommer, C. Vahlhaus, G. Lauck, A. von Smekal, M. Reinke, U. Hofer, W. Bloch, F. Traber, C. Schneider, J. Gieseke, W. Jung, and H. Schild, "MR imaging and cardiac pacemaker: in-vitro evaluation and in-vivo studies in 51 patients at 0.5 T," *Radiology*, vol. 215, no. 3, pp. 869-879, June 2000

[9] A. Roguin, M. M. Zviman, G. R. Meininger, E. R. Rodrigues, T. M. Dickfeld, D. A. Bluemke, A. Lardo, R. D. Berger, H. Calkins, and H. R. Halperin, "Modern pacemaker and implantable cardioverter/defibrillator systems can be magnetic resonance imaging safe. In vitro and in vivo assessment of safety and function at 1.5 T," *Circulation*, vol. 110, no. 5, pp. 475-482, May 2004

[10] S. Pisa, G. Calcagnini, M. Cavagnaro, E. Piuzzi, M. Triventi, and P. Bernardi, "SAR and temperature elevations in pacemaker holders exposed to EM fields produced by MRI apparatus," in 2006 *IEEE MTT-S International Microwave Symposium Digest*, San Francisco, pp. 1754-1757, June 2006

[11] ICNIRP Statement on: "Medical magnetic resonance (MR) procedures: protection of patients," *Health Phys.*, vol. 87 no. 2, pp. 197-216, Aug. 2004

[12] S. Nath, C. Lynch, J. G. Whayne, and D. E. Haines, "Cellular electrophysiological effects of hyperthermia on isolated guinea pig papillary muscle implications for catheter ablation," *Circulation*, vol. 88, pp. 1826–1831, Oct. 1993

[13] ASTM Designation: F 2182 – 02a "Standard Test Method for Measurement of Radio Frequency Induced Heating Near Passive Implants During Magnetic Resonance Imaging," 2002

[14] T. W. Athey, M. A. Stuckly and S. S. Stuckly, "Measurement of RF permittivity of biological tissues with an open-ended coaxial line: part I," IEEE Trans. Micowave Theory Tech, MTT-30, 1982, pp. 82-86

[15] "Natrosol hydroxyethylcellulose: A nonionic water soluble polymer, physical and chemical properties," Aqualon, Hercules Inc., Wilmington, DE

[16] D. Caratelli and R. Cicchetti, “A full-wave analysis of interdigital capacitor for planar integrated circuits,” *IEEE Trans. Magn.*, vol. 39, no. 3, pp. 1598-1601, May 2003

[17] M. Yang and Y. Chen, “Automesh: an automatically adjustable, non-uniform, orthogonal FDTD mesh generator,” *IEEE Antennas Propagat. Mag.*, vol. 41, no. 2, pp. 13-19, Apr. 1999

[18] S. Pisa, M. Cavagnaro, E. Piuzzi, and V. Lopresto, “Numerical-experimental validation of a GM-FDTD code for the study of cellular phones,” *Microwave Opt. Technol. Lett.*, vol. 47, no. 4, pp. 396-400, Nov. 2005

[19] A. Taflove and S. C. Hagness, *Computational Electrodynamics: The Finite-Difference Time-Domain Method*. Boston, MA: Artech House, 2000

[20] U. D. Nguyen, S. Brown, I. A. Chang, J. K. Krycia, and M. S. Mirotznik, “Numerical evaluation of heating of the human head due to magnetic resonance imaging”, *IEEE Trans. Biomed. Eng.,* vol. 51, no. 8, pp. 1301-1309, Aug. 2004

[21] C. M. Collins, S. Li, and M. B. Smith, “SAR and B1 field distributions in a heterogeneous human head model within a birdcage coil,” *Magn. Res. Med.*, vol. 40, pp. 847-856, 1998

[22] N. Ozisik, Heat Transfer: a Basic Approach, New York: Mc Graw Hill, 1985.

[23] S. Pisa, M. Cavagnaro, E. Piuzzi, P. Bernardi, and J. C. Lin, “Power density and temperature distributions produced by interstitial arrays of sleeved-slot antennas for hyperthermic cancer therapy,” *IEEE Trans. Microwave Theory Tech*., vol. 51, no. 12, pp. 2418-2426, Dec. 2003

[24] K. R. Foster, A. Lozano-Nieto, and P.R. Riu, “Heating of tissues by microwaves: a model analysis,” *Bioelectromagnetics,* vol. 19, pp. 420-428, 1998

[25] P. Bernardi, M. Cavagnaro, S. Pisa, and E. Piuzzi, “Specific absorption rate and temperature elevation in a subject exposed in the far-field of radio-frequency sources operating in the 10-900 MHz range,” *IEEE Trans. Biomed. Eng.*, vol. 50, no. 3, pp. 295-304, Mar. 2003

[26] P. A. Mason, W. D. Hurt, T. J. Walters, J. A. D’Andrea,P. Gajsek, K. L. Ryan, D. A. Nelson, K. I. Smith, and J.M. Ziriax, “Effects of frequency, permittivity, and voxel sizeon predicted specific absorption rate values in biological tissue during electromagnetic-field exposure,” *IEEE Trans. MicrowaveTheory Tech*., vol. 48, n. 11, pp. 2050-2058, Nov. 2000

Chapter 7

RF induced heating on a pacemaker implant during MRI: numerical model and experimental validation

E Mattei[1], M Triventi1, G Calcagnini[1], F Censi[1], and P Bartolini[1]

[1] Department of Technologies and Health, Italian National Institute of Health, Roma, Italy

Abstract

Magnetic resonance imaging (MRI) may cause harmful tissue heating in patients implanted with pacemakers (PM) or cardioverter/defibrillator. Consequently, these patients are often preventively excluded from any kind of MRI investigations. The scientific community has been studying this issue for several years, in order to identify the elements that are involved in the heat generation process and to eventually define safety conditions and procedures that could allow to extend MRI also to implanted patients. In this field, numerical studies represent very useful tools to extend the range of experimental measurements; in addition, they allow to model a realistic patient anatomy and to study individually the impact of the many parameters that are involved. However, to obtain reliable results, every numerical analysis needs to be validate be experimental evidence. In this paper we propose a Finite-Differences Time-Domain (FDTD) model able to simulate the interaction between the radiofrequency (RF) field of an MRI scanner and human tissues implanted with a PM. We also describe the method adopted for the validation of the model through experimental measurements.

As final output, a numerical tool that predicts the induced power as a function of the particular path of the PM lead is presented. We compared the two typical locations for a PM implant (left and right pectoral region) and we found a sensible difference - of about 30% - between the two cases. In general, the same analysis can be adopted to compare different possible solutions for the implant positioning and to evaluate the risks associated to a particular condition.

7.1 Introduction

Magnetic resonance imaging (MRI) is an important modality, with no ionizing radiation exposure, and it is used daily for clinical and interventional diagnosis. During MRI of patients implanted with metallic devices, such as pacemakers (PMs), brain stimulators, cochlear implants and so on, there is a risk of radiofrequency (RF) heating and special attention must be paid in such cases. In particular, the RF field generated during MRI procedure may induced electrical currents which flow from the metallic implant towards biological tissue and which might cause local tissue heating and damage. In-vivo and in-vitro experimental studies have shown the complexity of the electromagnetic fields induced within the associated radiofrequency (RF) coils and how many aspects influence the temperatures increase produced around the implant [1-6]. In particular, the implant configuration, which in the clinical practice can significantly vary from patient to patient (figure 1), seems to play a major role in MRI induced heating.

Such a complexity, together with the increasing recognition of the role played by tissue-coil interactions, made become clear that numerical techniques based on full-wave methods can provide essential information for understanding the behavior of RF coils when they are loaded with biological structures [7].

Computational tools based on full-wave methods can be very effective for feasibility studies of RF coils, which are extremely difficult to carry out in experimental settings. As such, for whole-body human

applications, computational electromagnetic can be effectively utilized to design and evaluate RF coils before they are constructed and tested experimentally. At fields B_0 below 1.5 Tesla, the design of radio frequency (RF) head coils for MRI systems traditionally has been based on circuit concepts. As B_0 fields are increased, however, these design concepts become inadequate since the RF coil dimensions are a significant fraction of the operational wavelength. Under these conditions, the currents in the coil do not behave in a manner in which circuit analysis can predict (Ibrahim 2000). Consequently, the use of computational EM techniques, such as the finite difference time domain (FDTD) method [8], has recently flourished for modeling RF coils [9-11], including birdcage [12] and transverse electromagnetic (TEM) [13] resonators. It is also anticipated that the optimization of current high-field RF coils or the design of new coils will rely heavily upon numerical modeling [14,15]. However, every numerical analysis needs to be validated by experimental evidence: for this reason, if a computational tool wants to be used to study the interaction between an EM field and a metallic structure implanted in biological tissues, preliminary experimental measures have to be performed in order to ensure the validity of the model.

Aim of this paper is to develop and to validate through experimental measures a numerical model able to reproduce the effects of the EM field generated by a birdcage RF coil on human tissues implanted with a metallic implant, in particular a PM. The model can be used to compare different implant configurations, in terms of deposited power at the lead tip, and to identify possible worst-condition case conditions.

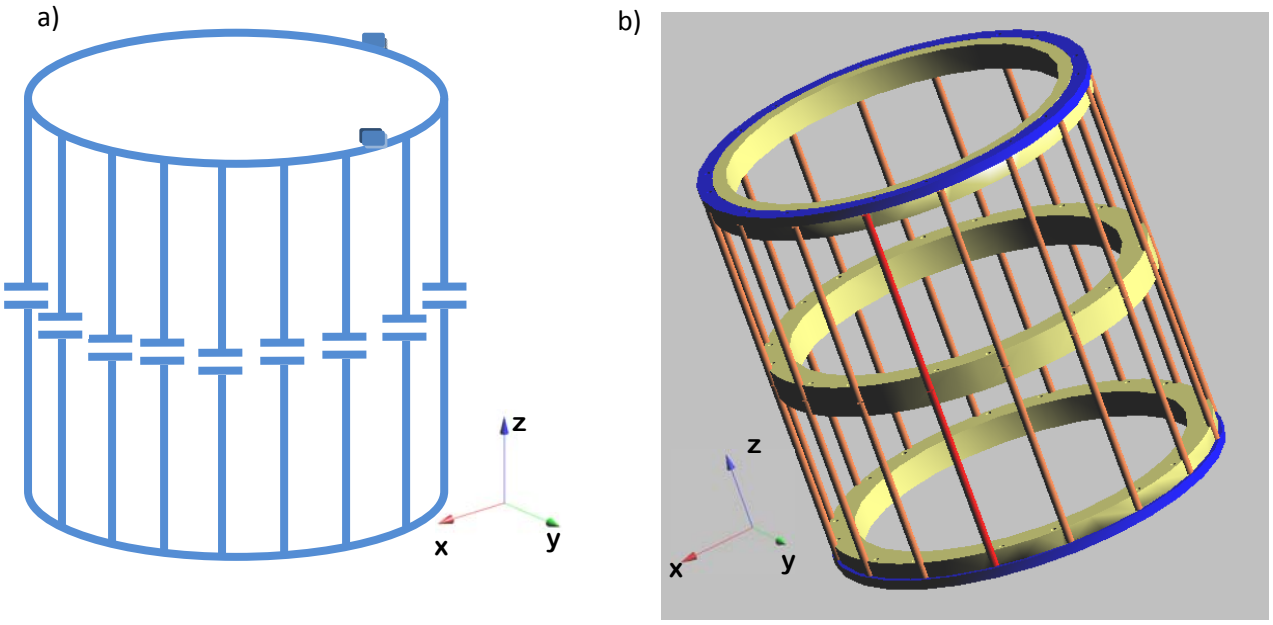

Figure 1. a) Typical structure of a16-legs low-pass birdcage coil; b) design of the birdcage coil in the 3D CAD environment.

7.2 Materials and Methods

In order to obtain numerical and experimental data that could be immediately compared, we developed a scheme of a 16-leg low-pass birdcage coil suitable as common base project for the numerical analysis and the realization of a physical model. The same structure implemented as numerical model and physical prototype allows to obtain a direct mean to validate the results of the numerical analysis, reducing all the possible variables that could be involved in other validation procedures.

As a preliminary study for the realization of the coil prototype, the standard structure of the low-pass birdcage typically proposed in literature (i.e. with a single capacitor used to match the resonance frequency placed in the middle of each leg – figure 1, a) has been compared with a more complex model, where, for each leg, besides the central capacitors, other two capacitors are added at the connection leg-ring. This structure was derived from a RF birdcage laboratory coil used during previous in-vitro experimental studies at the Center for Devices and Radiological Health (CDRH) of the Food and Drug Administration (FDA) [6] on the induced heating on metallic implants. The electromagnetic field distribution inside the two birdcage models where obtained using a commercial FDTD software (SEMCAD X, version 14.0, SPEAG, Zurich) that incorporated native drawing and importing of 3-D CAD object models in ACIS (.sat) format. The software had a variable grid (graded-mesh) generator and was used on a personal computer with a 2.4 GHz, 64-bit processor, 3 GB of RAM, and a Windows XP operating system. An accelerator card (aXware V1.5 Card) was used to speed up the solution time required by the numerical models.

The common scheme for the realization of the numerical and physical birdcage model was designed using a commercial 3D-CAD sofware (SolidWorks, *SolidWorks Corporation*, USA): the dimensions of the different components of the coil were chosen big enough to be easily implemented in the FDTD environment, but at the same time suitable to be handled in a common mechanical workshop. In particular, the coil is made up of 16 cylindrical legs (diameter = 6 mm, height = 30 cm) and two external rings with a rectangular section (12 mm x 8 mm) and an internal diameter of 30 cm. For each leg, three gaps of 1 mm where left for the placement of the tuning capacitors, in the middle and just before the connection with the rings. Three PVC rings were also used to get the structure more stability, in the point where the capacitors have to be placed (figure 1, b).

We first imported the CAD file with the geometry of the coil in the FDTD environment and we performed a preliminary broadband analysis in order to find the value of the tuning capacitors that allows the coil to be resonant at the frequency of 64 MHz (the RF used in the 1.5 T clinical scanner). The variable capacitors used in the physical model of the coil were then tuned using a LRC meter (4263B, *Hewlett-Packard*, USA) to the same value resulting from the broadband simulation. On one of the two rings were also realized two RF ports (figure 2, a), where it is possible to apply a voltage gap between the ring and one of the legs, (in parallel to one of the tuning capacitors).

A handheld vector network analyzer (Bravo MRI II, *AEA Technology Inc*, USA) was used in order to measure the electrical parameters of the coil prototype at the frequency of 64 MHz. A first step towards the validation of the numerical model was the comparison between the reflection coefficient measured for the physical model

and for the numerical one, as a function of the frequency. The birdcage prototype was then fed with a single 64 MHz sinusoidal source applied at one of the RF port, whereas the other was close on a 50 Ohms load. This kind of source is used when a linear-polarized magnetic field wants to be obtained inside the coil.

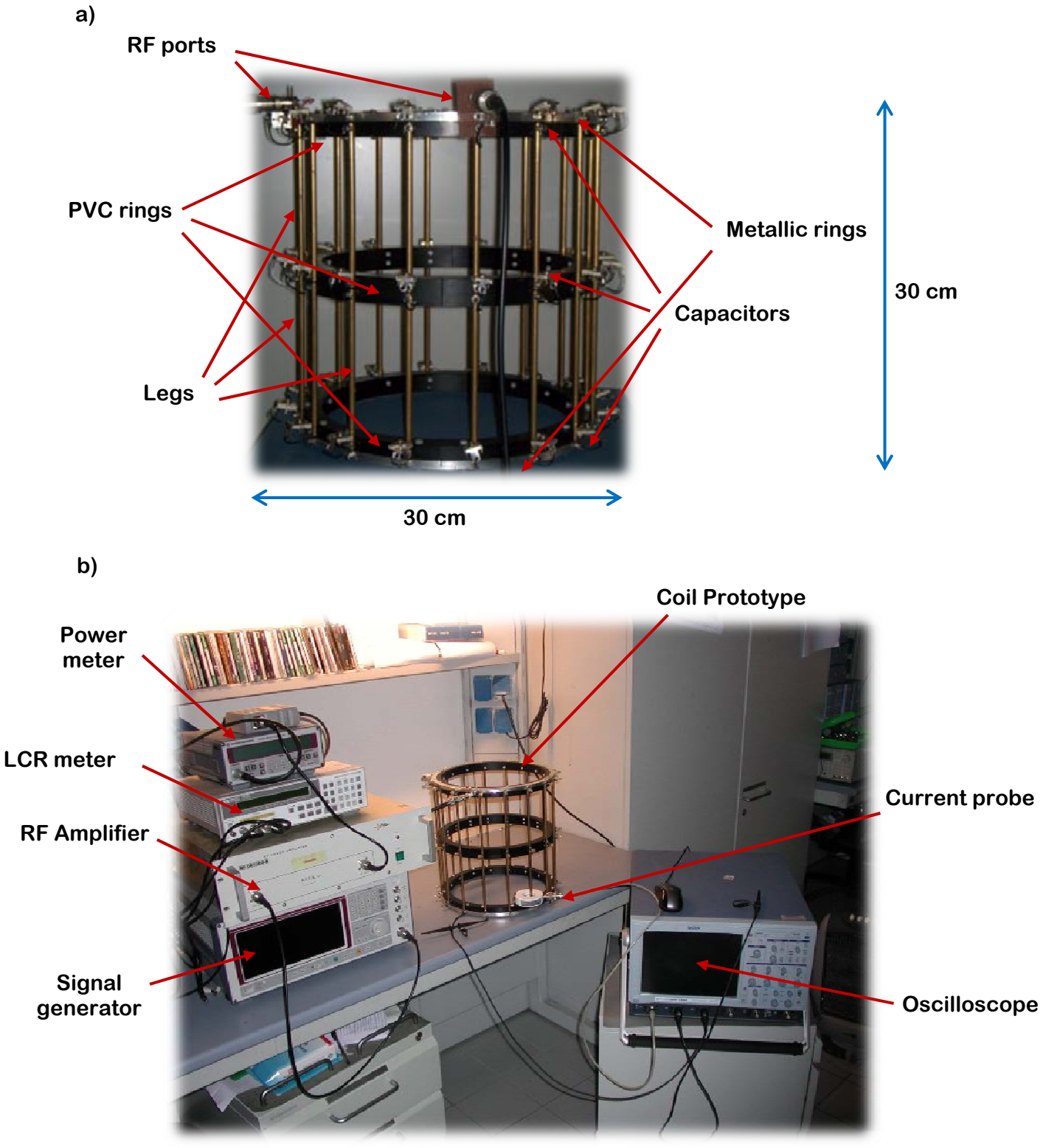

Figure 2. a) Physical model of the 16-leg low-pass birdcage coil; b) experimental set-up for the RF measurements on the birdcage coil.

The experimental set-up adopted is described in figure 2, b: a signal generator (SMT 06, *Rhode & Schwartz*, Germany) was connected to a RF amplifier (RF 06100-6, *RFPA*, France) and the output power towards the coil was monitored in real time thanks to a RF power meter (NRT, Z14, *Rhode & Schwartz*, Germany). The voltage signal applied at the RF port was monitored by a high-frequency oscilloscope (WavePro 7300A, *LeCroy*, USA), and also the current distribution along each leg was measured using a clamp-on broadband current probes (BCP-512, *A.H. System*, USA).

The same voltage source used to excite the physical model of the coil was reproduced in the numerical model, and the resulting currents computed along the legs were compared to experimental data.

The FDTD model was then scaled to match the dimensions of a total body birdcage scanner (length = 62 cm; diameter = 62 cm) and a rectangular box was added inside the coil, in order to simulate a standard gel saline phantom used for testing of MRI heating of implants [16]. We used a temperature measure database collected in a birdcage coil simulator and presented in a previously published paper [6] to compare the SAR values recorded experimentally with the computed data, over equivalent implant configurations and with an equivalent whole-body SAR.

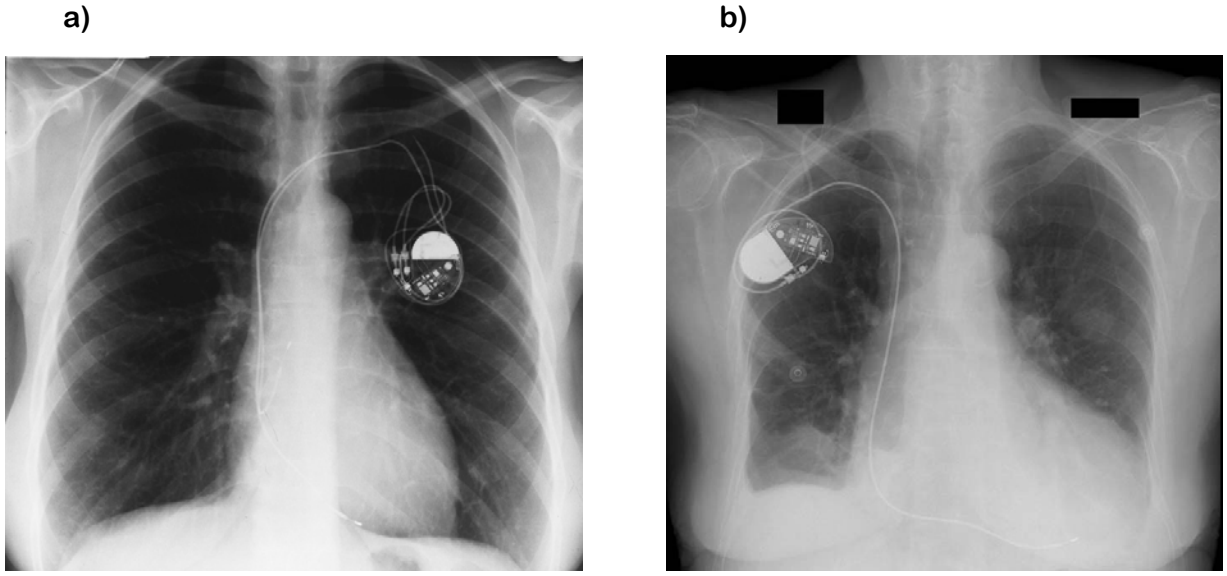

Figure 3. RX images of a patients implanted with a PM: a) left pectoral implant positioning; b) right pectoral implant positioning.

Once we ensure the validity of the model, we integrated it with a "visible human dataset", that reproduces 34 different human tissues, with a spatial resolution of 2 mm. The voltage excitation applied to the coil was chosen in order to determinate an averaged whole-body SAR inside the human trunk model of $1 Wkg^{-1}$. This value is consistent with the typical MRI clinical procedures and is the same used by the authors during the experimental measurements performed inside a laboratory RF coil [5,6].

Finally, two typical PM implants were reproduced inside the human trunk model: in the first case, the PM chassis was located in the left pectoral region, immediately under the skin and the lead was inserted into the left subclavian vein, the left brachoencefalic vein, the superior cava vein, the right atrium, till the right ventricle, where the tip is put in contact with the heart wall (Figure 4). The second implant reproduces a right-pectoral PM implant: the lead reaches the right atrium through the right subclavian vein, the right brachoencefalic vein, and the superior cava vein. The path from the right atrium to the right ventricle is common for the two configurations. The implant geometries and positioning were derived from RX images of implanted patients, reported in figure 3.

The FDTD model of the birdcage coil and of the human visible dataset provided with the PM implant required a very height spatial resolution: in particular, all over the area covered by the implant the graded mesh had to be very fine (min. step=0.4 mm), in order to simulated the insulated sheath all along the lead path.

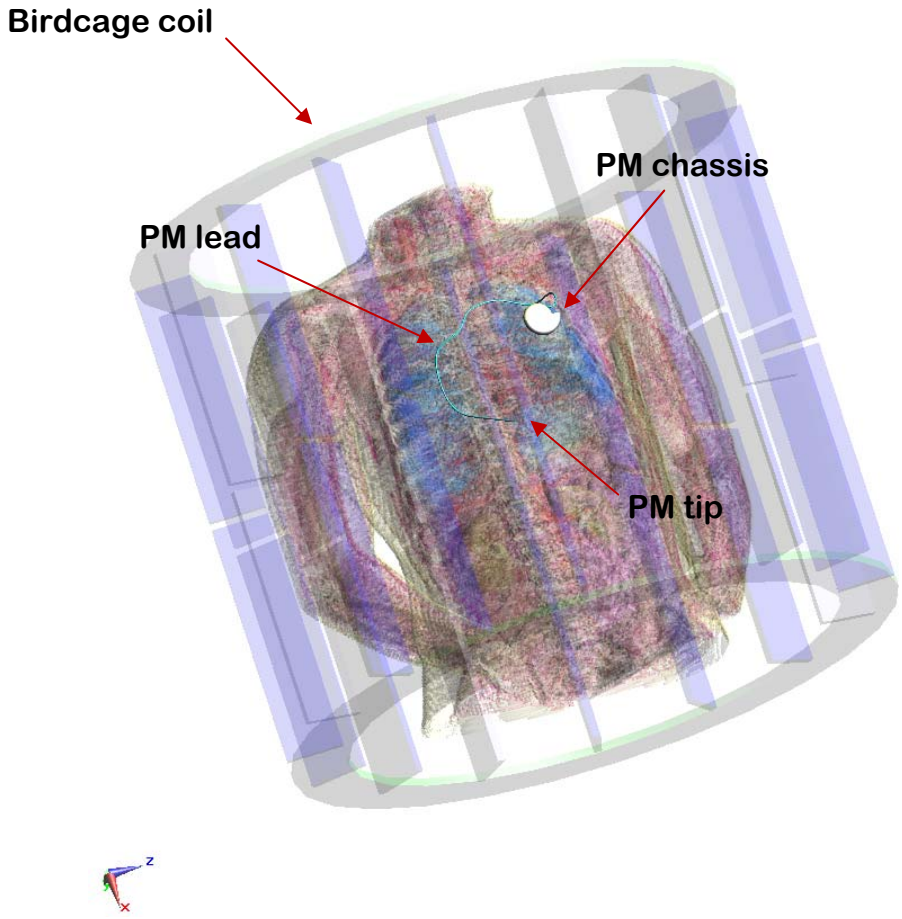

Figure 4. FDTD model of the whole-body birdcage coil and of the visible human dataset implanted with a PM.

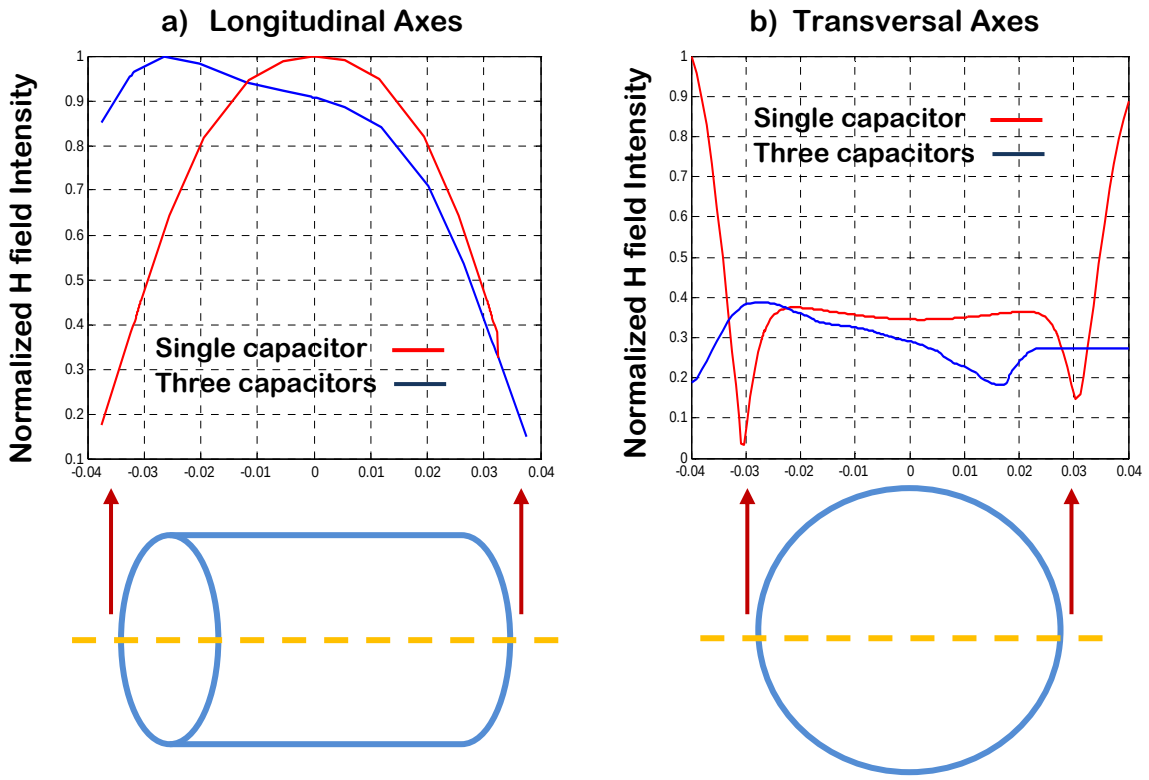

Figure 5. Effect of the three tuning capacitors on each leg of the birdcage coil model in the H field distribution: a) longitudinal axes; b) transversal axes.

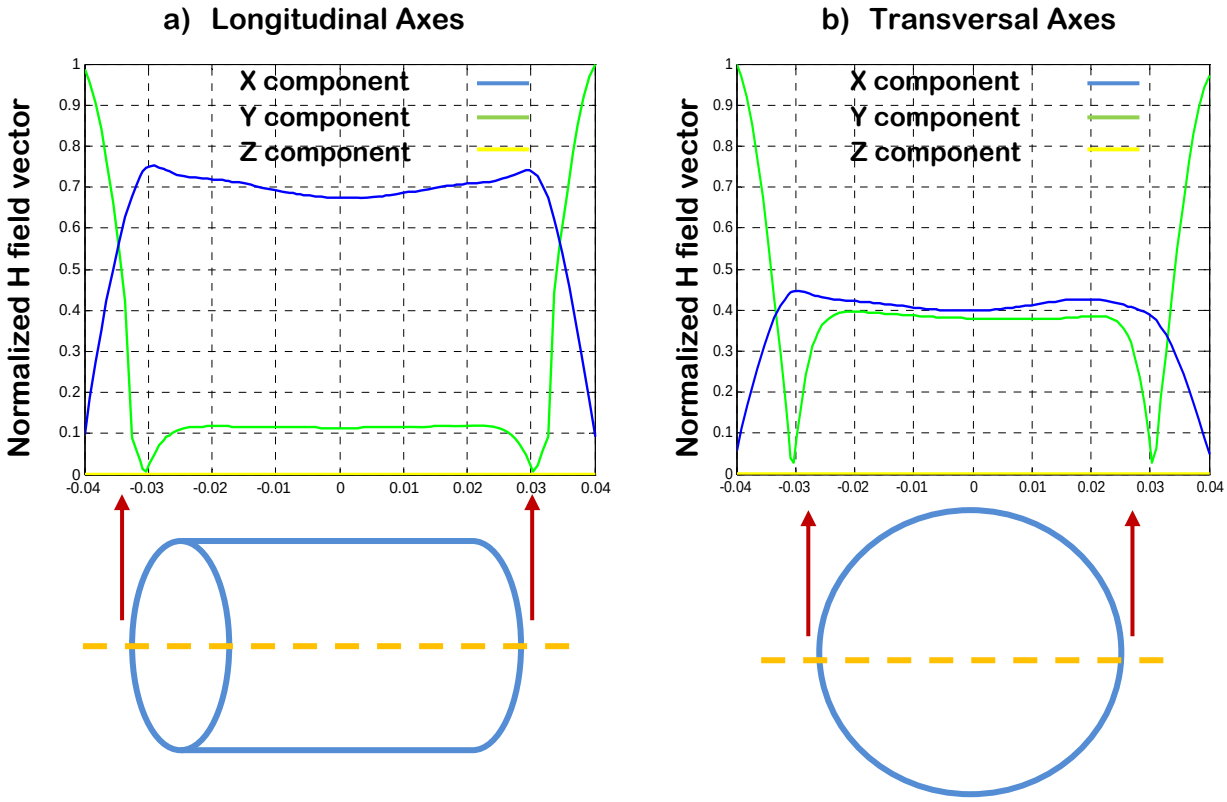

Figure 6. H field components along the three spatial axis inside the birdcage coil model: a) single source excitation; b) quadrature excitation.

7.3 Results

The standard birdcage model, with a single capacitor on each leg, was compared with a more complex structure, with three capacitor for each leg. The new tuning elements introduced in the model make the magnetic field distribution inside the coil more uniform and symmetric, as shown in figure 5.

We also compared the magnetic field as a function of the excitation applied to the coil: a single sinusoidal voltage source results in a linearly polarized magnetic field; whereas a couple of sinusoidal signals with a 90° shift both in space and in time (quadrature excitation) , produces a circularly polarized magnetic field inside the coil. The components of the H field along the three spatial axes are plotted in figure 6, for the single and quadrature source excitations.

These preliminary results were the starting point for the design of a 3D common scheme to be used both for the FDTD analysis and for the realization of a physical birdcage coil prototype; by the comparison between the numerical results and the RF experimental measurements on the coil, we could validate the proposed model. In figure 6 the reflection coefficients vs. frequency computed for the numerical and physical model are reported.

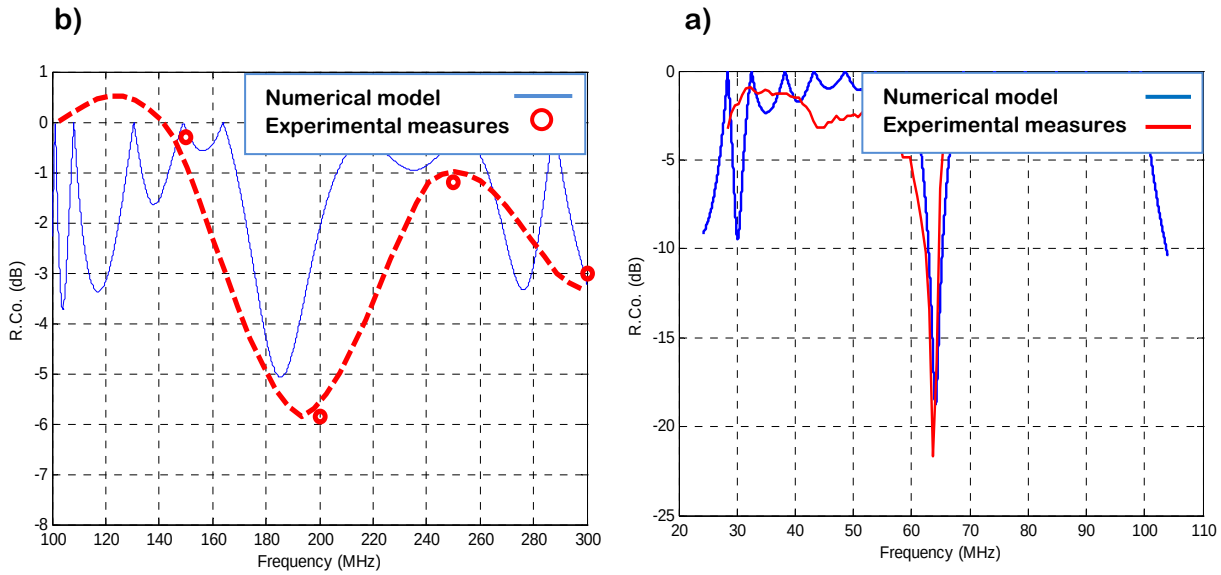

Figure 7. Reflection coefficient computed in the numerical model and by experimental measurements on the birdcage coil prototype: a) coil structure without capacitors; b) coil structure with the capacitors tuned at 17 pF.

The simple birdcage structure, without any tuning capacitor, shows an intrinsic resonance at about 200 MHz (Figure 7, a). By adding three capacitors for each leg of the coil, the resonance frequency becomes lower; with all the capacitors tuned at the value of 17 pF, it is possible to match the radiofrequency typically used in the 1.5T MRI scanners (i.e. 64 MHz, figure 7, b).

In a second set of measurements, we compared the current distribution along the legs of the coil (Figure 8): both in the numerical model and in the physical prototype, the coil was excited with a single voltage signal (peak amplitude=7.7 V) applied between one a ring and one of the leg.

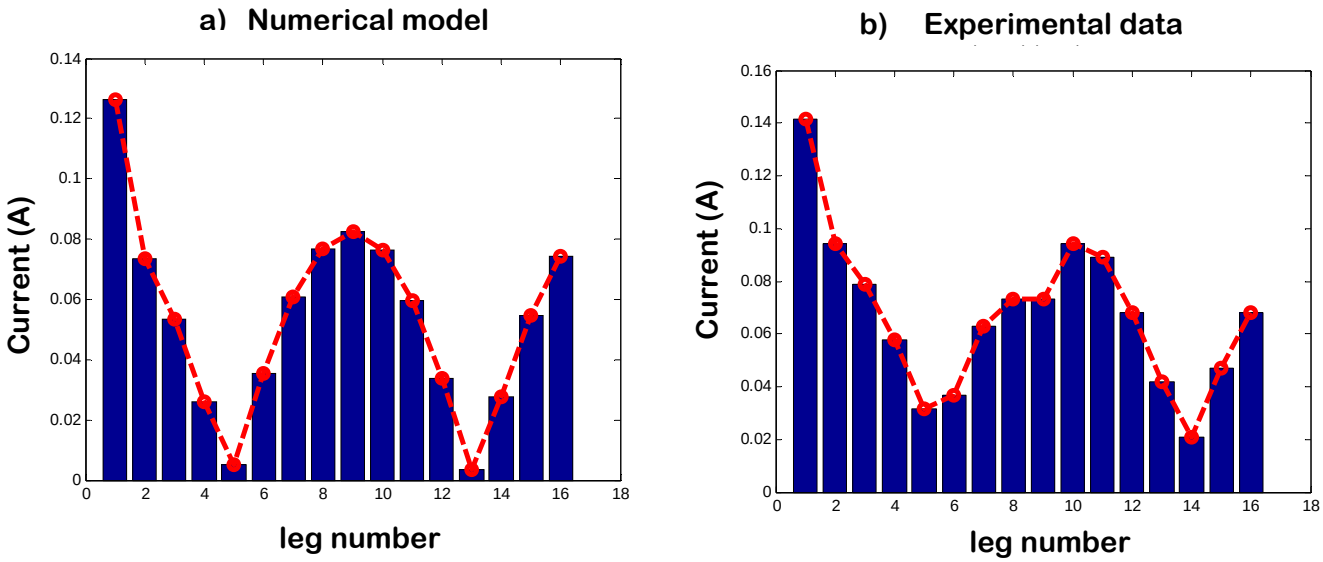

Figure 8. Current distribution along the legs of the birdcage coil: a) numerical model; b) experimental data. In both cases, the voltage source was applied between the ring and leg 1.

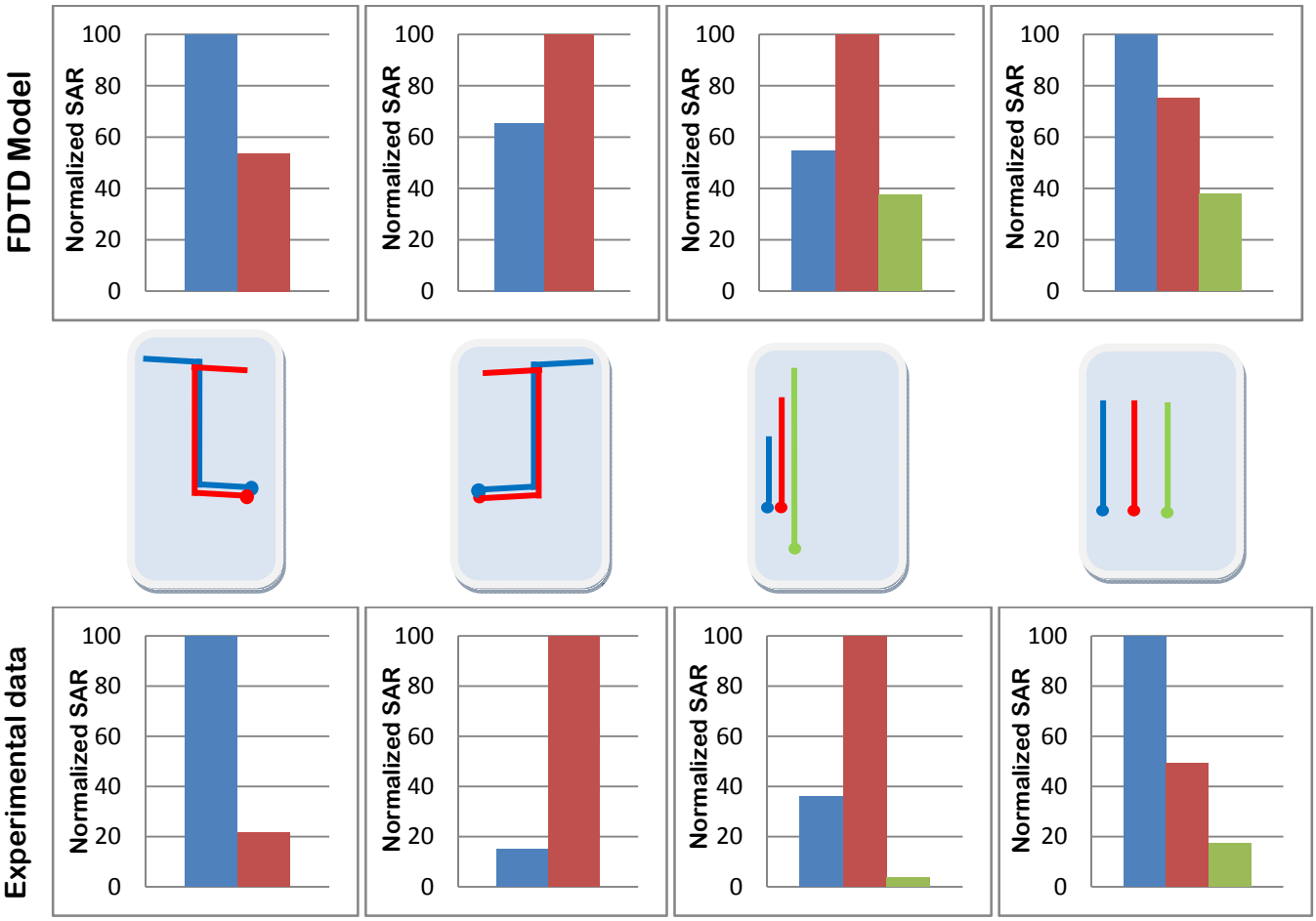

Figure 9. Comparison between the SAR measured from the temperature increases recorded inside a laboratory RF coil and SAR computed in the FDTD over equivalent configuration implant and RF exposure. Note that each graph has been normalized to the corresponding maximum value of SAR.

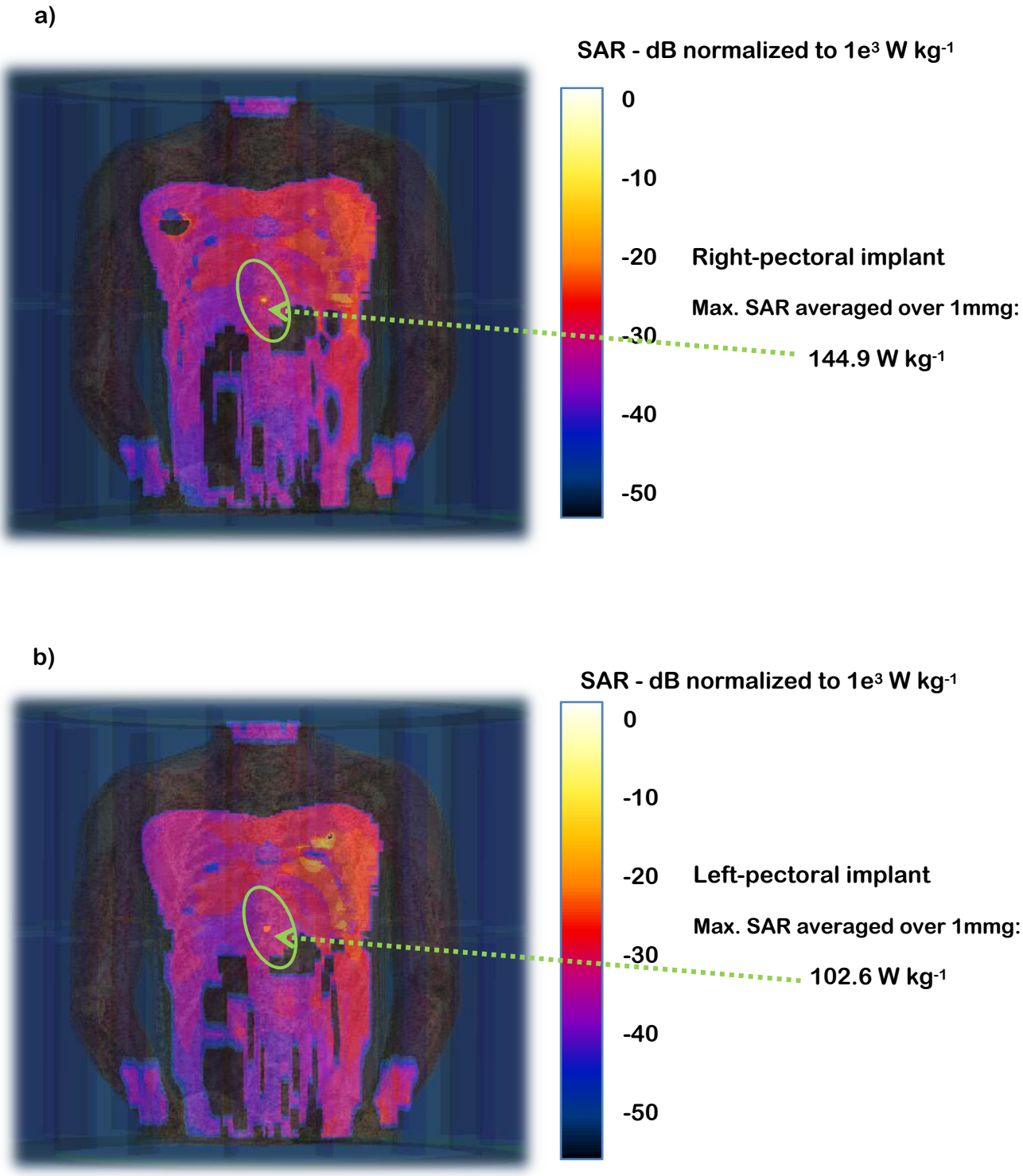

Figure 10. Human visible dataset implanted with a PM and exposed to the RF field of a birdcage coil: SAR distribution resulted from the numerical model; a) right pectoral implant configuration; b) left-pectoral implant configuration.

Besides RF measurements, we also validate the FDTD model of the birdcage coil in terms of deposited power inside a dielectric domain implanted with thin metallic. To this aim, we use an experimental database of

temperature and SAR measurements preformed inside a whole body birdcage laboratory coil [6] and we reproduced the same experimental set-up in the FDTD environment.
In particular, we modeled a rectangular box (with dimensions and physical properties equal to the ones of the rectangular-shaped phantom used in the experimental measures) implanted thin metallic wires of different shapes, length and location (figure 9). Experimental and computed data are consistent: wires with the same shape but differently orientated produces different heating (figure 9, a and b); the highest temperature increase is obtained when the wire has a length close to the theoretical resonance value at 64 MHz (≈ 26 cm, figure 9, c); the more the wire is next to the edge of the phantom, the highest is the induced heating at its tip (figure 9, d).
The validated birdcage coil model was then completed with the human visible dataset and a PM implant: in particular, a right and a left pectoral implant configuration were reproduced. In figure 10 the SAR distribution over a frontal plane through the lead tip is reported for the two cases. The SAR values were computed as the average over 1 mg tissue mass. A 1 mg mass was chosen as good trade-off between a volume small enough to cover significantly high SAR value and, at the same time, big enough to avoid the case of a local "hot spot".

7.4 Discussion

Each year, approximately 1 million people worldwide are implanted with a PM, hundreds of thousands of whom may be able to benefit from an MRI scan. A recent study [17] shows that an MRI procedure is requested by a physician for 17% of PM patients within 12 months of device implant. Every three minutes in the U.S. and every six minutes in Europe, a patient is denied an MRI scan due to the presence of an implantable cardiac device.
Several studies have demonstrated the potential for MRI to be performed in PM or ICD patients without serious clinical consequence [2,18,19]. As with the previous studies, however, the authors acknowledge a multitude of limitations that prevent broad applicability of the results and thus make necessary further and more comprehensive investigations.
With regards to the MRI induced heating on PM and ICD leads, the large number of variables that take part in the process makes extremely difficult to perform extensive and exhaustive experimental measurements; modellistic approaches based on numerical tools might represent a useful mean, able to limit the number of experimental measures and to better identify the contributes of the various aspects involved. However, every numerical study needs an appropriate experimental validation in order to give reliable results. In this study a numerical model based on FDTD simulations was validated to obtain a general tool for investigating the large number of parameters and factors involved in this complex phenomenon. In particular, the numerical model of an MRI birdcage coil was validated by comparing it with an equivalent custom-designed physical structure. The birdcage coil we reproduced has three capacitor for each leg, differently from the standard birdcage model that uses a single capacitor for each leg: this is a common solution adopted by the RF coil manufactories in

order to obtain a more uniform and symmetric field distribution and do not add too much computational effort to the FDTD simulation.

RF measurements of the reflection coefficient and of the current distribution along the leg of the coil show that the FDTD model well reproduces the behavior of the physical structure, if assuming the same excitation signal and the same value for the tuning capacitors. The maximum error between the numerical model and the experimental data was as low as 3 dB for the reflection coefficient at 64MHz, and 0.038 A in the worst case for the current distribution (mean error = 0.013 A).

We also compared the deposited power computed in the numerical model at the tip of metallic wires with a set of experimental data collected in a laboratory birdcage coil: the comparison could not be done in terms of absolute SAR. Experimental values were calculated from the slope of the initial temperature rise and thus contain an error related to the physical dimension of the temperature probe and to the methods for the SAR evaluation itself [4,6]. In addition, it is also difficult to define in the numerical model an optimal averaging mass for the SAR evaluation, suitable to be compared with the experimental data. However, the factors that in the experimental study played a major role in the induced heating (implant location, geometry and length), have been confirmed to be important element also in the numerical simulation, giving the same results, over equivalent configurations.

The correspondence between the numerical model and the physical coil is not invalidated if changing the absolute dimensions of the structure. The scaled model of the whole-body birdcage coil inside which the visible human dataset was implemented, was tuned to have the same resonance behavior at 64 MHz. The RF measurements that allowed to validate the model of the coil prototype are therefore still valid for the whole–body model.

The SAR distribution computed inside the human visible implanted with the PM and its lead shows that the implant positioning inside the body is an important aspect that can affect the amount of heating induced at the lead tip. Today, the site for the PM location (left or right pectoral region) is generally chosen according to the surgeon preferences, without any relevant clinical motivation. Our data show that the PM implanted in the right pectoral region causes a SAR deposition at the lead tip that is about 30% higher that the left-pectoral implant. It suggests that the left pectoral region has somehow to be preferred as the location site for a PM implant. The asymmetric distribution of the electric field within the body (20) and the better coupling of the right-implant lead with the currents induced in the biological tissues (6) can justify such a behavior. Experimental data conducted on homogeneous phantoms implanted with PM in different configurations (3,5,6,20) confirm these data. The numerical approach adopted in this study allows to take into account several aspects that experiments on homogenous gelled phantoms cannot consider: in particular, the possibility to design a path for the PM lead that follows the anatomical structures of blood vessels and to model different tissues with different electromagnetic properties, makes the analysis more realistic and helps in extending the range of experimental measurements, and in correlating heating results to those expected in humans.

A limitation of our study is that we did not modeled the heat transfer mechanisms adopted by living tissues in order to maintain the temperature inside a given range. Such a limitation also affects the experimental in-vitro

measurements with gelled phantom and does not allow to immediately relate the computed SAR to a consequent temperature increase and tissue damage. However, the model we developed still represent a useful tool by which to evaluate the potential safety issues related to the MRI induced heating MRI on implanted patients. In particular, it allows to balance advantages and disadvantages associated to a particular implant configuration, as a function of the implant location, implant geometry and of the total-body deposited power, and eventually to plan an MRI scan also in presence of a PM, without posing a real risk to the patient.

7.5 Conclusions

This paper proposes a numerical model for the evaluation of the SAR induced in human tissues implanted with a PM and its lead, when exposed to the RF field generated by an MRI birdcage coil. In order to validate the model two sets of experimental data have been used: 1) RF measurements on a custom-designed birdcage coil prototype; 2) temperature and SAR measurements on metallic wires implanted inside gelled phantoms and exposed to the RF field of a laboratory whole-body birdcage coil. Once validate the model, it has been completed with a visible human dataset implanted with a PM. The SAR distribution computed for the two typical implant configurations (left and right pectoral region) reveal that the implant location is an important aspect that affects the amount of the induced heating at the lead tip. In particular, a left pectoral implant seems to be related to a lower temperate increase than the right one.

The numerical model we developed represents a useful tool that allows to study the peculiarity of specific implant configurations and to predict the induced SAR in the surrounding tissues. It could be adopted by the medical staff in order to decide whether to perform the MRI scan or not, and, in case, to plan the treatment, so to minimize to potential risks for the patient.

References

[1] Sommer T, Vahlhaus C, Lauck G, von Smekal A, Reinke M, Hofer U, Block W, Traber F, Schneider C, Gieseke J, Jung W, Schild H: MR imaging and cardiac pacemakers: in-vitro evaluation and in-vivo studies in 51 patients at 0.5 T. *Radiology* 2000, **215**(3):869-79

[2] Roguin A, Zviman MM, Meininger GR, Rodrigues ER, Dickfeld TM, Bluemke DA, Lardo A, Berger RD, Calkins H, Halperin HR: Modern pacemaker and implantable cardioverter/defibrillator systems can be magnetic resonance imaging safe: in vitro and in vivo assessment of safety and function at 1.5 T. *Circulation* 2004, **110**(5):475-82. 2004 Aug 3

[3] Bassen H, Kainz W, Mendoza G, Kellom T: MRI-induced heating of selected thin wire metallic implants – laboratory and computational studies – findings and new questions raised. *Minim Invasive Ther Allied Technol* 2006, **15**(2):76-84

[4] Mattei E, Triventi M, Calcagnini G, Censi F, Kainz W, Bassen HI, Bartolini P: Temperature and SAR measurement errors in the evaluation of metallic linear structures heating during MRI using fluoroptic probes. *Phys Med Biol* **52**(6):1633-46. 2007 Mar 21

[5] Calcagnini G, Triventi M, Censi F, Mattei E, Bartolini P, Kainz W, Bassen HI. In vitro investigation of pacemaker lead heating induced by magnetic resonance imaging: role of implant geometry. *J Magn Reson Imaging*. 2008 Oct;**28**(4):879-86

[6] Mattei E, Triventi M, Calcagnini G, Censi F, Kainz W, Mendoza G, Bassen HI, Bartolini P. Complexity of MRI induced heating on metallic leads: experimental measurements of 374 configurations *Biomed Eng Online*. 2008 Mar 3;**7**:11

[7] Ibrahim TS, Mitchell C, Schmalbrock P, Lee R, Chakeres DW.Electromagnetic perspective on the operation of RF coils at 1.5-11.7 Tesla. *Magn Reson Med*. 2005 Sep;**54**(3):683-90

[8] Yee KS. Numerical solution of initial boundary value problems involving Maxwell's equations in isotropic media. *IEEE Trans Antenna Propag* 1966;**4**:302–307

[9] Jin JM, Chen J, Chew WC, Gan H, Magin RL, Dimbylow PJ. Computation of electromagnetic fields for high-frequency magnetic resonance imaging applications. *Phys Med Biol* 1996;41:2719–2738.

[10] Collins CM, Li SL, Smith MB. SAR and B1 field distributions in a heterogeneous human head model within a birdcage coil. *Magn Reson Med* 1998;**40**:846–856

[11] Ibrahim TS, Lee R, Baertlein BA, Yu Y, Robitaille P-ML. Computational analysis of the high pass birdcage resonator: finite difference time domain simulations for high-field MRI. *Magn Reson Imaging* 2000; **18**:835–843

[12] Hayes EC, Edelstein WA, Schenck DF, Mueller OM, Eash M. An efficient highly homogeneous radiofrequency coil for whole-body NMR imaging at 1.5 T. *J Magn Reson* 1985;**63**:622–628

[13] Vaughan JT, Hetherington HP, Otu JO, Pan JW, Pohost JM. High frequency volume coils for clinical NMR imaging and spectroscopy. *Magn Reson Med* 1994;**32**:206–218

[14] Ibrahim TS, Lee R, Abduljalil BABAM, Zhu H, Robitaille P-ML. Effect of RF coil excitation on field inhomogeneity at ultra high fields: a field optimized TEM resonator. *Magn Reson Imaging* 2001;**19**:1339–1347

[15] Ibrahim TS, Lee R, Baertlein BA, Robitaille P-ML. Application of finite difference time domain method for the design of birdcage RF head coils using multi-port excitations. *Magn Reson Imaging* 2000;**18**:733–742

[16] ASTM F2182–02a – ''Standard Test Method for Measurement of Radio Frequency Induced Heating Near Passive Implants During Magnetic Resonance Imaging'', *ASTM International*, 100 Barr Harbor Drive, PO Box C700, West Conshohocken, PA, 19428–2959 USA

[17] Sommer T, Naehle CP, Yang A, Zeijlemaker V, Hackenbroch M, Schmiedel A, Meyer C, Strach K, Skowasch D, Vahlhaus C, Litt H, Schild H. Strategy for safe performance of extrathoracic magnetic resonance imaging at 1.5 tesla in the presence of cardiac pacemakers in non-pacemaker-dependent patients: a prospective study with 115 examinations. *Circulation*. 2006 Sep 19;**114**(12):1285-92

[18] Martin ET, Coman JA, Shellock FG, Pulling CC, Fair R, Jenkins K Magnetic resonance imaging and cardiac pacemaker safety at 1.5-Tesla. *J Am Coll Cardiol*. 2004;**43**:1315–1324

[19] Gimbel JR, Kanal E, Schwartz KM, Wilkoff BL. Outcome of magnetic resonance imaging (MRI) in selected patients with implantable cardioverter defibrillators (ICDs). *Pacing Clin Electrophysiol*. 2005;**28**:268–269

[20] Nordbeck P, Fidler F, Weiss I, Warmuth M, Friedrich MT, Ehses P, Geistert W, Ritter O, Jakob PM, Ladd ME, Quick HH, Bauer WR. Spatial distribution of RF-induced E-fields and implant heating in MRI. *Magn Reson Med*. 2008 Aug;60(2):312-9

Conclusions

Our study, together with the other papers published in literature dealing with the MRI induced heating on pacemaker and ICD leads, highlights how complex the phenomenon is and how many aspects must be well addressed in order to perform an exhaustive and reliable analysis.

Most of the data related to the compatibility between MRI and pacemaker come out from in-vitro and in-vivo experimental studies [1-11]. Even if the results, in terms of amount of heating generated at the lead tip, significantly vary among the different studies reported in literature, it is quite easy to asses that the RF induced temperature increases during an MRI scan is a matter-of-fact problem. It undoubtedly plays a major role in the definition of the possible safety conditions for the extension of MRI examinations also to patients implanted with metallic structures.

While experimental data are now becoming more and more available [10,11], only few studies have been conducted adopting numerical and modellistic approaches [6,12,13]. This is mainly due to the fact that simplified, low resolution simulations are not useful for small metallic structures and thin wires exposed to the RF field of MRI coils. On the other hand, numerical studies could allow to better address the large number of variables which may be involved in the amount of heat generation and which make difficult to perform extensive and exhaustive experimental measures.

In this study we systematically investigate the MRI induced heating on metallic wires and pacemaker implants, both performing experimental measurements and numerical analysis. Our findings point out the major aspects that are involved in the process:

- The position of the implant inside the body;
- The position of the body respect to the RF coil;
- The path and the exposed length of the lead;
- The RF sequence used during the MRI scan;
- The morphology of the patient.

In order to minimize the temperature increase induced at the lead tip, implant configurations with a short exposed lead segment should be chosen; in addition, the portions of the implant located immediately under the skin should be reduced as much as possible. MRI scans with a ”field of view” that does not involve the implanted tissues are related to a lower induced heating compared to scans of the body areas were the metallic structures are located. Finally, RF sequences with a high whole-body averaged SAR are the ones associated with the highest temperature increases; on the other hand, other imaging procedures with a low SAR value might produce no significant heating.

However, the complexity and the large number of variables involved in the process, make extremely difficult to define standard safety conditions for MRI scans of patients implanted with metallic structures. Each specific situation should be evaluated as a function of the particular type of imaging procedure, the implant location and its geometry, the anatomical characteristics of the patient, and so on.

A preliminary study using numerical models could represent an useful evaluation tool in planning the treatment. The FDTD model we developed is able to calculate the SAR distribution inside a realistic model of the human tissues exposed to the RF filed generated by a whole-body birdcage coil typically used in MRI scans. The *human visible dataset* can be integrated with the model of a pacemaker or of another metallic implant; it thus allows to predict the potentially induced heating as a function of its geometry, its location and of the type of MRI scan that is going to be planned.

The numerical model was validated by comparing it with RF experimental measures on a custom-made birdcage coil prototype. The coil was designed and realized inside the cardiovascular unit of the department of Technology and Health of the Italian National Institute of Health. It reproduces the actual structure of a birdcage coil used to generate the RF field of a MRI system and allows to easily characterize the RF behavior of the structure. Furthermore, we also chose a set of temperature and SAR measurements on metallic leads to verify the consistency between what we got from experimental measures and from numerical analysis.

In conclusion, the methods developed and validated during the PhD program led to the design of an experimental framework for the accurate measure of PM lead heating induced by MRI systems. In addition, numerical models based on FDTD simulations were validated to obtain a general tool for investigating the large number of parameters and factors involved in this complex phenomenon. The results obtained demonstrated that the MRI induced heating on metallic implants is a real risk that represents a contraindication in extending MRI scan also to patient bearing a pacemaker, and ICD, or other thin metallic objects. On the other side, both experimental data and numerical results show that, under particular conditions, MRI procedures might be consider reasonably safe also for an implanted patient. The complexity and the large number of variables involved, make difficult to define a unique set of such conditions: when the benefits of a MRI investigation cannot be obtained using other imaging techniques, the possibility to perform the scan should not be immediately excluded, but some considerations are always needed. The final decision has to be taken by the medical staff, that must evaluate the implant geometry and its position respect to the area that has to be scanned; furthermore, the radiologist must plan the treatment, using the RF sequences associated to the lowest whole body SAR.

References

[1] Sommer T, Vahlhaus C, Lauck G, von Smekal A, Reinke M, Hofer U, Block W, Traber F, Schneider C, Gieseke J, Jung W, Schild H: MR imaging and cardiac pacemakers: in-vitro evaluation and in-vivo studies in 51 patients at 0.5 T. *Radiology* 2000, **215**(3):869-79

[2] Achenbach S, Moshage W, Diem B, Bieberle T, Schibgilla V, Bachmann K: Effects of magnetic resonance imaging on cardiac pacemakers and electrodes. *Am Heart J* 1997, **134**(3):467-73

[3] Roguin A, Zviman MM, Meininger GR, Rodrigues ER, Dickfeld TM, Bluemke DA, Lardo A, Berger RD, Calkins H, Halperin HR: Modern pacemaker and implantable cardioverter/defibrillator systems can be magnetic resonance imaging safe: in vitro and in vivo assessment of safety and function at 1.5 T. *Circulation* 2004, **110**(5):475-82. 2004 Aug 3

[4] Martin ET, Coman JA, Shellock FG, Pulling CC, Fair R, Jenkins K: Magnetic resonance imaging and cardiac pacemaker safety at 1.5-Tesla. *J Am Col Cardiol* **43**(7):1315-24. 2004 Apr 7

[5] Konings MK, Bartels LW, Smits HF, Bakker CJ: Heating around intravascular guidewires by resonating RF waves. *J Magn Reson Imaging* 2000, **12**(1):79-85

[6] Bassen H, Kainz W, Mendoza G, Kellom T: MRI-induced heating of selected thin wire metallic implants – laboratory and computational studies – findings and new questions raised. *Minim Invasive Ther Allied Technol* 2006, **15**(2):76-84

[7] Rezai AR, Baker KB, Tkach JA, Phillips M, Hrdlicka G, Sharan AD, Nyenhuis J, Ruggieri P, Shellock FG, Henderson J: Is magnetic resonance imaging safe for patients with neurostimulation systems used for deep brain stimulation? *Neurosurgery* 2005, **57**(5):1056-62

[8] Kanal E: White Paper on MRI Safety. In American Society of Neuroradiology Toronto, Canada. May 24, 2005

[9] Gimbel JR: Magnetic resonance imaging of implantable cardiac rhythm devices at 3.0 tesla. *Pacing Clin Electrophysiol*. 2008 Jul; **31**(7):795-801

[10] Roguin A, Schwitter J, Vahlhaus C, Lombardi M, Brugada J, Vardas P, Auricchio A, Priori S, Sommer T, Magnetic resonance imaging in individuals with cardiovascular implantable electronic devices. Europace. 2008 Mar;10(3):336-46

[11] Nordbeck P, Weiss I, Ehses P, Ritter O, Warmuth M, Fidler F, Herold V, Jakob PM, Ladd ME, Quick HH, Bauer WR.Measuring RF-induced currents inside implants: Impact of device configuration on MRI safety of cardiac pacemaker leads. Magn Reson Med. 2009 Jan 8.

[12] Ho H. Safety of Metallic Implants in Magnetic Resonance Imaging. *Journal of Magnetic Resonance Imaging*. 2001;**14**: 472–7

[13] Stuchly MA, Abrishamkar H, Strydom ML. Numerical evaluation of radio frequency power deposition in human models during MRI. *Conf Proc IEEE Eng Med Biol Soc*. 2006;**1**:272-5